Universidade de Aveiro Departamento de Física
Ano 2011

Susana Margarida das Neves Mendes

FLUXOS CONVECTIVOS DE MOMENTO LINEAR SIMULADOS POR UM MODELO DE NUVENS 3D

CUMULUS MOMENTUM FLUXES IN CLOUD-RESOLVING MODEL SIMULATIONS OF TOGA-COARE

Universidade de Aveiro Departamento de Física
Ano 2011

Susana Margarida Das Neves Mendes

FLUXOS CONVECTIVOS DE MOMENTO LINEAR SIMULADOS POR UM MODELO DE NUVENS 3D

CUMULUS MOMENTUM FLUXES IN CLOUD-RESOLVING MODEL SIMULATIONS OF TOGA-COARE

Dissertação apresentada à Universidade de Aveiro para cumprimento dos requisitos necessários à obtenção do grau de Doutor em Física, realizada sob a orientação científica do Doutor Christopher S. Bretherton, Professor Catedrático do Departamento de Ciências Atmosféricas da Universidade de Washington e do Doutor Alfredo Moreira Caseiro Rocha, Professor Associado com Agregação do Departamento de Física da Universidade de Aveiro

Apoio financeiro da FCT através de Bolsa de Doutoramento Refª SFRH/BD22932/2005 no âmbito do III Quadro Comunitário de Apoio (2000-2006).

o júri

presidente

Professor Doutor José Carlos Esteves Duarte Pedro
Professor Catedrático da Universidade de Aveiro

Professor Doutor João Alexandre Medina Corte-Real
Professor Catedrático da Universidade de Évora

Professor Doutor Christopher S. Bretherton
Professor Catedrático da Universidade de Washington

Prof. Doutor Alfredo Moreira Caseiro Rocha
Professor Associado com Agregação da Universidade de Aveiro

Doutora Mariana Stichini Vilela Hart de Campos Bernardino
Investigadora do Instituto de Meteorologia

Doutor Paulo de Melo Gonçalves
Investigador do CESAM - Centro de Estudos do Ambiente e do Mar da Universidade de Aveiro

agradecimentos

Expresso aqui os meus mais profundos agradecimentos aos meus pais, que têm sido incansáveis e fonte de apoio inesgotável ao longo dos meus percursos pessoal e profissional. Obrigada por acreditarem e confiarem.

Ao Professor Doutor Christopher S. Bretherton pela orientação e coordenação deste trabalho, pelo conhecimento transmitido e pela educação científica.

Ao Prof. Doutor Alfredo Rocha pelo apoio fundamental, sob os mais diversos aspectos, ao longo de todo este processo.

Ao Professor Doutor João Corte-Real pela amizade, pela confiança, pela colaboração ao longo de mais de uma década e pelo contínuo estímulo dado em relação ao meu próprio percurso científico. Bem haja, Professor!

Aos Doutores Peter Blossey e Matthew Wyant, do Departamento de Ciências Atmosféricas da Universidade de Washington, pelas preciosas informações acerca dos dados, do modelo utilizado neste trabalho e pelas inúmeras dicas em relação ao software utilizado.

A todos os meus amigos, em Portugal e em Seattle, que me acompanharam sempre com muito carinho e inesgotável paciência, nesta longa jornada.

palavras-chave

Transporte vertical de momento linear horizontal, convecção profunda, modelo de nuvens 3D, campanha TOGA-COARE.

resumo

O objectivo deste trabalho científico é o estudo do transporte vertical de momento linear horizontal (*CMT*) realizado por sistemas de nuvens de convecção profunda sobre o oceano tropical. Para realizar este estudo, foram utilizadas simulações tridimensionais produzidas por um modelo explícito de nuvens (CRM) para os quatro meses de duração da campanha observacional TOGA COARE que ocorreu sobre as águas quentes do Pacífico ocidental. O estudo foca essencialmente as características estatísticas e à escala da nuvem do CMT durante um episódio de fortes ventos de oeste e durante um período de tempo maior que incluí este evento de convecção profunda. As distribuições verticais e altitude-temporais de campos atmosféricos relacionados com o CMT são avaliadas relativamente aos campos observacionais disponíveis, mostrando um bom acordo com os resultados de estudos anteriores, confirmando assim a boa qualidade das primeiras e fornecendo a confiança necessária para continuar a investigação. A sensibilidade do CMT em relação do domínio espacial do model é analisada, utilizando dois tipos de simulações tridimensionais produzidas por domínios horizontais de diferente dimensão, sugerindo que o CMT não depende da dimensão do domínio espacial horizontal escolhido para simular esta variável. A capacidade da parameterização do comprimento de mistura simular o CMT é testada, destacando as regiões troposféricas onde os fluxos de momento linear horizontal são no sentido do gradiente ou contra o gradiente. Os fluxos no sentido do gradiente apresentam-se relacionados a uma fraca correlação entre os campos atmosféricos que caracterizam esta parameterização, sugerindo que as formulações dos fluxos de massa dentro da nuvem e o fenómeno de arrastamento do ar para dentro da nuvem devem ser revistos. A importância do ar saturado e não saturado para o CMT é estudada com o objectivo de alcançar um melhor entendimento acerca dos mecanismos físicos responsáveis pelo CMT. O ar não saturado e saturado na forma de correntes descendentes contribuem de forma determinante para o CMT e deverão ser considerados em futuras parameterizações do CMT e da convecção em nuvens cumulus. Métodos de agrupamento foram aplicados às contribuições do ar saturado e não saturado, analisando os campos da força de flutuação e da velocidade vertical da partícula de ar, concluindo-se a presença de ondas gravíticas internas como mecanismo responsável pelo ar não saturado. A força do gradiente de pressão dentro da nuvem é também avaliada, utilizando para este efeito a fórmula teórica proposta por Gregory et al. (1997). Uma boa correlação entre esta força e o produto entre efeito de cisalhamento do vento e a perturbação da velocidade vertical é registada, principalmente para as correntes ascendentes dentro da nuvem durante o episódio de convecção profunda. No entanto, o valor ideal para o coeficiente empírico c^*, que caracteriza a influência da força do gradiente de pressão dentro da nuvem sobre a variação vertical da velocidade horizontal dentro da nuvem, não é satisfatoriamente alcançado. Bons resultados são alcançados através do teste feito à aproximação do fluxo de massa proposta por Kershaw e Gregory (1997) para o cálculo do CMT total, revelando mais uma vez a importância do ar não saturado para o CMT.

keywords Vertical transport of horizontal momentum, tropical deep convection, 3D cloud resolving model, TOGA-COARE campaign.

abstract The aim of the proposed research is the investigation of vertical cumulus momentum transport (CMT) in tropical oceanic deep convective cloud systems. Our approach is to use a unique four month three-dimensional cloud resolving model (CRM) simulations of TOGA COARE - a major field experiment over the warm waters of the west Pacific. Emphasis is given to the study of cumulus-scale characteristics of convective momentum transport during the December westerly wind burst and a longer time interval encompassing this specific deep convective event. The analysis of vertical and time-height distributions are evaluated against observations confirming the good quality and reliability of CRM simulations. Good agreement with previous studies is found. The CMT sensitivity to spatial domain size is analyzed using two data sets produced by different horizontal domain sizes, suggesting a non-dependency of this field upon the dimension of model spatial domain. The skill of the downgradient mixing-length parameterization is tested, highlighting the tropospheric regions where the momentum fluxes are downgradient and where they are upgradient. The upgradient transports are linked to an unexpected poor correlation between the fields involved in this parameterization, suggesting that formulations of updraft cloud mass flux and entrainment should be revisited. The role of saturated and unsaturated drafts on CMT is investigated in an attempt to reach a better understanding of their underlying physical mechanisms. The unsaturated air via downdrafts, and the saturated downdrafts have an important contribution to CMT, and they must be considered in future CMT and cumulus convection parameterizations. Binning methods are applied to these saturated and unsaturated contributions, through the analysis of buoyancy force and vertical velocity fields, suggesting the presence of internal gravity waves driving the unsaturated air. The cloud pressure-gradient force is also evaluated using the theoretical formula proposed by Gregory et al. (1997), exhibiting a strong correlation to the product mean vertical shear by vertical velocity perturbation, especially in cumulus updrafts during the strong convective event. However, an optimal value for the empirical coefficient c^*, which characterizes the role of the cloud pressure-gradient force on the vertical variation of cloud horizontal velocity, is not satisfactorily achieved. Good results are accomplished by Kershaw and Gregory (1997) proposed mass flux approximation to total CMT, which has a fairly good performance in parameterization the total CMT and in identifying the regions of greater variability. Testing this particular approach revealed once again the important role of unsaturated air to the total CMT, which must be considered in future CMT and deep cumulus convection parameterizations.

Contents

ERRATA SHEET

This errata sheet lists errors and their correction for the doctoral thesis of Susana Margarida das Neves Mendes (nº 44786), titled "Cumulus Momentum Fluxes in Cloud-Resolving Model Simulations of TOGA-COARE", Doctoral Program MAP-FIS, Department of Physics,University of Aveiro, October 2011.

Location	*Error*	*Correction*
Resumo, line 4	"por modelo"	"por um modelo"
Resumo, line 20	"OS"	"Os"
Resumo, line 37	"corficiente"	"coeficiente"
Page x, 1.3, line 3	"reprrsents"	"represents"
Page xi, 3.1.5, line 2	"TOGA-COAR"	"TOGA-COARE"
Page xi, 3.1.9, line 1	"Total Cloud"	"total cloud"
Page 24, par. 2, line 1	1977	1976
Page 24, par. 4, line 6	"Radar sets"	"Radar data sets"
Page 25, par. 1, line 13	"ast"	"last"
Page 26, par. 2, line 8	"bug"	"big"
Page 31, par. 1, line 1	"-0.7"	"0.7"
Page 34, par. 1, line 3	"os"	"of"
Page 34, par. 2, line 15	"monotone"	"monotonic"
Page 36, par. 2 , line 9	"Ciesielski"	"Ciesielki (2003)"
Page 42, par. 2, line 2	"D256T120-S"	"D256T10-S"
Page 42, par. 3, line 2	"120 day"	"120-day"
Page 42, par. 3, line 2	"CRm"	"CRM"
Page 46, par. 1, line 2	"vertical shear"	"vertical wind shear"
Page 47, par. 2, line 10	"10^{-3}"	"10^{-3} (/s)"
Page 52, par. 1, line 3	"string"	"strong"
Page 52, par. 1, line 6	"are"	"area"
Page 53, par. 2, line 3	"et. Al"	"et al"
Page 57, par. 1, line 7	"Figure 3.1.15"	"Figure 3.2.2"
Page 61, par. 2, line 15	"(Fig. 3.1.18)"	"(Fig. 3.1.12)"
Page 67, par. 1, line 1	"Table 4.1"	"Table 4.1 and"
Page 69, par. 1	Paragraph repeated twice	Delete the paragraph
Page 70, par. 4, line 9	"binning w"	"binning"
Page 71, par. 1, line 5	"If"	"For"

Page 71, par. 1, line 6	“if”	“If”
Page 72, par. 2, line 10	“levels”	“level”
Page 78, par.1, line 5	“this”	“This”
Page 79, eq. (4.3)	$B = T\ \frac{T_d - \bar{T}_d}{\bar{T}_d}$	$B = g\ \frac{T_d - \bar{T}_d}{\bar{T}_d}$
Page 79, eq. (4.5)	$B = g - \frac{T'_d}{\bar{T}_d}$	$B = g\ \frac{T'_d}{\bar{T}_d}$
Page 79, par. 2, line 1	“Figures 4.2.8 and 4.2.9”	“Figures 4.3.1 and 4.3.2”
Page 79, par. 3, line 3	“Figures 4.2.8, 4.2.9 and 4.2.10”	“Figures 4.3.1, 4.3.2 and 4.3.3”
Page 83, par. 1, line 2	“and cloudy and”	“and the air”
Page 83, par. 1, line 7	“(Fig. 4.2.2)”	“(Fig. 4.3.2)”
Page 85, par. 2, line 2	“saturated”	“unsaturated”
Page 91, par. 1, line 2	“cases, for both”	“cases, and for both”
Page 92, par. 1, line 3	“times”	“time steps”
Page 110, par. 1, line 3	“fromc loud”	“from cloud”
Page 117, par. 3, line 6	“environmental vertical velocity”	“environmental zonal velocity”
Page 119, line 16	*Missing reference*	Add: Charney, J. G., and A. Eliassen, 1964: On the growth of hurricane depression. *J. Atmos. Sci.*,**21**, 68-75.
Page 122, line 8	*Missing reference*	Add: Palmen, E., and C. W. Newton, 1969: Atmospheric Circulations Systems. Academic, New York, 421 pp.

List of Tables

List of Figures

List of Acronyms

CAM	Community Atmosphere Model
CMT	Convective Momentum Transport
CRM(s)	Cloud-Resolving Model(s)
CRM CMT	Convective Momentum Transport simulated by the Cloud-Resolving Model
D256T10	Large Domain (256 x 256 km^2) for a 10-day Time period 3D data set
D256T10-S	Large Domain (256 x 256 km^2) for a 10-day Time period 1D/2D data set
D64T10	Small Domain (64 x 64 km^2) for a 10-day Time period 3D data set
D64T120-S	Small Domain (64 x 64 km^2) for a 120-day Time period 1D/ 2D data set
GCM	Global Climate Model
GKI97	Gregory, Keshaw and Inness, 1997
IFA	Intensive Flux Array
IOP	Intensive Observational Period
MJO	Madden-Julian Oscillation
OSA	Outer Sounding Array
QBO	Quasi-Biennal Oscillation
SAM	System for Atmospheric Modeling
SL76	Schneider and Lindzen, 1976
TOGA-COARE	Tropical Ocean-Global Atmosphere Coupled Ocean-Atmosphere Response Experiment
VS, VWS	Vertical Wind Shear
WWB(s)	Westerly Wind Burst(s)
ZW03	Zhang and Wu, 2003

Chapter 1

Introduction

1.1 Objectives of the present research

The role of cumulus convection in the climate system is of great importance, particularly at low latitudes and in summertime over midlatitude continents. Cumulus convection is a primary control on precipitation and tropospheric latent heating. Tropical convective clouds systems generate two thirds of the global precipitation and the associated latent heating is a principal driver of the atmospheric circulation. Cumulus convection also creates extensive clouds that affect earth's radiation budget, and vertically fluxes heat, moisture and other atmospheric constituents throughout the troposphere. It also induces vertical momentum fluxes, which will be the subject of this thesis.

Cumulus convection is a subgrid scale process; cumulus updrafts and downdrafts have width on the order of 1 km, much smaller than a climate model horizontal grid spacing of order 100 or more km. Thus cumulus convection needs to be parameterized (that is, its feedbacks with the grid-scale variables need to be represented in the climate model), which has proved to be a challenging problem. In addition to its interaction with large-scale circulations, cumulus convection interacts closely with other small-scale processes such as boundary-layer turbulence, cloud microphysics, and land-surface heterogeneity (Figure 1.1), adding to the parameterization challenge.

Most of the vertical transport of air within the tropical and subtropical troposphere is accomplished by a combination of deep (heavily precipitating) and shallow (lightly precipitating or nonprecipitating) cumulus convection. Deep and shallow cumulus convection frequently occurs in environments of large vertical wind shear. In these environments, convective updrafts can have a systematically different horizontal velocity

than convective downdrafts, resulting in a net vertical flux of horizontal momentum, or convective momentum transport (hereafter named by CMT). Because CMT is caused by small-scale updrafts and downdrafts, its average effect on global space and timescales cannot be measured directly. Hence, the effect of CMT on the global atmospheric circulation is still uncertain.

Studies of both idealized (*e.g*. Houze 1973, Schneider and Lindzen 1977), and general circulation (*e.g*. Zhang and McFarlane 1995) models have suggested that CMT has a important effect on mean zonal winds in the tropics and may also play a role in transient disturbances such as the Madden-Julian Oscillation (MJO), although few reliable observations exist over regions large enough to verify these modelling results. For these regions or larger scales, CMT can be inferred from an observational radiosonde network using a budget residual, although this involves considerable uncertainty deriving from the need to estimate the synoptic-scale pressure gradient force. Using this method, Carr and Bretherton, (2001) and Lin et al. (2005) showed over the western tropical Pacific, CMT tends to damp vertical wind shear in mean zonal winds or transient disturbances, such as the Madden-Julian Oscillation (MJO), on timescales of 5-10 days. It influences the tropical Hadley Circulation, rainfall and surface winds across the tropics (e.g. Richter and Rasch, 2008).

To represent these effects in climate models requires a parameterization of CMT. Diverse parameterizations have been proposed, but they are inadequately grounded in small-scale observations and modeling. The turbulent transport of momentum is different than for atmospheric constituents such as heat and moisture because due to pressure gradient forces, momentum is not conserved following fluid parcels even in the absence of mixing. Past studies suggest that even the sign of the transport depends on the degree and geometry of the cloud organization.

The major goal of this work is to improve our understanding of the vertical transport of horizontal momentum by deep convection over the tropical oceans, using a unique four month three-dimensional cloud-resolving model simulation of TOGA-COARE, a major field experiment over the warm waters of the west Pacific, characterized by extended periods of strong convection in strong vertical wind shear - ideal conditions for CMT, and extensive radiossonde, aircraft, and radar data sets which provide a good foundation for checking the quality of the CRM simulation. The author will investigate the statistical and the cumulus-scale characteristics of the convective momentum transport, examining the signs of the vertical transport of horizontal momentum during strong convection episodes, the sensitivity of CMT to grid resolution and domain size, the contribution from saturated and unsaturated up-and-downdrafts to CMT, and the accuracy of the physical assumptions made in some existing parameterizations of CMT.

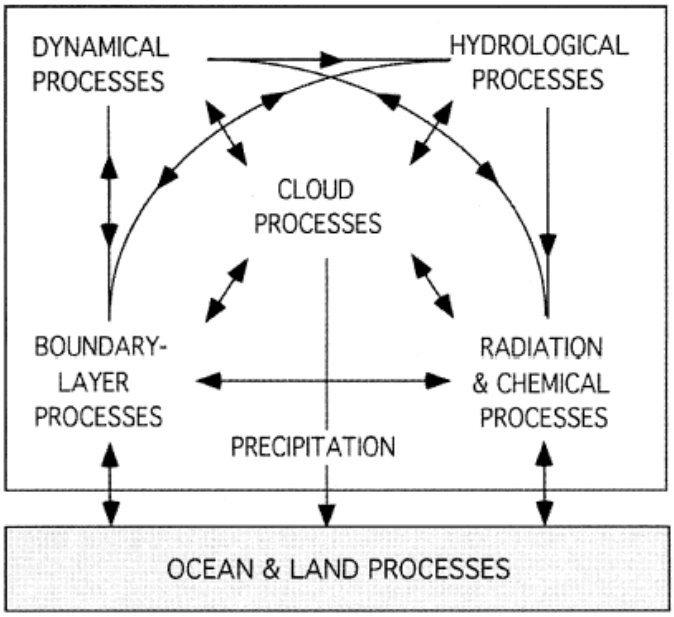

Figure 1.1. Interactions between various processes in the climate system (from Arakawa, 2004).

This dissertation will be structured in the following manner: Chapter 2 will briefly describe the cloud-resolving model used and the various TOGA-COARE simulations analyzed. In Chapter 3, the author will present time series of the most CMT-relevant variables and the comparison of CMT between two simulations characterized by different spatial domain sizes. Chapter 4 presents a test of the mass-flux approach to parameterization of CMT and evaluates the contribution of saturated and unsaturated up-and downdrafts to CMT. In Chapter 5, the author will discuss the prediction of U', the perturbation of the zonal component of the horizontal wind, and will evaluate the contribution of the pressure gradient force and entrainment terms for this prediction, assessing the issues related to these contributions. A direct comparison with the Gregory et al. (1997) CMT parameterization scheme using different choices for an adjustable coefficient called c^* and the deduction of an optimal value for c^*, defines the last section of Chapter 5. Chapter 6 will present a summary of the results, conclusions and directions for future work on the subject .

1.2 An Overview of Convective Momentum Transport

The first calculations using scale analysis and indirect estimates of vertical motion (*e.g*. Charney and Eliassen 1964, Palmen and Newton, 1969), suggested that CMT might be important to both steady and transient flows. Ooyama (1971) modelled CMT by assuming that momentum was mixed vertically like other scalars such as heat and moisture, and suggested that CMT should act to reduce the deep tropospheric shear in the environment. This transport is referred as downgradient transport, since momentum is transported from levels of high momentum to levels of low momentum. Schneider and Lindzen (1976) noted that even without turbulent mixing, the momentum of a cloud parcel can change during its ascent, due to cloud-scale pressure gradients produced by the relative horizontal motion of the cloud to its environment. This opened the possibility that CMT cloud act in a counter-gradient sense, that is, to increase the vertical shear.

During the 1970s, large-scale budget studies provided the first substantial observational determination of CMT. These studies estimated momentum flux convergence as the residual of a horizontal momentum budget over an array of sounding stations. This budget included contributions from large-scale horizontal momentum advection and storage, from Coriolis forces, and from pressure gradient forces. The challenge in this approach is that the residual term is typically much smaller than the other terms, so small uncertainties in these other terms (especially the pressure grandient force) magnify into big uncertainties in the CMT. Larger-scale budget residual studies, despite uncertainties, also suggest mesoscale convective organization impacts CMT. Momentum budgets have been constructed for shallow (*e.g*. Holland and Rasmussen 1973) and deep convection (*e.g*. Stevens 1979, Wu and Yanai 1994). Stevens (1979) calculated the momentum budget in easterly waves over the tropical Atlantic Ocean, in which deep convection was often organized in north-south oriented squall lines. In the wave troughs, where the convection was most vigorous, the author found downgradient CMT in the along-line direction with little CMT in the across-line direction, an anisotropy consistent with in-situ observations of squall lines. The synoptic-scale pressure gradient force was a major uncertainty in this study. Wu and Yanai (1994) examined mesoscale convective systems observed by storm- and mesoscale sounding arrays in Oklahoma and Kansas. Upper-tropospheric environmental wind shear was reduced by CMT in a mesoscale convective complex case and increased in a squall line case, suggesting once more the existence of a relationship between CMT and convective organization.

Sui and Yanai (1986) tried to overcome the uncertainties in inferring CMT from a

momentum budget residual by using a vorticity budget approach, in which the pressure gradient force does not appear. The curl of the momentum flux convergence is a source of vorticity which can be deduced as a budget residual, but this still requires a number of assumptions about conditions along the perimeter of the budget domain and in practice does little to decrease the uncertainty of the derived CMT.

Direct eddy-correlation measurements made by aircrafts and using winds derived from dual-Doppler radar analysis in field campaigns contributed significantly to understanding convective momentum transport. In a seminal observational study of momentum fluxes in squall lines, LeMone (1983) showed that in the across-line direction, CMT can act to increase the environmental wind shear. The tilt of the updraft produced mesoscale horizontal pressure gradients around the leading edge of the line that accelerated the updrafts rearward and downdrafts forward. This pressure distribution was exactly opposite to that predicted by flow around an obstacle and suggests that cumulus momentum fluxes can depend at a considerable degree in the convective organization. Many observational (*e.g*. LeMone et al. 1984, Flatau and Stevens 1987, LeMone and Jorgenson 1991, Gallus and Johnson 1992), and modeling (*e.g*. Soong and Tao 1984, Lafore et al. 1988, Gao et al. 1990) studies have confirmed the existence of countergradient or ugradient momentum fluxes in organized systems, of the sign opposite that predicted by mixing-length theory. These studies suggest that depending on the vertical profile of horizontal wind *U(z)*, two-dimensional convection in the atmosphere can transport *U*-momentum either up or down the vertical shear gradient, with the slope of the plane separating the leading-edge convection from the environment perhaps a better predictor of U-transport than the preceding environmental wind profile (the leading-edge is the intersection of a vertical plane normal to the convective line and the aforementioned plane). When the convective line is oriented to minimize the *U* shear (which is frequent), the evolution of *U* profile is such that the *U*-momentum is eventually countergradient.

It has been further found (LeMone et al. 1988a) that the CMT in a squall line is affected by the convection-induced perturbation pressure gradient resulting from the interaction between the main convective updraft and strong low tropospheric vertical shear of horizontal wind, as studied by Rotunno and Klemp (1982). However, in a 3D numerical study that included the neds of a squall line, Trier at al. (1998) found that the overall cross-line CMT was downgradient, even though was upgradient on the mid-plane. The convective-scale pressure perturbation is weaker in a low-shear environment, as observed by LeMone et al. (1988b). Therefore, nonsquall mesoscale convective systems that develop in a low-shear environment are unlikely to have upgradient CMT.

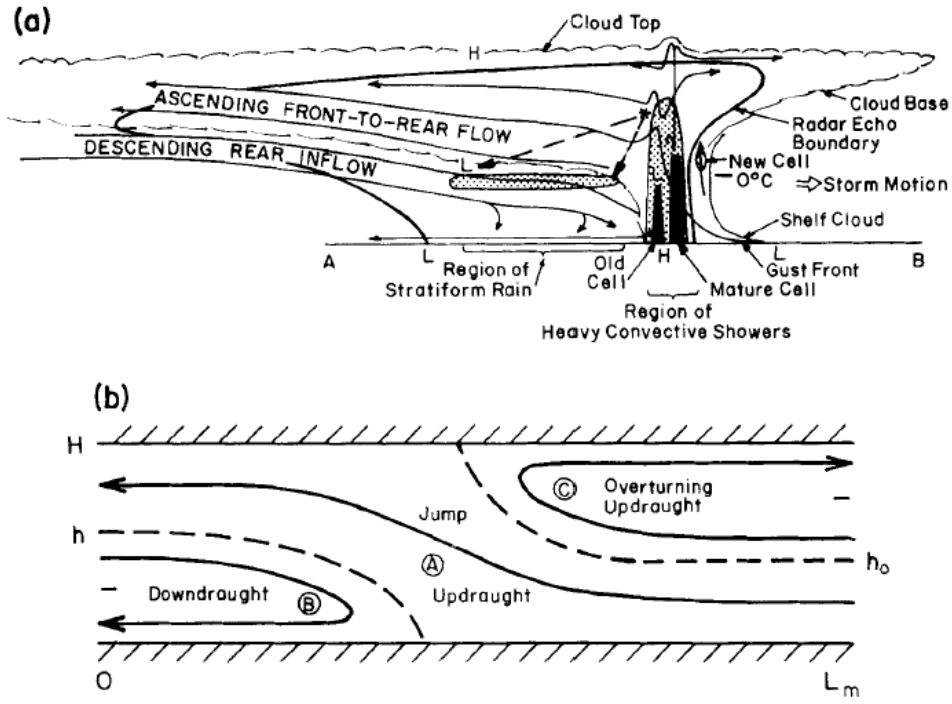

Figure 1.2. (a) Schematic diagram of the relative airflow and physical processes associated with a squall line mesoscale convective system. (From Moncrieff 1992, adapted from Houze *et al.* 1989). (b) Schematic diagram of the airflow in the stationary dynamical model showing the three flow branches, namely jump updraught (A); downdraught (B); and overturning updraught (C), part of the archetypal model. (From Moncrieff 1992).

Moncrieff (1992) developed an archetypical model which allowed for countergradient transport in organized systems by representing the effects of mesoscale circulations and the flow in the across-line direction by three branches: a descending downdraft, jump updraft, and overturning updraft (Figure 1.2). It is the dynamics and thermodynamics of the jump updraft responsible for the production of much of the countergradient transport. LeMone and Moncrieff (1993) found this model to be a good representation of line-normal CMT for quasi-two-dimensional convective bands, but its implementation as a parameterization of CMT in global models faces several challenges, e.g.: a) the closure for the model requires an assumption about the orientation of the convective lines which is not verified by observations, and b) as Trier et al (1998) study found, local countergradient transport in a squall line often does not generalize to larger space and timescales. Most current CMT parameterizations (e. g. Gregory 1997, Zhang and Cho 1991) are based on idealized models of flow partly entrained into and partly diverted around an isolated cumulus updraft. For most wind profiles, these parameterizations tend to produce largely downgradient fluxes, which result in a smoothing of the environmental wind profile.

1.3 Convective Momentum Transport in TOGA-COARE observational campaign

The Tropical Ocean-Global Atmosphere Coupled Ocean-Atmosphere Response Experiment (TOGA COARE, Webster and Lukas 1992) provided an attractive opportunity to examine reanalysis-based estimates of convective momentum transport (CMT). The TOGA COARE Intensive Observation Period (IOP) took place over the tropical western Pacific from November 1st 1992 to February 28th 1993. During this period soundings were launched every six hours at four stations on the perimeter of the IFA: Kavieng (-2.35N, 150.48E), Kapingamarangi (1.04N,154.48E), R/V Kexue#1 (-4.00N,156.00E), and R/V Shigan#3 (-2.00N,158.00E). Soundings were also taken at a more coarsely spaced network of surroundings stations. Upper-air sounding stations were located at the vertices of an Intensive Flux Array (IFA, Figure 1.3), and at a larger Outer Sounding Array (OSA). Additional sounding stations were also scattered throughout the region.

The vertical transport of horizontal momentum by cumulus convection was investigated in observations and model simulations of the Tropical Ocean Global Atmosphere Coupled Ocean-Atmosphere Response Experiment (TOGA COARE). Estimates of CMT were obtained from radar data, momentum budget residuals, and two-dimensional cloud-resolving models and CMT parameterizations. During the “active” periods of strong deep convection, there was often strong, deep vertical wind shear, lending hope that cumulus momentum fluxes might be sufficiently large to reliably estimate from a budget approach. However, Carr and Bretherton (2001) concluded that budget estimates of CMT were strongly affected by pressure-gradient uncertainties, with no clearly detectable signature of CMT above 850 mb. Below 850 mb, there was a tendency for downgradient transport.

Using radar data, Houze et al. (2000) concluded that the nature of mesoscale CMT during COARE varied with the phase of the Madden-Julian Oscillation. Qualitatively, transport of mid-level momentum by mesoscale downdrafts appeared to be downgradient during the onset of a December westerly wind burst, but countergradient during the period of strongest low-level westerlies.

Tung and Yanai (2002a and 2002b) investigated the general features of CMT and analysed specific case studies during TOGA-COARE. In their Part I, using sounding data, taken during the IOP, they studied the CMT effects through the residual of the large-scale momentum approach and concluded that CMT exhibits a profound transient behavior, modulated by the MJO and other disturbances. They also noted that, on average, the

vertical momentum transport is downgradient. Using the same approach with a specific objective analysis (2002b), they investigated the CMT associated with several convective events during TOGA-COARE. Their findings confirmed the role of CMT in modulating the large-scale motions, but also suggested its role in modulating the multiscale interaction among large-scale waves of various periods. Their analysis is very sensitive to their assumed pressure fields, which are quite uncertain, as Carr and Bretherton pointed out.

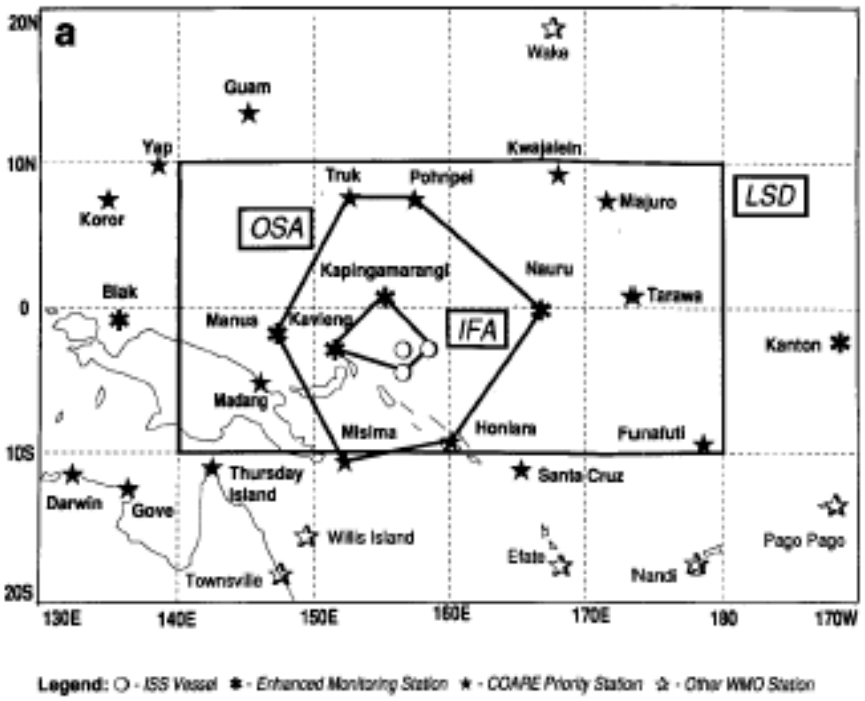

Figure 1.3. Measurement sites and study regions for the intensive observation period (IOP) of TOGA COARE. The legends beneath the panels refer to the symbols used to represent the observational platforms. This map reprrsents the entire COARE domain. The large-scale domain (LSD), the outer sounding array (OSA) and the intensive flux array (IFA) are outlined. (From Webster and Lukas 1992).

Zhang and Wu (2003), through a month-long 2D CRM simulation of TOGA-COARE convective systems using the observed large-scale forcing, tried to understand the role of the convection-induced perturbation pressure field in the momentum transport. To quantify the performance of the mass flux approximation, they computed the vertical profiles of the linear regression slopes at each level and the correlation coefficients between the pressure gradient and the product of cloud mass flux and vertical wind shear. The slope was close to -0.4 in the lower troposphere and slightly larger in the upper

troposphere, where they were forced to conclude that the value of 0.7 proposed by Gregory et al. (1997) was too large. They also showed that momentum transport by active convective downdrafts is small due to the weak downdraft mass flux. These authors noted that a 2D simulation, while more computationally affordable, may not be a good approximation for deriving CMT and pointed out that, long-term simulation with a 3D CRM should be the ultimate approach to investigate convective momentum transport in the future.

Chapter 2

The Cloud-Resolving Model and TOGA-COARE Simulations

2.1 The 3-dimensional cloud-resolving model

Over the last decades, cloud-resolving models (CRMs) have been widely used as a tool to assist in the formulation and testing of cloud parameterization schemes for larger-scale models. There are several advantages in using CRMs over observational data, one of the most important is that clouds are explicitly represented. Better spatial and temporal resolution is achieved. It is assumed that CRMs are able to represent the main features of convective storms correctly. These models have some skill in simulating a wide variety of cloud structures, giving some confidence that there is value in using these data to develop convective parameterization schemes for use in large-scale models (Kershaw and Gregory, 1997).

Cloud-resolving models can be used to estimate the momentum transports by deep convection, for different flow regimes and cloud organizations. As well as providing estimates of the net transport of momentum, the CRMs simulations provide details of the internal cloud-structure, such as the variation of horizontal wind with height within cloud and the structure and magnitude of the cloud pressure-gradient force can be estimated directly. Although the use of CRMs to study convective momentum transport has been increasing, this use has been limited to hours-long simulations of individual convection cases, often under idealized initial conditions, with the exception of Gray (2000), who computed the momentum transport by mesoscale convective systems over a 6-day period

in TOGA-COARE. Two-dimensional CRMs distort the air flow through and around convective clouds too much to reliably simulate convective mass transport, often leading to simulation of squall-line organization and upgradient convective momentum transport not observed in a 3-dimensional CRM of the same convective environment. Like Zhang and Wu (2003) stated long-term 3D CRM simulations should be used to investigate CMT. Many authors (e.g. Moncrieff, 1992) have stressed the importance of organized mesoscale circulations within convective storms, which may require a large computational domain to simulate. Thus it is important to test the sensitivity of CRM-simulated CMT to domain size.

The simulations available to perform this study were provided by the System for Atmospheric Modeling (SAM, Version 6.3), a CRM developed by Marat Khairoutdinov at Colorado State University and described in detail in Khairoutdinov and Randall (2003). The model solved non-hydrostatic and anelastic equations for a 3-dimensional, rectangular, cartesian horizontal grid over a flat and homogeneous surface. SAM used a staggered C-grid, in which divergence and pressure are calculated at the same point in order to avoid spurious oscillations in the velocity field. Surface fluxes were computed using Monin-Obhukov similarity theory from specified sea surface temperatures (SSTs), wind speed, humidity and temperature at the first model level above the surface. The CRM predicted the time variation of the three velocity components u, v and w, pressure p, and the three thermodynamic variables, liquid-ice static energy s_{li}, total non-precipitating water (vapor/cloud) q_t, and precipitating water q_r. s_{li} and q_t were adiabatically conserved even during vapor/liquid phase transitions but had sources due to the formation and evaporation of precipitation. The thermodynamic variables were transported with a monotonic advection scheme to prevent unphysical states associated with spurious oscillations.

The model used a single-moment bulk microphysical parameterization. Liquid–ice static energy was defined as $s_{li} = C_pT + gz - L_cq_{liq} - L_sq_{ice}$, where C_p is the specific heat of dry air at constant pressure, T is the absolute temperature (in Kelvin), g is the gravitational constant, q_{liq} is the mass mixing ratio of liquid phase hydrometeors, q_{ice} is the mass mixing ratio of ice phase hydrometeors, and L_c and L_s are the latent heats of condensation and sublimation, respectively. A diagnostic relationship based on temperature was used to differentiate the phases of non-precipitating hydrometeors (cloud liquid water and cloud ice) and precipitating hydrometeors (rain, snow and graupel). Cloud ice had a non-zero terminal velocity that depended on cloud ice water content and was derived from observations in Heymsfield (2003). A Smagorinsky-Lilly parameterization of subgrid turbulence (Smagorinsky 1963) was employed. No planetary boundary layer scheme, such as those used in global climate or weather models, was used

for vertical diffusion.

The CRM used three types of thermodynamic forcings: volumetric forcings (large-scale horizontal advection of sensible energy and moisture), surface forcings (either prescribed surface latent and sensible heat fluxes, or a prescribed sea surface temperature along with sea surface pressure) and a mean vertical velocity W_{ls} (detailed description in Blossey et al, 2008). The CRM radiation scheme was adapted from version 3 of the CAM (Community Atmosphere Model, a global climate model - GCM - from NCAR, the National Center for Atmospheric Research) provided for the CRM. Longwave and shortwave radiative heating rates transfer were computed in each model grid column approximately every three minutes. Water vapor, liquid water and the cloud ice (but not precipitating hydrometeors) were all radiative active.

Periodic boundary conditions were applied in the horizontal directions, and a rigid lid boundary condition was used at the top of the domain. The model vertical grid (in height coordinates) was composed of 96 layers, from surface to 30 km height, with grid spacings that increase smoothly from 75 m at the surface to a nearly uniform spacing of 250 m through the troposphere and then to 1 km in the Newtonian damping region, or sponge-region, in the top 30% of the model vertical domain, which prevented the reflection of upward-propagating gravity waves disturbances. In this damping region, perturbations of all prognostic variables from their horizontal mean were damped on a timescale that varies from two hours at 19 km to two minutes at the top of the domain. In the top two model layers, the mean thermodynamic profiles were nudged to specified observationally-derived profiles with a relaxation time scale of one hour.

The CRM generated two types of outputs, The first type, 3D outputs were instantaneous three-dimensional fields of basic model variables, including pressure (mbar), zonal wind component (m/s), meridional wind component (m/s), vertical wind component (m/s), pressure perturbation (Pa), radiative heating rate (K/day), absolute temperature (K), water vapor mixing ratio (g/kg), non-precipitating condensate (water plus ice) mixing ratio (g/kg) and precipitating water (rain plus snow) (g/kg). The second type, 2D/1D (referred hereafter as “statistics”) included horizontally-averaged variables and derived quantities such as vertical fluxes that were calculated within the CRM each time step, time-averaged and output periodically at a similar frequency as the 3D fields.

2.2. Description of TOGA-COARE CRM simulations

TOGA-COARE provided an excellent opportunity to investigate the convective momentum transport using cloud-resolving models, since, like previous observational campaigns, it collected large datasets from radiosonde, radar and aircraft instruments, some of which during strong convection events within substantial vertical wind shear environments.

Several CRM simulations, forced with TOGA-COARE data, using different choices of spatial and temporal domains, were performed by Dr. Peter Blossey at the Department of Atmospheric Sciences of the University of Washington. The forcings that provided the context of large-scale simulations were determined by large-scale atmospheric conditions over approximately (500 km)^2 region of the tropical west pacific Ocean centered on (2S, 156W) during the campaign (Ciesielski *et al.*, 2003). The mean horizontal velocity profiles in the model were nudged to the observed, time-dependent horizontal velocity profiles on a one-hour timescale. The SST and profiles of large-scale vertical velocity and horizontal heat and moisture advection were prescribed following Ciesielski (2003). Convection was initiated by a small (0.01 K) temperature perturbation at each grid point in the first five vertical levels of the cloud-resolving model. The temperature profiles were provided by TOGA-COARE soundings and derived from them in order to maintain the large-scale budget conditions. The surface moisture flux was computed interactively with the SSTs.

The TOGA-COARE simulations available to perform this research work employed three different domain sizes: 64 x 64 points, 96 x 96 points and 256 x 256 points, all with a resolution of 1 km in order to resolve deep convection and allow local parameterizations in the vertical to occur. Table 1 summarizes these experiments.

It is important to mention that the 96 x 96 simulation was only available at the end of this study, and due to this reason, most of the calculations were made using the smaller domain dataset, 64 x 64 km^2. Although this domain size compromises the ability to realistically simulate large mesoscale systems, it has little effect on the statistics of the convective cloud cover, as Blossey et al.(2008) showed. However, Blossey et al. (2008) did not investigate the sensitivity of CMT to the domain size.

The simulations using the smaller spatial domain were archived for two different periods: a 3-dimensional dataset D64T10, output every three hours for a 10-day period, and an hourly statistics dataset D64T120-S for the whole 120-day campaign period, starting on November 1^{st,} , 1992, and ending on February 28th, 1993. The 3D dataset for the 10-day period, contained instantaneous gridded values of fields described in previous

section, every three hours. A simulation using a larger domain, 256 x 256 km², covered the single 10-day period, from December 16th to 25th, 1992. The three-dimensional data, referred as D256T10, included the same atmospheric fields as D64T10, every two hours; the corresponding statistics dataset, D256T10-S, was calculated hourly.

Dr. Peter Blossey performed three more TOGA-COARE CRM simulations using an intermediate spatial domain size: 96 x 96 km² , for the whole 120-days period, generating: a) a 3-dimensional dataset – D96T120, containing the same atmospheric fields as D64T10 and D256T10, every four hours; b) a 2-dimensional dataset – D96T120-2D, where several atmospheric variables were hourly vertically averaged by the model; and c) a statistics dataset – D96T120-S, including hourly time-series of spatial averaged atmospheric fields as in the simulation D64T120-S.

All simulations described above were identically forced with the prescribed time-varying vertical motion, horizontal temperature and moisture advection, and relaxation of the domain-mean wind profile to observations on a one-hour timescale.

CRM Experiment	Timescale (days)	Domain-size (km²)	Dimensions	Number of Variables
D64T10	10	64 x 64	x, y, z	10
D64T120-S	120	64 x 64	z and/or time	> 100
D96T120	120	96 x 96	x, y, z	10
D96T120-2D	120	96 x 96	x, y	20
D96T120-S	120	96 x 96	z and/or time	>100
D256T10	10	256 x 256	x, y, z	10
D256T10-S	10	256 x 256	z and/or time	>100

Table 2.1. Brief summary of the relevant features of the data generated by the cloud-resolving model, and available for this thesis.

Chapter 3

General Features of 3D CRM Simulations of TOGA-COARE

This Chapter explores the vertical structure of convective momentum transport vertical behavior and its sensitivity to spatial resolution, comparing two 3-dimensional cloud-resolving model simulations of TOGA-COARE with different spatial domain sizes, for a common 10-day period, characterized by a strong convective event.

3.1 Time Series of CMT-relevant variables

The importance of the vertical transport of horizontal momentum was recognized when the investigation of the physical mechanisms underlying convection within cumulus clouds revealed the relative importance of cloud-scale dynamics and sub-cloud-scale turbulence as a central aspect of convective motions, whether these motions were located in low or mid-latitudes. The signature of these smaller scale convective motions on the larger-scale or mean atmospheric circulations was first investigated using Reynolds averaging, as described below. In this approach, the governing equations (Equation of Motion, Equation of State, Thermodynamic Equation, Mass Continuity and Water Continuity) are separated into mean-variable equations where the large-scale motions are identified and treated, and into perturbation equations for departures from the mean-state.

Following Houze (1994), Newton's second law of motion governing the motion of air in the atmosphere, may be written in the form:

$$\frac{D\vec{v}}{Dt} = -\frac{1}{\rho}\nabla p - f\vec{k}\times\vec{v} - g\vec{k} + \vec{F} \tag{3.1}$$

where t is time, $\vec{v}$ is the three-dimensional velocity of an air parcel or wind velocity that may be decomposed as $\vec{v} = u\vec{i} + v\vec{j} + w\vec{k}$ where $\vec{i}$, $\vec{j}$ are the unit vectors in the horizontal directions given by x and y, $\vec{k}$ is the unit vector in the height direction given by z, and u, v and w are the individual wind components. ∇ is the three-dimensional gradient operator and D/Dt represents the total derivative, which is the time derivative following an air parcel. The density and the pressure of the air are represented by ρ and p, respectively. The right-hand side of (3.1) represent the four forces acting on an air parcel: the pressure-gradient force, the Coriolis, gravitational and frictional accelerations, respectively. The magnitude of the gravitational acceleration is given by g, and f is the Coriolis parameter given by $2\Omega \sin\Phi$, where Ω is the angular speed of the earth's rotation and Φ is the latitude. Assuming the hypothesis that the large-scale environment is usually in hydrostatic balance, the equation of motion (3.1) may be written in a more convenient form in terms of the deviations of pressure and density from a hydrostatically balanced reference state, whose properties vary only with height. Denoting this reference state by the subscript o and the deviation from the reference state by *, the equation (3.1) is closely approximated by

$$\frac{D\vec{v}}{Dt} = -\frac{1}{\rho_0}\nabla p^* - f\vec{k}\times\vec{v} + B\vec{k} + \vec{F} \tag{3.2}$$

where B is the *buoyancy* defined as

$$B = -g\frac{\rho^*}{\rho_0} \tag{3.3}$$

Considering air motions in terms of deviations from an average over some arbitrary spatial volume of air (for example, a grid volume in a numerical model), any atmospheric field is expressed as the sum of its average value and its deviation

$$A = \overline{A} + A' \tag{3.4}$$

When the fields are decomposed in this way, the basic equations split into two sets: the *mean-variable equations*, which predict the behavior of the mean atmospheric fields or large scales, and the *perturbation equations*, which predict the departure from the mean state, representing the smaller scales. Applying this method to the equation (3.2), it yields to

$$\frac{\overline{D}\,\overline{\vec{v}}}{Dt} = -\frac{1}{\rho_0}\nabla\overline{p^*} - f\vec{k}\times\overline{\vec{v}} + \overline{B}\vec{k} + \overline{\vec{F}} + \vec{F} \tag{3.5}$$

where

$$\vec{F} \equiv \frac{1}{\rho_0}\left[\left(\nabla\bullet\rho_0\overline{u'\vec{v}'}\right)\vec{i} + \left(\nabla\bullet\rho_0\overline{v'\vec{v}'}\right)\vec{j} + \left(\nabla\bullet\rho_0\overline{w'\vec{v}'}\right)\vec{k}\right] \tag{3.6}$$

is the three-dimensional convergence of the eddy flux of momentum. It may be regarded as an effective force associated with the eddy motions of the air, while the fourth term on the right-hand side of (3.5) is a smaller-scale molecular friction force. The equation for the velocity perturbation is obtained subtracting (3.5) from (3.2). Referring to the equation (3.6) and to the classical definition of momentum, the object of this research was defined as

$$\rho\,\overline{u'w'} \tag{3.7}$$

the vertical transport of zonal momentum by deep convective clouds or, in an abbreviate way, the convective momentum transport. This work is totally focused on the vertical component of CMT , as seen is (3.7), rather than on the horizontal components since the horizontal accelerations associated with CMT should be much smaller than its vertical accelerations. Statistically, the convection varies very slowly in the horizontal, but rapidly and strongly in the vertical. In fact, in a periodic domain there is no systematic horizontal gradient of CMT.

Throughout time, several parameterizations were proposed to deal with the effects of this mechanical side of cumulus convection, in an attempt to assess the relative

importance of different variables to the vertical structure of CMT as well as to understand the physical processes underlying the vertical transport of zonal momentum. These parameterizations are divided into two main groups: the first one relying on mixing-length theory, where the vertical wind shear plays a fundamental role, and the second group related to the cloud mass flux field where the contributions from convective up and downdrafts are evaluated.

This research was initialized by surveying and comparing the available cloud-resolving model simulations, namely D64T10, D64T120-S and D256T10-S (refer to Table 2.1) and by analyzing CMT during strong convective events. We anticipate that strong CMT will be favored by extensive deep convection in strong vertical shear, so we look at surface precipitation (a measure of convective activity) and the vertical profile of zonal wind, since the strongest winds in this region tend to be in the zonal (east-west) direction. Figure 3.1.1 presents the time series of surface precipitation, accumulated hourly, for the whole period of 120-days divided into 10-day sub-periods. December 1992 was particularly active with two major events, one close to the Julian day 345 and a second one closed to Julian day 360. Figure 3.1.2 presents the rainfall for the specific 11-day period from 20th to 30th of December 1992, highlighting the second episode, the greatest one, on December 24th with a total of approximately 80 mm/day. This event is also attractive because it is included in the 10-day large-domain simulations.

Figure 3.1.3 shows a time-height cross-section of CRM-simulated zonal wind, for the whole 120-day period. Since the mean wind in the CRM is strongly nudged to observations, this is almost identical to the observed zonal wind.

From a climatological point of view, the tropical western Pacific lower troposphere along the equator is usually characterized by the presence of weak easterly winds with speeds between 1 to 5 m/s (Peixoto and Oort, 1992). These easterlies are frequently disrupted by westerly wind bursts (WWBs) occurring on intraseasonal timescales in a combination with the Madden-Julian Oscillation (MJO; Madden and Julian, 1971, 1972) or with extratropical interactions (Lin and Johnson, 1996). Below 10km, Figure 3.1.3 shows two prominent periods of strong low-level westerlies, commonly designated as westerly wind bursts (WWBs). Intense upper-levels easterlies aloft with magnitudes exceeding 30 m/s occupied the upper troposphere through most of the IOP and were modulated by the WWBs.

The first WWB, shown in detail on Figure 3.1.4, from mid-December to early January, starts to build up near the surface on December 15th, gradually increasing in magnitude and extending upward to the middle troposphere. By the end of this episode, the simulated westerly winds occupy most of the troposphere, reaching approximately 12 km of height. Maximum westerlies with speeds greater than 17 m/s occurred at low levels,

between 1.5 and 4 km of height, at the beginning of January. For the first WWB episode, the peak upper-atmospheric easterly wind of 33 m/s is in phase with the maximum westerly wind below. This WWB ends in mid-January, when low-level easterly winds start to develop extending to mid-troposphere, and strong westerlies above, in upper-levels.

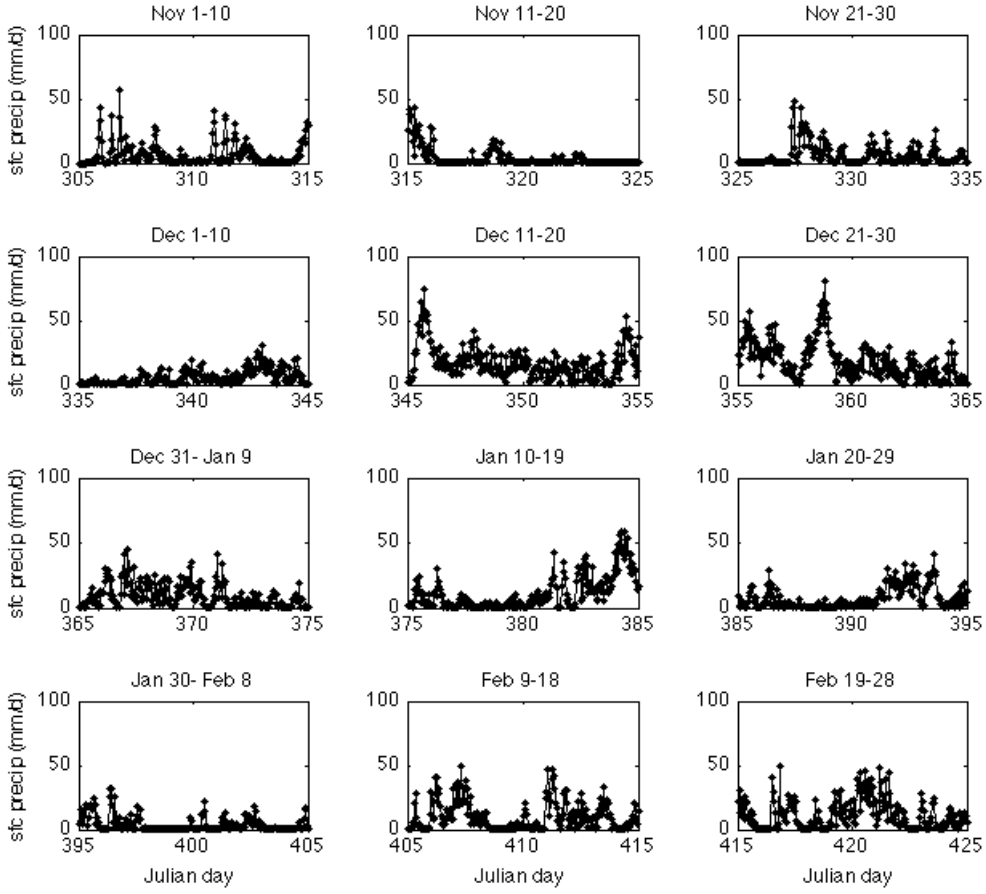

Figure 3.1.1. Surface precipitation (mm/day) for the whole period, 120 days, of TOGA-COARE, given by the simulation D64T120-S.

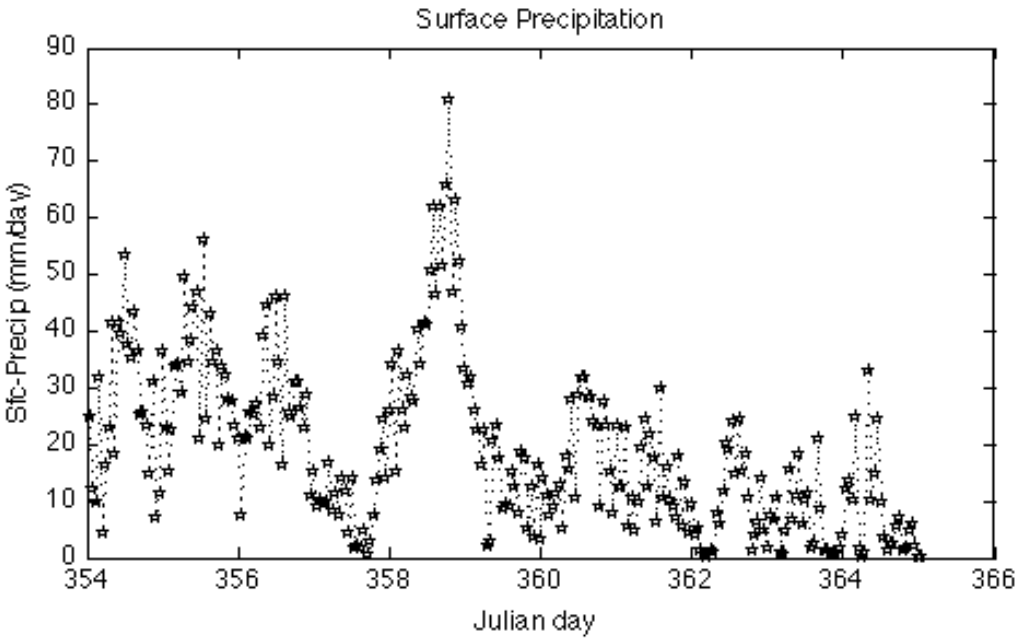

Figure 3.1.2. The surface precipitation field (mm/day) for a 11-day period, from December 20th to 30th, 1992, spatially averaged by the model over the small domain 64 x 64 km².

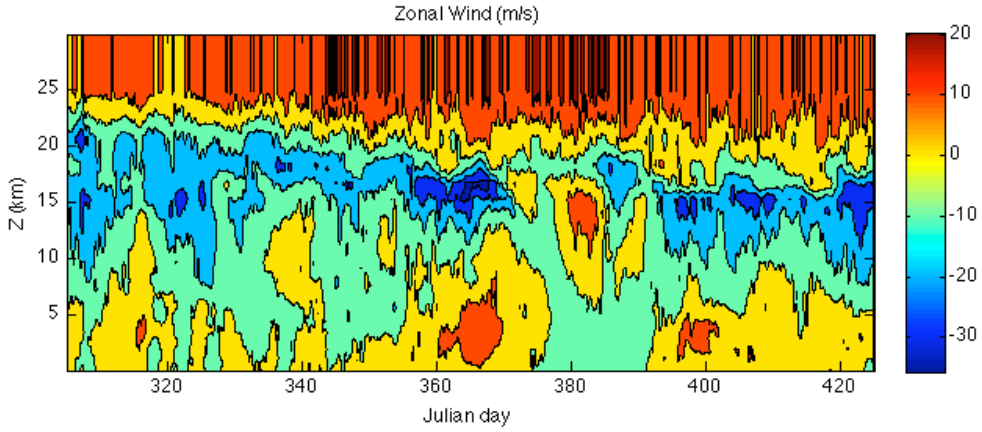

Figure 3.1.3. Time-height cross-section for zonal wind (m/s) during IOP, spatially averaged over the small domain, simulated by D64T120-S.

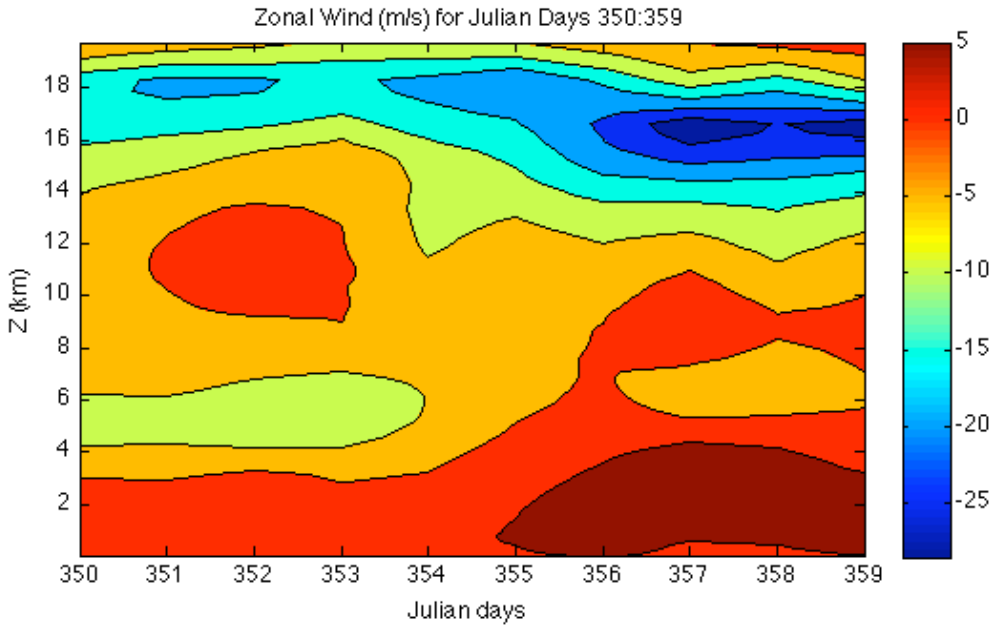

Figure 3.1.4. Time-height cross-section for zonal wind (m/s) provided by the simulation D64T10, a 3-D dataset, for a sub-period of 10 days, including the deep convective event occurred in December 24th.

The 2nd WWB event occurs at early February, initiating from the lower troposphere and gradually increasing in depth, and characterized by smaller wind magnitudes and a shorter duration. Following this WWB event, the Australian monsoon moves in maintaining the westerly flow below 6 km, from mid-February to the end of the month (Tung and Yanai, 2002a). Above 20 km, in the stratosphere, most of the IOP features very strong westerly winds, a signature of the westerly phase of the quasi-biennial oscillation (QBO) (Lin and Johnson, 1996). All these features are present in the vertical profile for the IOP mean zonal wind, Fig. 3.1.5. The low troposphere features westerly winds extending upward to 6 km at which easterly winds start to dominate the middle and upper troposphere, reaching a maximum below the tropopause, at the jet stream level. Above 15 km westerlies dominate the vertical model domain.

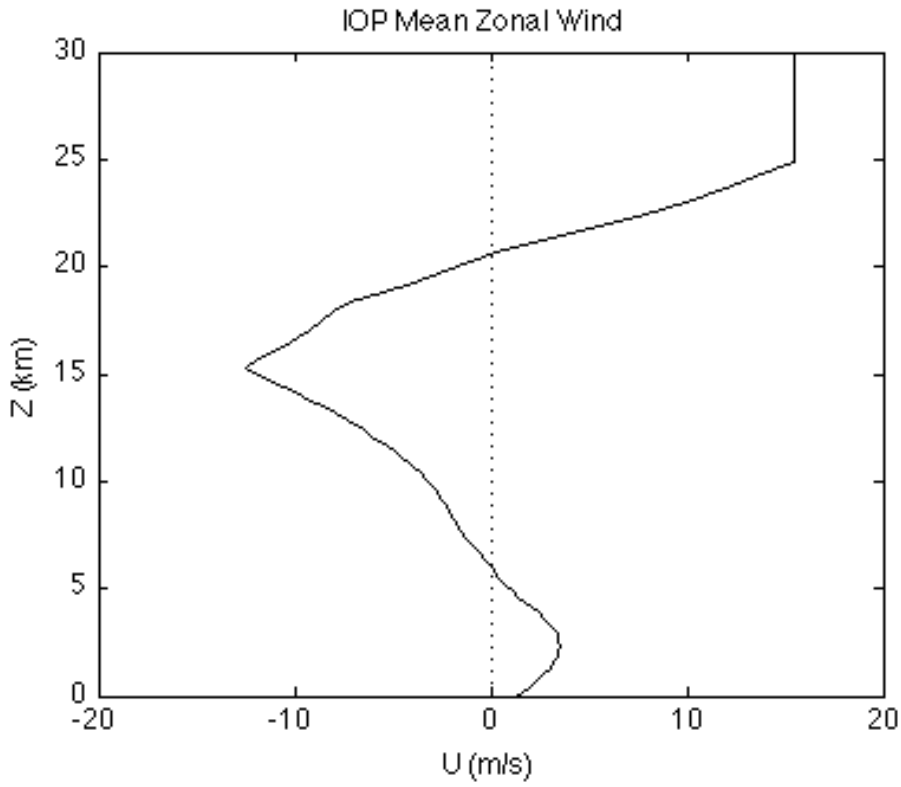

Figure 3.1.5. Vertical profile of mean zonal wind simulated by D64T120-S, averaged over the whole 120-days of TOGA-COARE.

The "Mixing-Length" hypothesis was the first to suggest a simple relationship between the CMT and the vertical wind shear. It became the basis of several CMT parameterizations in weather and climate models. Mixing-length theory suggest that as with molecular viscosity, the momentum flux is given by $-K_m (\partial \bar{U}/\partial z)$, where K is a positive eddy exchange coefficient for momentum and $\bar{U}$ is the mean zonal wind. The exchange coefficient is the product of a lengthscale (a typical large eddy size, perhaps 1-3 km for deep cumulus clouds) and a velocity (the eddy turnover velocity, which one could estimate as 1-5 m/s for deep cumulus). This approach will always predict downgradient momentum flux from levels of larger zonal velocity to levels of smaller zonal velocity. Thus, mixing length theory predicts that the vertical shear would be an indicator of regions of positive or negative convective momentum transport. The IOP-mean environmental wind shear profile in Figure 3.1.6 would then drive a region of positive momentum flux from above the cloud base up to the upper troposphere, and two regions of negative momentum flux beneath the cloud base and above the tropical tropopause. This prediction will be tested using CRM-simulated CMT profiles later in this section.

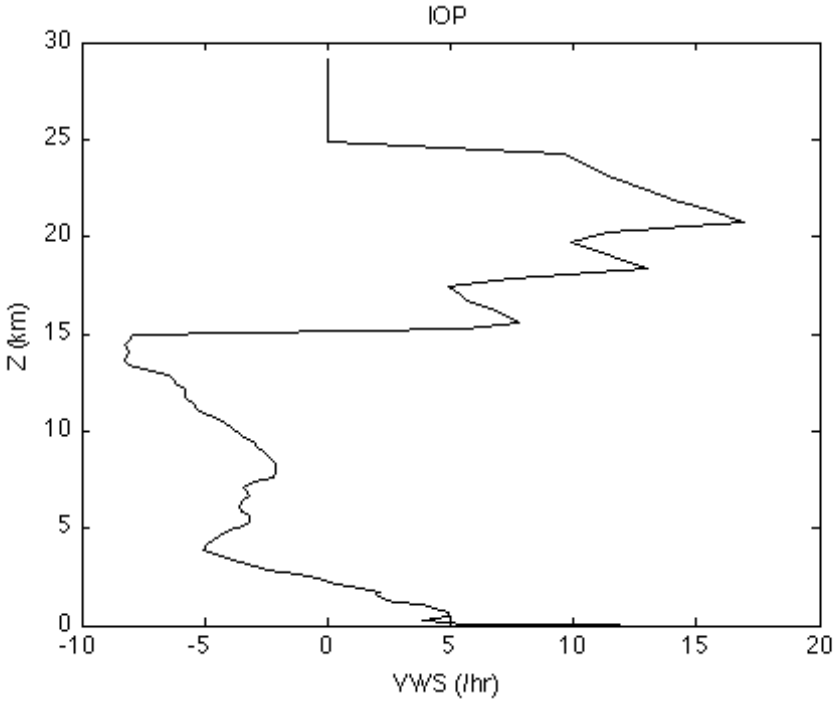

Figure 3.1.6. Vertical profile of the vertical wind shear (hr^{-1}) simulated by the D64T120-S dataset, averaged over the small domain and over TOGA-COARE IOP.

The vertical profile of the vertical wind shear, in Figure 3.1.6., averaged, by the model, over the whole spatial domain and over the 120-days period (IOP), shows two distinct regions of vertical wind shear within the atmospheric column. Most of the troposphere is dominated by negative values, related to the variations of zonal wind signs: westerly and easterly phases, and at 15 km, where the easterly jet stream is located, a rapidly inversion occurs starting to increase upward and being positive up to 25 km, in the stratosphere, where westerly winds dominate. In Figure 3.1.7, positive values of vertical wind shear dominate the IOP, with a few exceptions coincident with the low-levels westerlies in the first 60 days and the upper-levels westerlies, after Jd 380. The typical IOP-mean zonal vertical wind shear in the troposphere has magnitude 10^{-3} (/s), similar to other environments in which are *in situ* observations of CMT (for example, LeMone et al., 1984, 1988).

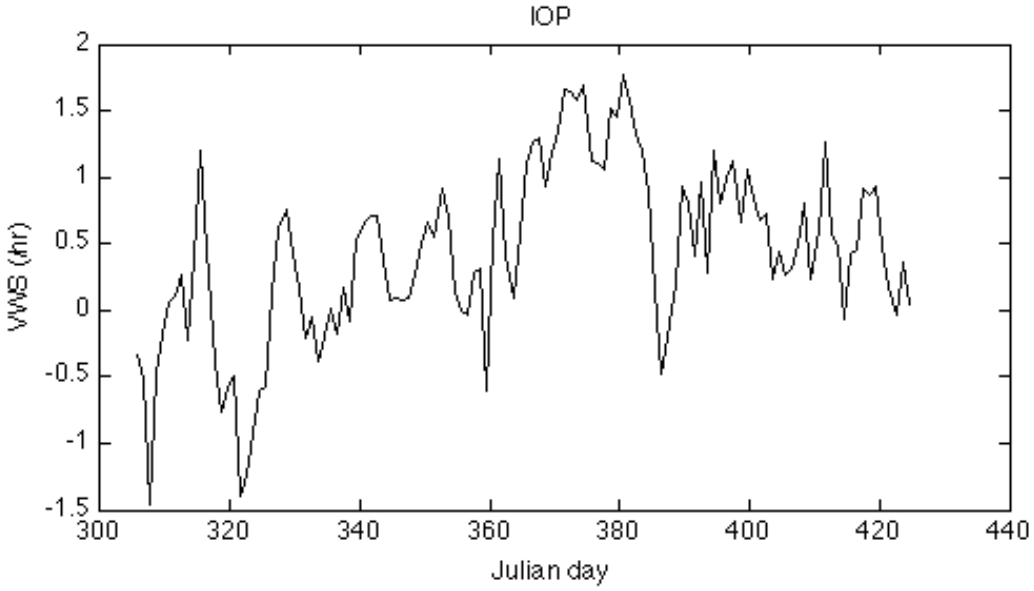

Figure 3.1.7. Time series of vertical wind shear (hr^{-1}), given by simulation D64T120-S, averaged over the whole atmospheric column.

A time-height of the prescribed vertical wind during Julian days 350-359 (Figure 3.1.8.) shows nearly continuous lower-tropospheric mean ascent and two periods of deep ascent on Julian days 355 and 358 reaching up to 14 km preceding the most intense low-level westerlies. These periods correspond to the strongest deep convection and surface precipitation during the period.

The total cloud mass flux field is intrinsically related to the vertical wind field through the relationship $M_c = \rho\sigma_c w_c$, where ρ is the air density, σ_c is the cloud fractional area and w_c is the average vertical velocity in cumulus clouds. The total cloud mass has two major contributions: from updrafts $M_u = \rho\sigma_u w_u$, and from downdrafts $M_d = \rho\sigma_d w_d$, being designated by convective updraft mass flux and convective downdraft mass flux, respectively. The most important role of the updraft and downdraft mass fluxes is that their vertical variations are directly linked to the rate of entrainment and detrainment at the cumulus cloud boundaries, and entrainment and detrainment have a significant effect on momentum flux, being one of the physical mechanisms underlying the vertical transport of horizontal momentum by deep convection.

Since the cloud mass flux (Mc) depend on the total cloud fraction, which helps to identify the location and the cloud type simulated by the CRM, the later will be analyzed first, using the simulation D64T120-S. The time series for the total cloud fraction and the fractional area of cloudy updrafts, model-spatial averaged, during IOP are present in Figure 3.1.9. In this plot, several peaks of the total cloud fraction are shown, the majority

in phase with the WWB events registered during IOP. The major peak happens on Jd 358, like the surface precipitation and vertical wind, at the onset of the most intense WWB in TOGA-COARE. More than 15% of the model atmospheric column was occupied by clouds during the time corresponding to deep convective days and/or WWB events initiated at the lower-levels or mid-levels (Julian day 380). During easterlies (lower-levels), less than 5% of the column is occupied, consistent with observations.

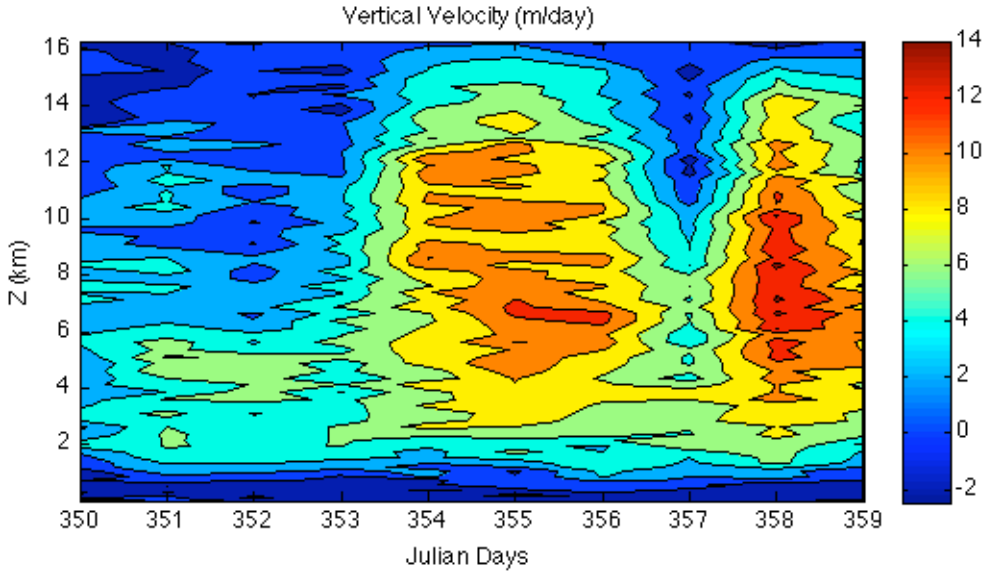

Figure 3.1.8. Time-height cross-section of vertical wind (m/day), for the 10-day period, from Dec 16th to 25th, 1992, as simulated by the 3-D dataset D64T10.

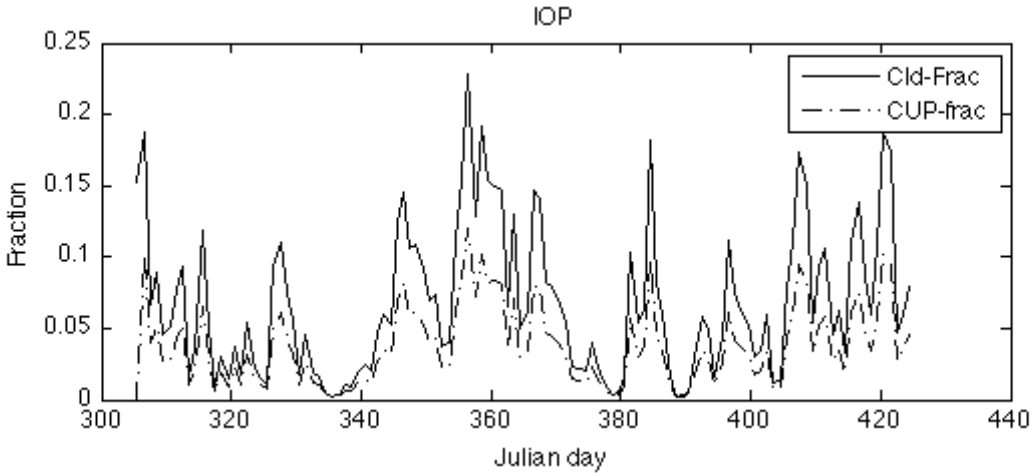

Figure 3.1.9. Time series of the Total Cloud area fraction (solid line) and the fractional area of cloudy updrafts (dash-dotted line), simulated by D64T120-S, for the whole TOGA-COARE period, 120 days.

Throughout IOP, the saturated updraft area fraction remains approximately half of the total cloud fraction; the remainder of the cloud is composed of saturated downdrafts. Figure 3.1.10 highlights the similarity between the vertical structure of both fields.

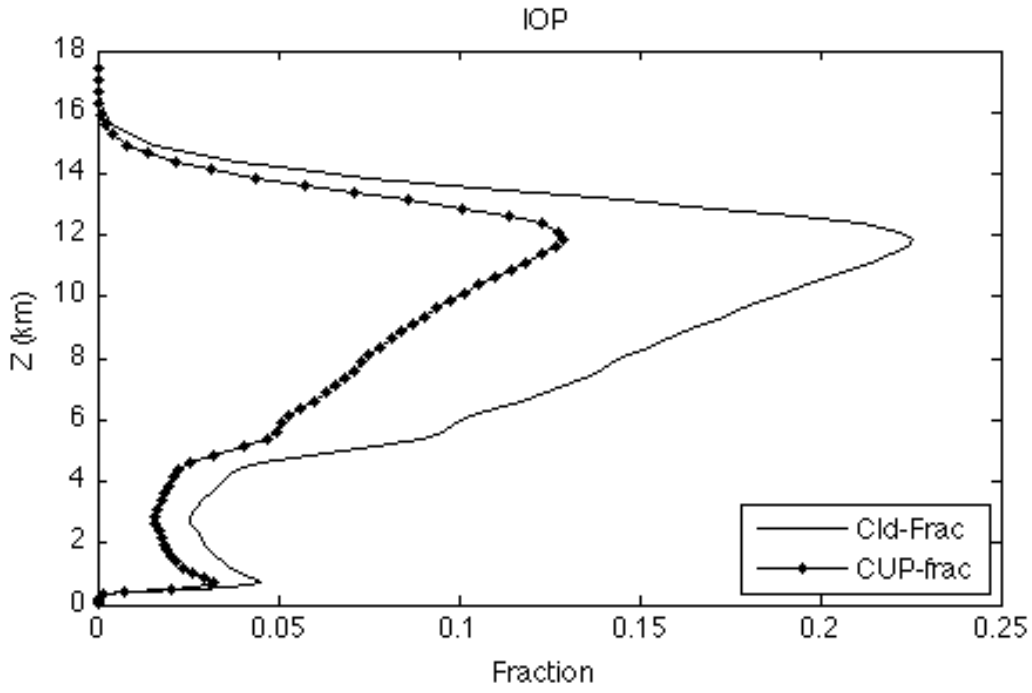

Figure 3.1.10. Vertical profiles of total cloud area fraction (solid line) and the fractional area of cloudy updrafts (dotted line), as simulated by D64T120-S, averaged over IOP: 120 days.

Above 12 km, in the stably-stratified tropopause transition layer, both fields decrease rapidly up to 16 km where no clouds are observed. Since the vertical profiles are averaged over the whole TOGA-COARE period, we conclude that the IOP was dominated by extensive upper-layer cirrus anvil clouds. In a 30-day 2-D CRM TOGA-COARE study, Zhang and Wu (2003, hereafter ZW03) found similar values for the total cloud fraction in the lower troposphere, but the vertical structure of cloud fraction differed greatly from our simulations. This might be due to dimensionality or a their use of a different ice microphysical treatment than ours.

The simulation D64T120-S provides three different cloud mass flux ($kg/m^2/s$) fields: the updraft cloud mass flux (McUP), the downdraft saturated cloud mass flux (McDD) and their sum, the cloud mass flux (Mc).

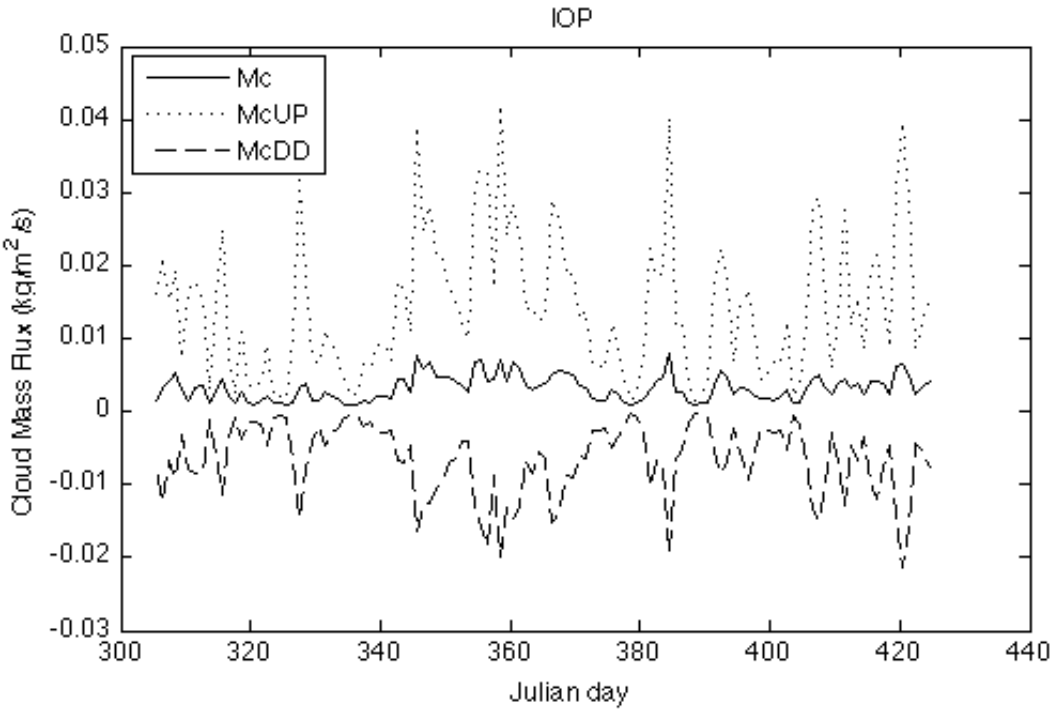

Figure 3.1.11. Time series of simulated total cloud mass flux (kg/m²/s, solid line), the updraft cloud mass flux (dotted line, kg/m²/s) and the downdraft cloud mass flux (dashed line, kg/m²/s), given by D64T120-S, for the TOGA-COARE IOP.

The evolution, both vertical and temporal, of these atmospheric variables is shown in Figures 3.1.11 and 3.1.12. As seen from Fig. 3.1.11. the total cloud mass flux is positive throughout the IOP, but very low in magnitude, due to strong compensation between McUP and McDD. The time evolution of updraft cloud mass flux, McUP, resembles that of cloud area fraction (Figure 3.1.9), suggesting that variations in area fraction are more important than those in updraft vertical velocity. Like the updraft cloudy area fraction and the total cloud area fraction, McUP and McDD peaks coincide with the onset of strong low-level westerlies. The strongest peaks in both McUP and McDD are on Julian day 358, consistent with the surface precipitation and vertical wind maxima.

The vertical profiles of IOP-averaged Mc, McUP and McDD, in Figure 3.1.12, show features analogous to those found in Fig. 3.1.11. The guiding signature in Mc belongs to McUP, but this is strongly compensated at most levels by McDD. Right above the surface Mc registers a minimum value without apparent relationship to neither McUP nor McDD. This minimum is located within the boundary layer and it is connected to a minimum in the mean vertical wind within the downdraft core, suggesting the presence of unsaturated downdrafts, which may be a result of evaporation of precipitation within the downdraft,

underneath the cloud base. Mc has a maximum value around cloud base associated with shallow cumulus clouds, decreasing slowly until 3 km of height indicating some detrainment happening at these levels. Above this height, Mc slightly increases (suggesting entrainment) until it reaches another maximum value around 11 km of height.

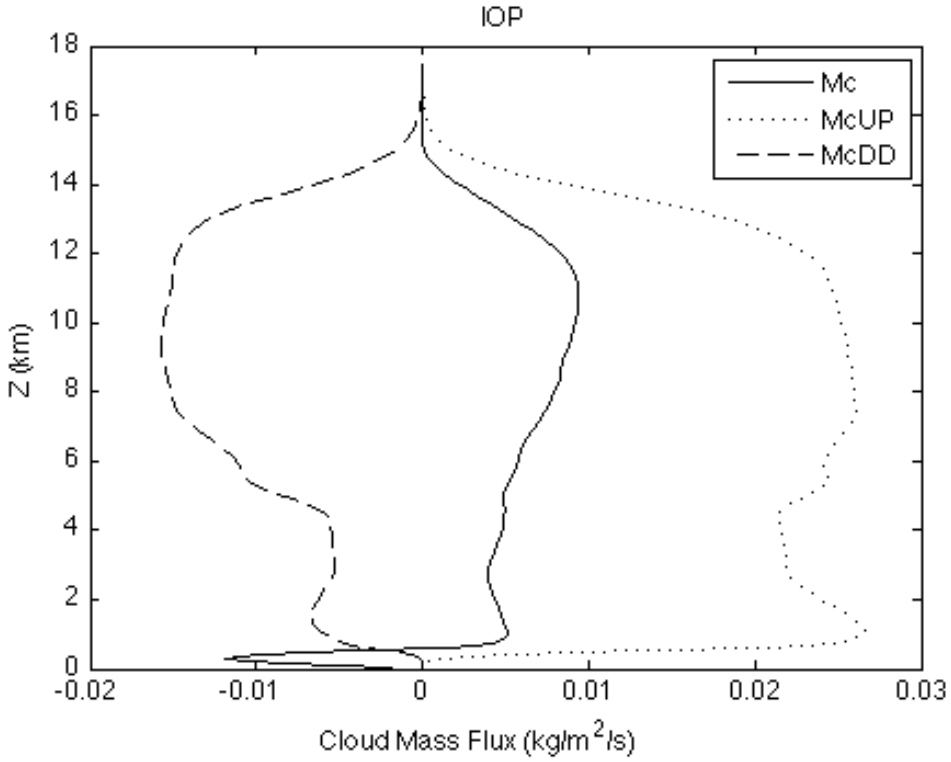

Figure 3.1.12. Vertical profiles of the total cloud mass flux (solid line), the updraft cloud mass flux (dotted line) and downdraft cloud mass flux (dashed line), given by the D64T120-S dataset, averaged over the TOGA-COARE IOP.

The simulated cloud mass flux profiles are somewhat different than those obtained by other authors using different large-scale forcing conditions, for instance ZW03 and Gregory et. al. 1997 (hereafter GKI97). In their tropical case study, GKI97 found that their CRM-simulated McUP peaks at the cloud base, but unlike in Figure 3.1.12., it declines throughout the troposphere. ZW03, in their 2D CRM study of a 30-day period of TOGA-COARE, also found a maxima in McUP at the cloud base, decreasing slowly upward to 4 km, followed by a fast decline up to 14 km.

We conclude this section with vertical profiles (Figure 3.1.13) of the vertical transport of the zonal component of horizontal momentum (magnitude of 10^{-2}) and mean

zonal wind, as simulated by D64T120-S, averaged over the spatial domain and over the IOP. This momentum flux is due to all forms of motion, including unsaturated turbulence (important near the surface) and gravity waves, but since cumulus clouds are the main energy source for small-scale motions, we will use the term CMT to describe the entire eddy momentum flux horizontally averaged across the computational domain. The mean zonal wind profile is nearly anticorrelated to the CMT profile. Up to 5 km, westerlies dominate and CMT is negative. Between 6-20 km, easterly winds and positive momentum fluxes dominate. In the stratosphere above 20 km, CMT is weak. The vertical profile of the mean vertical wind shear (Fig. 3.1.6) fails to identify the layer of negative momentum fluxes below 6 km and the positive momentum fluxes in the upper levels. This conclusion is at apparent odds with the hypothesis of downgradient transport but is in agreement with findings by LeMone (1983,1983 and 1988) and others. However, to fully test the downgradient transport hypothesis, the momentum transport must be split into cloudy updrafts and downdrafts and unsaturated motions, and the time-dependent evolutions of the flow must be considered. This subject will be further discussed on the next chapter.

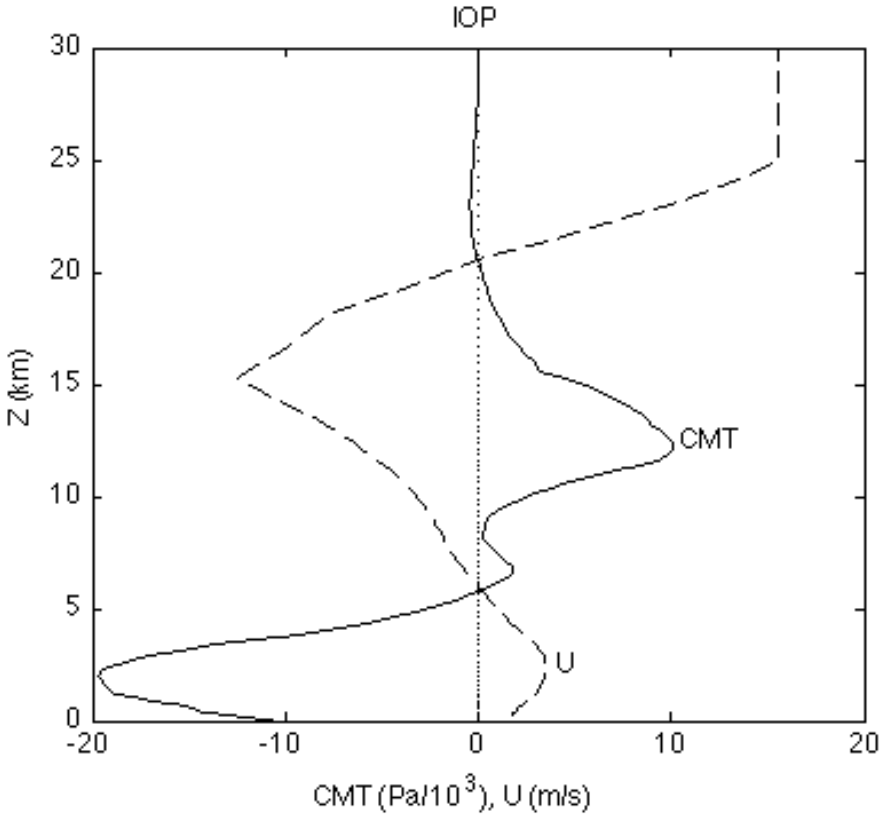

Figure 3.1.13. Vertical profiles of CMT (10^{-3} Pa) and mean zonal wind (m/s), provided by D64T120-S dataset, averaged over the TOGA-COARE IOP.

3.2 Comparison between small and large spatial domains of simulation

Kershaw and Gregory (1997, hereafter KG97) carried out some sensitivity tests to aid assessment of the accuracy of their cloud-model results. They tested the effects of increasing horizontal resolution, of increasing vertical resolution in the boundary layer, the sensitivity to the turbulence parameterization and the effects of including a representation of the ice phase, in all cloud-model simulations of two particular case studies, concerning the horizontal momentum transports and all variables related to it. They concluded that, an increase in the domain size has a very low impact on simulations. None of the experiments showed any sign of mesoscale or two-dimensional organization of the convection (such as a squall-line formation) and the momentum transports were very similar in all simulations. Nevertheless, this influence has not been properly explored when cloud-model studies are concerned. The sensitivity of several CMT-relevant variables to the CRM horizontal domain size is addressed in this section. Two datasets are available to perform this analysis: D64T120-S and D256T10-S (for more information please refer to Table 2.1), the first for a smaller domain 64 x 64 km² in the horizontal and the second for a larger domain size 256 x 256 km², both with the same horizontal grid-spacing of 1 km. The larger spatial domain simulations are available only for a period of 10 days, Jd 350:359 (Dec 16th to 25th , 1992).

Figure 3.2.1 shows the surface precipitation time series obtained in the small and large domain simulations. Overall, these time series are very similar, both showing the three large convective episodes on December 20th, 21st and 24th. Some differences are noteworthy. The large spatial domain simulation D256T10-S starts to produce rainfall only at the end of the first day of simulation. This is due to the fact that D256T10-S is initialized with a nearly horizontally homogeneous thermodynamic state at the Jd 350 (December 16th), and a spin-up period of nearly a day is required to produce near-equilibrium statistics of cumulus convection and rainfall; thus we ignore the first day of simulation. The small-domain simulations have noisier rainfall profiles because they contain far less convective storms at each time.

The mean zonal wind and CMT vertical profiles over Jd 351-360 are shown in Figure 3.2.2. Because the domain-mean horizontal winds in both simulations are strongly nudged to the observed IFA-mean profiles, they are essentially identical. The time-mean CMT is almost identical between runs, but is slightly less negative in the small-domain run in the lower troposphere. This agreement suggests that the 64 km domain is adequate for simulating the CMT profile, and that mesoscale circulations not simulated in such domain must therefore not being playing a dominant role in producing CMT. The right panel in Figure 3.2.2 displays the vertical profiles of the all cloud mass fluxes available in D64T120-S and D256T10-S CRM simulations. As seen in time series of rainfall and CMT vertical profiles, the McUP, Mc and McDD vertical behaviors are very much alike, for both simulations. The large spatial domain simulated magnitudes are lower than those for the small domain dataset, except for the total cloud mass flux (Mc), where the magnitude is slightly superior, due to the fact that McUP and McDD contributions are also smoother, not emphasizing the significant changes of these fields over the vertical. Nevertheless, the overall view suggest a good match between both simulations.

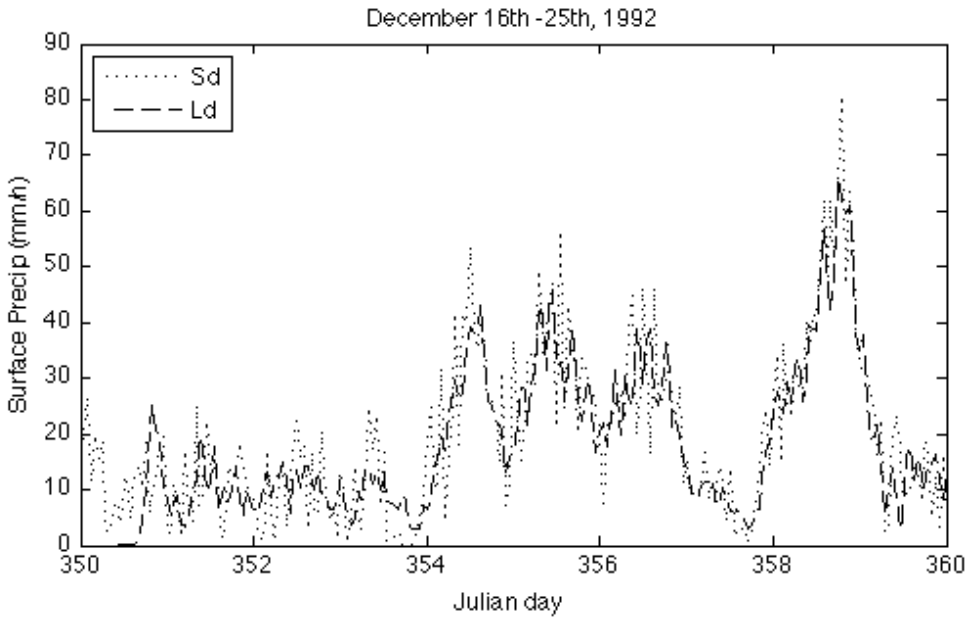

Figure 3.2.1. Time series of surface precipitation (mm/hr), for the common 10-day period (Jd 350:359, December 16th to 25th, respectively), obtained by the small domain simulation D64T120-S (Sd, dotted line) and by the large domain simulation D256T10-S (Ld, dashed line).

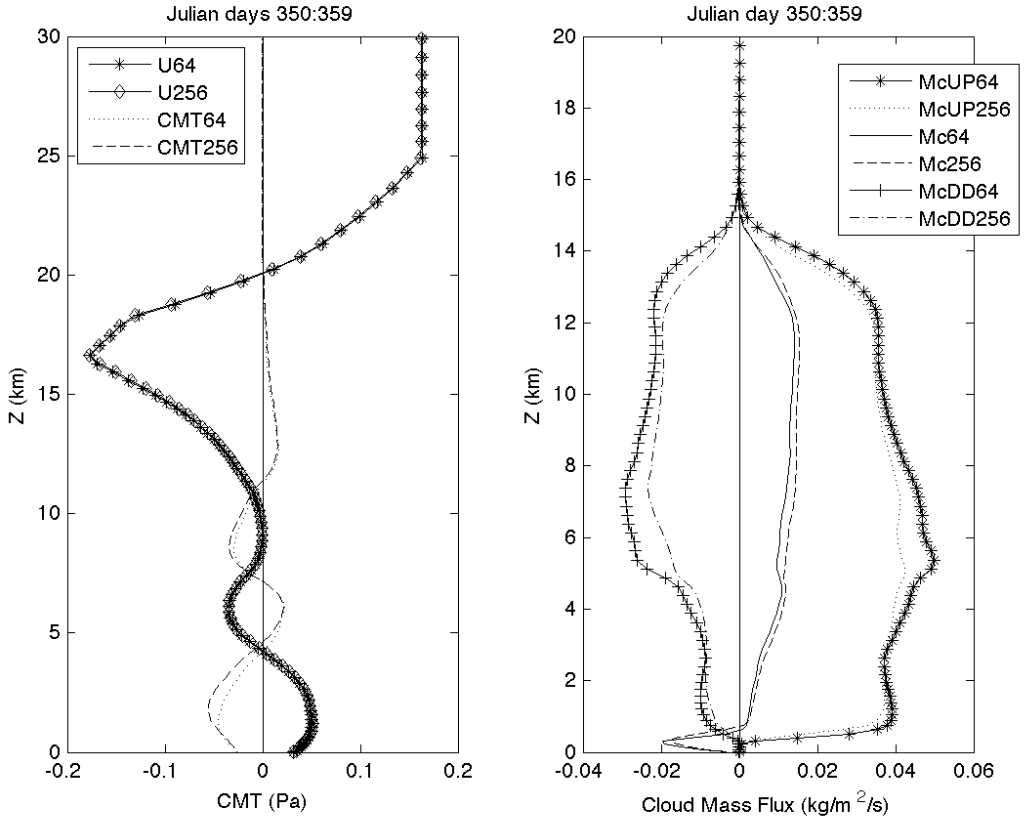

Figure 3.2.2. *Left:* vertical profiles of mean zonal wind U (m/s/100), given by the simulations D64T120-S (U64, small domain, starred solid line) and D256T10-S (U256, large domain, diamond solid line) and CMT (Pa), obtained by the simulations D64T120-S (CMT64, dotted line) and D256T10-S (U256, dashed line). *Right:* vertical profiles of updraft cloud mass flux McUP64 and McUP256 (kg/m²/s), of total cloud mass flux Mc64 and Mc256 (kg/m²/s) and of downdraft cloud mass flux McDD64 and McDD256 (kg/m²/s), provided by the small domain simulation D64T120-S and by the large domain simulation D256T10-S; averaged over the common 10-day period.

Figure 3.2.3 exhibits the time and vertical structure of total Mc and CMT, for both horizontal domains. The conclusions lead by the vertical profiles are also confirmed here, highlighting the much greater small-domain CMT variability over time and height. Once more, confidence that the 120-day small domain run is representative of a larger domain CRM simulation even though the small domain cannot support mesoscale organizations of more than 64 km wavelength is achieved.

The comparison between small and large domain simulations will continue to be discussed in Chapter 4.

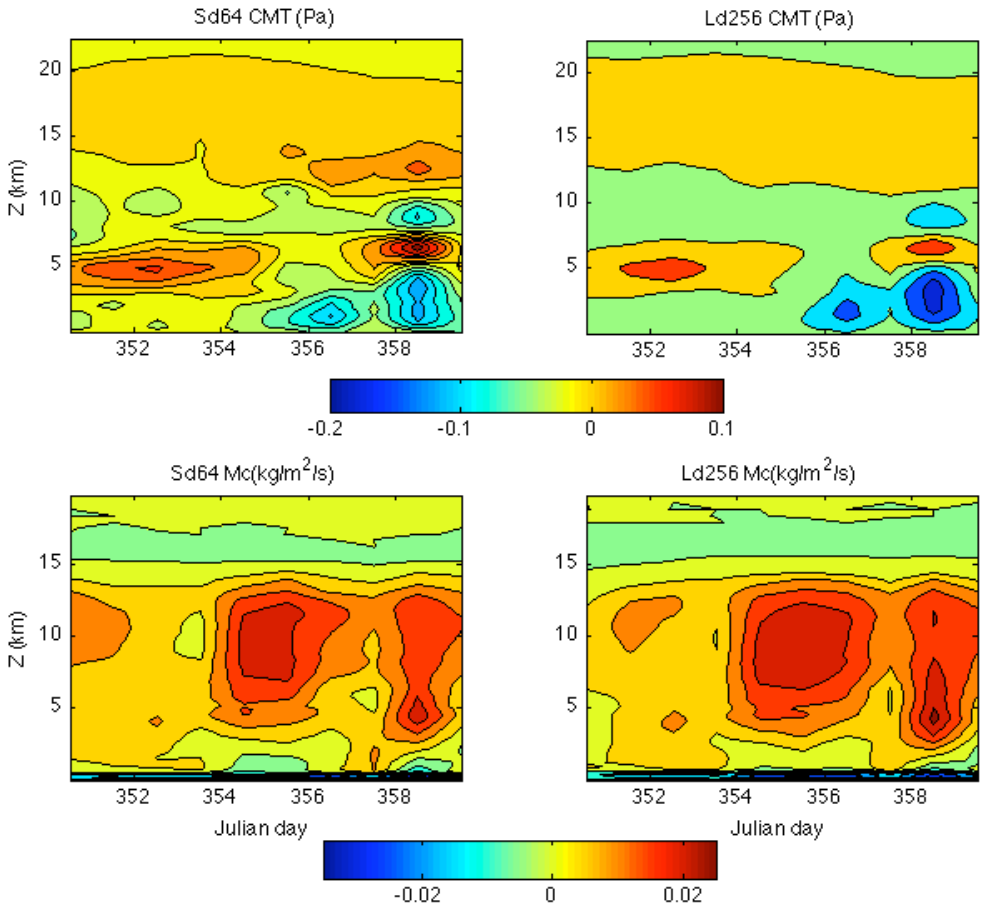

Figure 3.2.3. Contour plots of time-height section of CMT (Pa) for the small domain (top row left) and for the larger domain (top row right), and of total cloud mass flux Mc (kg/m²/s) given by D64T120-S (bottom row left) and by D256T10-S (bottom row right), for the time interval Jd 350:359.

Chapter 4

Mass-Flux Discretization of Convective Momentum Transport

This chapter discusses the skill of the mass-flux representation of CMT first proposed by Schneider and Lindzen (1976, hereafter SL76). It investigates the relative contributions to CMT from cumulus clouds, in the form of saturated updrafts and downdrafts, and from unsaturated air in the form of downdrafts and vertically propagating gravity waves.

4.1 Testing the SL76 scheme

Schneider and Lindzen (1976) noted the failure of eddy-diffusion theory to correctly identify regions where the momentum transport is upgradient, since the theory only predicts downgradient momentum transports (of opposite sign to the vertical shear) at all levels. They instead proposed a linear relationship in which the vertical transport of horizontal momentum relates to the upward cloud mass flux M_c and to the difference between the mean horizontal wind ($\bar{U}$) and the horizontal wind within the cloud (u_c):

$$-\overline{\rho}\left(\overline{u'w'}\right)_c = M_c\left(\overline{U} - u_c\right) \tag{4.1}$$

This expression is derived by assuming that the fractional area of transporting clouds is much less than unity, and that the momentum transport is due to upward motion with cloud mass flux M_c and horizontal velocity u_c and a compensating downward cloud mass flux ($-M_c$) in the environment where the horizontal velocity is assumed to be $\bar{U}$. This type of representation is called a mass-flux parameterization of CMT. SL76 further assumed that u_c at all heights within the cloud is equal to the environmental wind at the cloud base (updrafts conserve their horizontal momentum). More recent mass-flux parameterizations of CMT modify the vertical profile of u_c to contributions from entrainment and pressure drag, as we will later discuss.

In environments where the vertical wind shear does not change too rapidly with height (often a good assumption in TOGA COARE), the difference ($\bar{U}$ - u_c) tends to be proportional to the mean vertical wind shear, with a proportionality constant that depends on the combined effect of the perturbation pressure gradient force on saturated updrafts and the lateral entrainment rate into these same updrafts, both of which tend to bring u_c closer to $\bar{U}$. Therefore, the equation (4.1) may be written as:

$$-\bar{\rho}\,\overline{\left(u'w'\right)}_c = L\,M_c\,\frac{\partial \bar{U}}{\partial Z} \tag{4.2}$$

where L represents the vertical mixing length scale (in meters) for updraft zonal velocity perturbations associated with entrainment and horizontal pressure gradient accelerations. In this case, the mass-flux approach reduces to downgradient momentum transport with eddy viscosity K = M_c L. SL76's scheme is like assuming the mixing-length at each height to equal the height above the cumulus cloud base. For most other more modern CMT schemes, L is comparable to an inverse lateral entrainment rate.

To investigate at what altitudes CRM-simulated cumulus convection is acting like an effective eddy viscosity, equation (4.2) is used as the basis of a linear regression, where the predictor is the product between the updrafts cloud mass flux and the vertical wind shear (hereafter referred as *X1*), the convective momentum transport is the predictand (hereafter referred as *X2*) and L is treated as an unknown to be estimated from the CRM output as the slope of the linear regression. Two regions are excluded from these calculations: the stratosphere (in which there are no cumuli and hence no CMT), and the subcloud boundary layer between the surface and the 500 m of height because in this layer the vertical momentum transport is due to the effect of turbulent eddies rather than cumulus clouds. The troposphere is divided into three layers: the lower troposphere (between 500m and 3 km of height), the middle troposphere (between 3 and 7 km of height) and finally the upper troposphere (from 7 to 16.7 km of height). The top of the

upper tropospheric layer is defined by the minimum value of the mean absolute temperature, which defines the transition between the troposphere and the stratosphere. The time period analyzed is the 10-day period from Julian days 350 to 359, corresponding to December 16th to 25th, 1992, for which there are both small and large-domain simulations.

We anticipate that ($\bar{U}$ - u_c) may be proportional to a vertically smoothed vertical wind shear due to the fact that the updraft cannot respond instantaneously to the vertical gradients of environmental wind, because it must be accelerated by entrainment and lateral pressure forces. Hence, four different smoothing scales ∂z for the vertical wind shear are tested: the actual model vertical resolution named the "CRM ∂z", ∂z = 1 km, ∂z = 1.5 km and ∂z = 3 km. In each case, the smoothed shear is computed using a forward finite difference scheme between all model flux levels within the height range considered. The model output used is from the runs D64T120-S and D256T10-S (please refer to Table 2.1 for more detailed information).

The hourly evolution for both the predictor (*X1*) and the predictand (*X2*) quantities, within the previously designated tropospheric layers, for all four choices of smoothing scale ∂z is investigated in order to extract some information about the variability of these fields. Figure 4.1.1 shows the hourly time series for the model regular vertical grid spacing. The predictand *X2* (CMT) presents the greatest variability over the 10-day period of simulation, within the lower and middle troposphere; the upper layer does not show much CMT, comparing with the other two tropospheric layers. The lower troposphere does not exhibit significant variability of CMT (*X2*) in the first half of the time period; the second half is characterized by a different structure with a couple of negative peaks. These responses are seen within the middle and upper layers where the vertical gradient of environmental wind is stronger and the cloud updrafts are well established. The predictor (*X1*) shows significant variations within the lower and middle troposphere, with smoother variations in the upper troposphere. In the lower layer, the first half of the 10-day period shows almost no variations, and the second half shows positive and negative peaks; similar structure is found in the mid troposphere. The vertical profile of updraft cloud mass flux McUP (Fig. 3.1.12) averaged over this period of time exhibits two maxima within these two layers, and its vertical variation suggests a significant entrainment signature in these tropospheric regions; the vertical wind shear also varies significantly within these layers, explaining the predictor perturbations seen below 7 km of height. Above this height, McUP decreases almost monotonically, influencing most the temporal structure within the upper tropospheric layer. For the whole troposphere, both *X1* and *X2* exhibit stronger variability in the second half of the 10-day period when strong convective precipitation, associated with this deep convective episode, is registered.

The small and large spatial domain simulations, for all tropospheric layers and ∂z considered, produce similar values of *X1* and *X2* over the whole period. This similarity is somewhat kept when daily time series are computed. Daily averaging leads to a much smoother temporal behavior, removing the noise from both *X1* and *X2*, as can be seen in Figure 4.1.2.

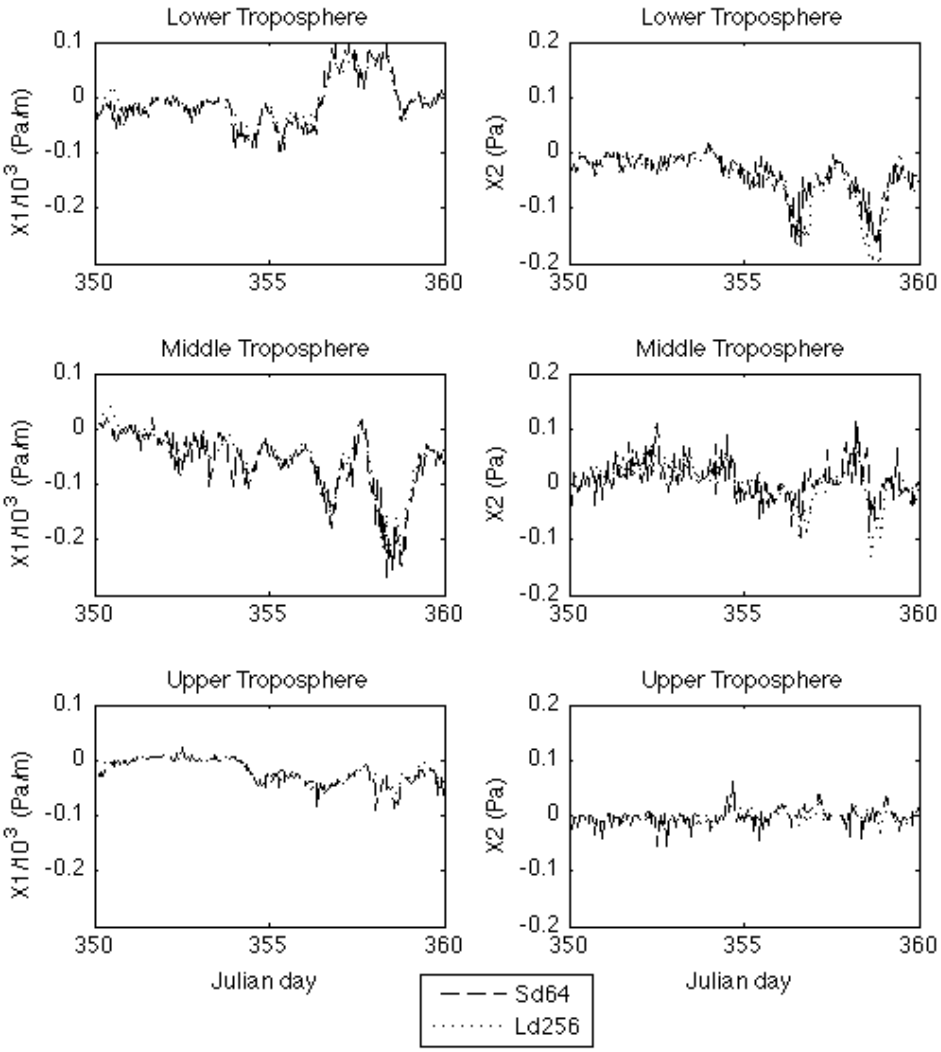

Figure 4.1.1. Hourly time series of *X1* (*Mcup*∂Ū/∂z*, left column) and *X2* (*CMT*, right column), for 10-day common period of simulation, within the lower, middle and upper troposphere, given by D64T120-S (dashed line) and D256T10-S (dotted line) data sets using the regular model vertical grid spacing ∂z.

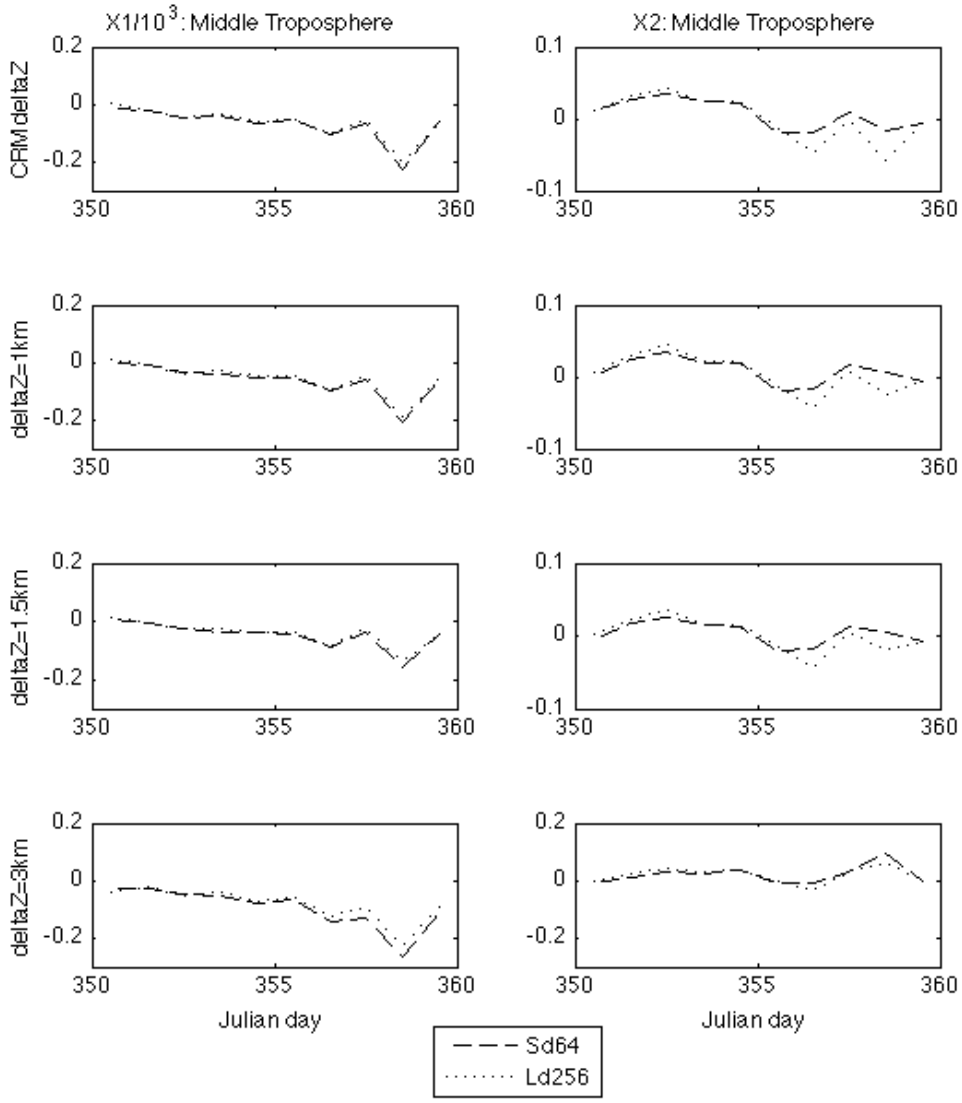

Figure 4.1.2. Daily time series of *X1* (*Mcup*∂Ū/∂z [Pa/m]*, left column) and *X2* (*CMT [Pa]*, right column), for 10-days common period of simulation, within the middle troposphere, for different choices of *∂z,* given by D64T120-S (dashed line) and D256T10-S (dotted line).

We note that *X1* and *X2* are one order of magnitude smaller in the upper troposphere (i.e. there is much less CMT) than in the rest of the troposphere. The most prominent features exhibited by *X1* and *X2* in each layer during the 10-day simulations are reproduced for all four choices of smoothing depth *∂z*, with some slight variations in their magnitudes visible in the hourly and daily time series. This suggests that changing the

vertical grid spacing within the troposphere (planetary boundary layer and stratosphere excluded) does not mask the important variations of both *X1* and *X2* throughout time.

The linear regression applied to equation (4.2) reveals the skill of a downgradient diffusion scheme, indicating how CMT (*X2*) is related to the product of vertical wind shear by the updraft cloud mass flux (*X1*), the goodness of the linear fit and what is a good estimate for the vertical mixing length at which CMT is carried out by the predictor, considering specific vertical grid scales. The linear regression results for the lower, middle and upper troposphere are represented in Figures 4.1.3, 4.1.4 and 4.1.5, and Table 4.1 gives the slope and (in parentheses) the correlation coefficients.

∂z	Spatial Domain	Lower Troposphere	Middle Troposphere	Upper Troposphere
CRM	D64	214 (0.38)	- 11 (0.03)	146 (0.44)
	D256	169 (0.21)	- 131 (0.22)	137 (0.36)
1 km	D64	267 (0.56)	91 (0.25)	249 (0.67)
	D256	244 (0.35)	-10 (-0.02)	249 (0.60)
1.5 km	D64	461 (0.82)	187 (0.53)	297 (0.68)
	D256	745 (0.85)	102 (0.23)	306 (0.62)
3 km	D64	649 (0.98)	290 (0.66)	426 (0.80)
	D256	1480 (0.91)	114 (0.25)	439 (0.73)

Table 4.1. Slope values *L* (in meters) and correlation coefficients (in parentheses) for all tropospheric layers and all ∂z studied, as the result of applying a linear regression to the equation (4.2), for the two spatial domain data sets, D64T120-S and D256T10-S.

The lower troposphere (Fig. 4.1.3) reveals low correlation coefficients for the first two ∂z tested, implying that the predictor is not the CMT main driving force at these levels for those vertical scales, and suggesting that CMT is carried out by the subgrid turbulence scheme, since McUP doesn't have a significant signature at these levels. For ∂z = 1.5 and 3 km, the linear fit improves considerably, with a much less spread of values, greater than 80% for both spatial domain data sets. These results indicate that the predictor is doing a good job in predicting CMT, that is, a good simulation of *X1* results in a more reliable CMT field within this region. The slope given by the linear regression are all positive within this layer, which means that lower troposphere is dominated by downgradient zonal momentum fluxes, for all vertical length studied.

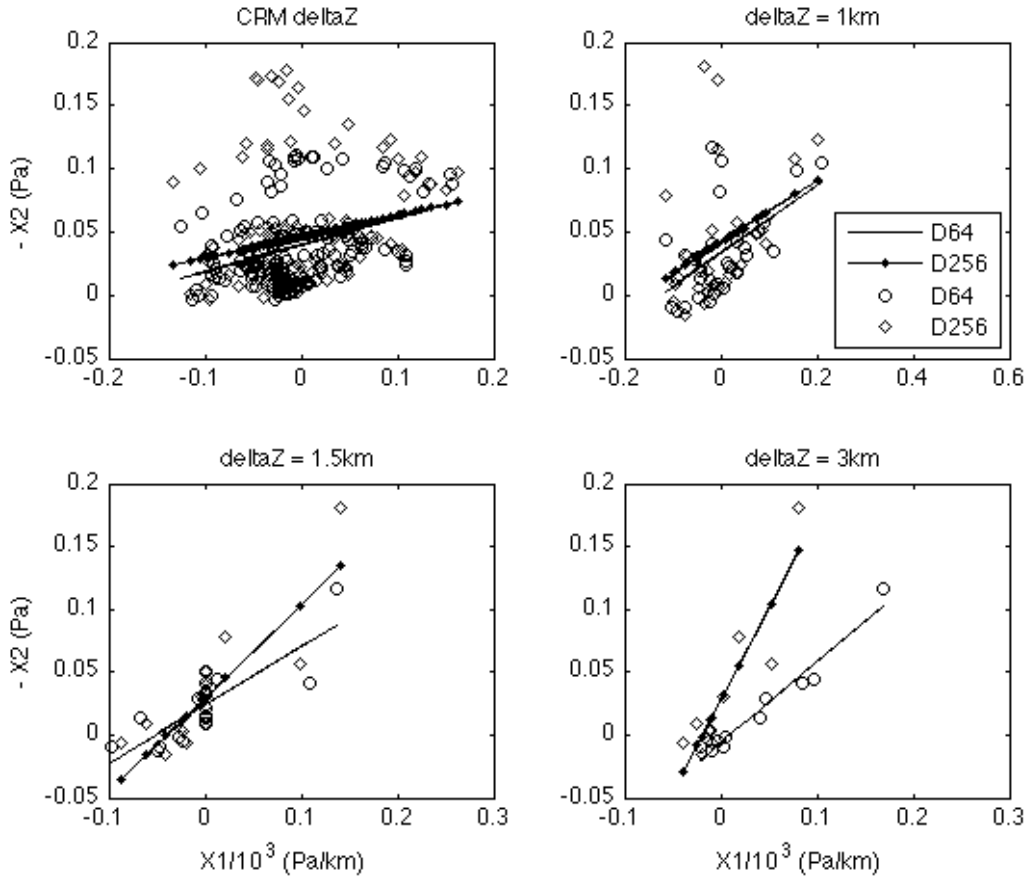

Figure 4.1.3. Scatter plots of *X1* and *-X2*, and the linear regression applied to equation (4.2), for each *∂z,* for small (circles and solid line) and large (diamonds and dotted line) domain sizes, within the lower troposphere.

The middle troposphere (Fig. 4.1.4) is the layer with the weakest linear fit. *X1* and *-X2* are only weakly correlated for all *∂z* tested, except for a stronger positive correlation for *∂z* = 1.5 and 3 km in the small-domain simulation. Within the mid-levels, the McUp field and the vertical wind shear both vary considerably during the 10-day simulation, so the lack of correlation is noteworthy. The slope values (Table 4.1) are not always positive, mainly for the small vertical scales, indicating the presence of upgradient momentum fluxes at specific heights. The failure of downgradient diffusion to reproduce the midtropospheric CMT shows that a more sophisticated mass-flux scheme is required for CMT parameterization.

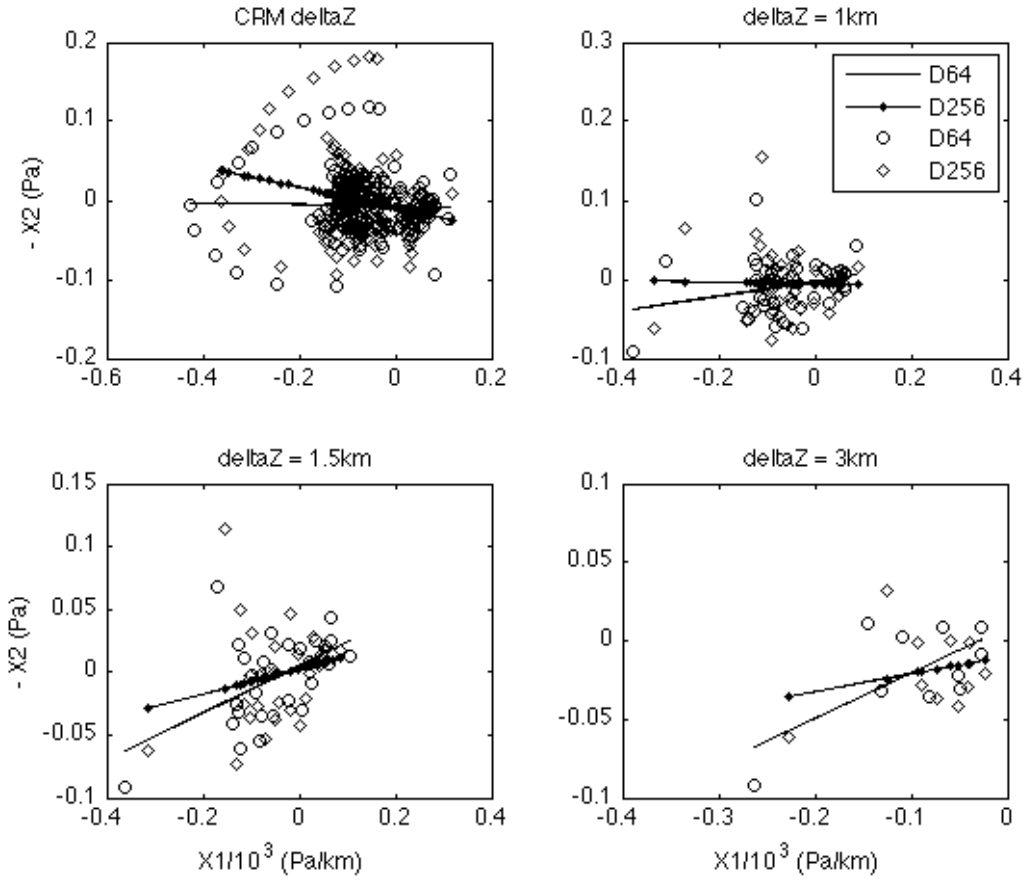

Figure 4.1.4. Scatter plots of *X1* and *-X2*, and the linear regression applied to equation (4.2), for each *∂z,* for small (circles and solid line) and large (diamonds and dotted line) domain sizes, within the middle troposphere.

Results for the upper troposphere (Fig. 4.1.5) exhibits very close similarity between both spatial domains, and correlation coefficients are very close to each other for *∂z* of 1 km or larger. The vertical scales of 1.5 and 3 km are the ones presenting the best linear fit between *X1* and *-X2,* as in the lower troposphere, although the correlation coefficients values are slightly smaller. The implied mixing-length scale is 250-450 m depending on *∂z*. This is much smaller than the prediction of SL76 (which would be around 10 km), showing that the horizontal momentum in the updraft is greatly modified by entrainment and pressure gradient forces as it rises from cloud base. Reflecting upon the values displayed in Table 4.1 having in mind the regions of strongest correlation, a vertical grid resolution of 1 or 1.5 km (3 km would be a somewhat coarse resolution) might be the appropriate choice for validating SL76 scheme, reducing the signature of turbulent (sub-grid scale) fluxes in the resolved CMT. The 3D-CRM vertical mixing-length scales are in

agreement with those used by Kershaw and Gregory (1997) in their study.

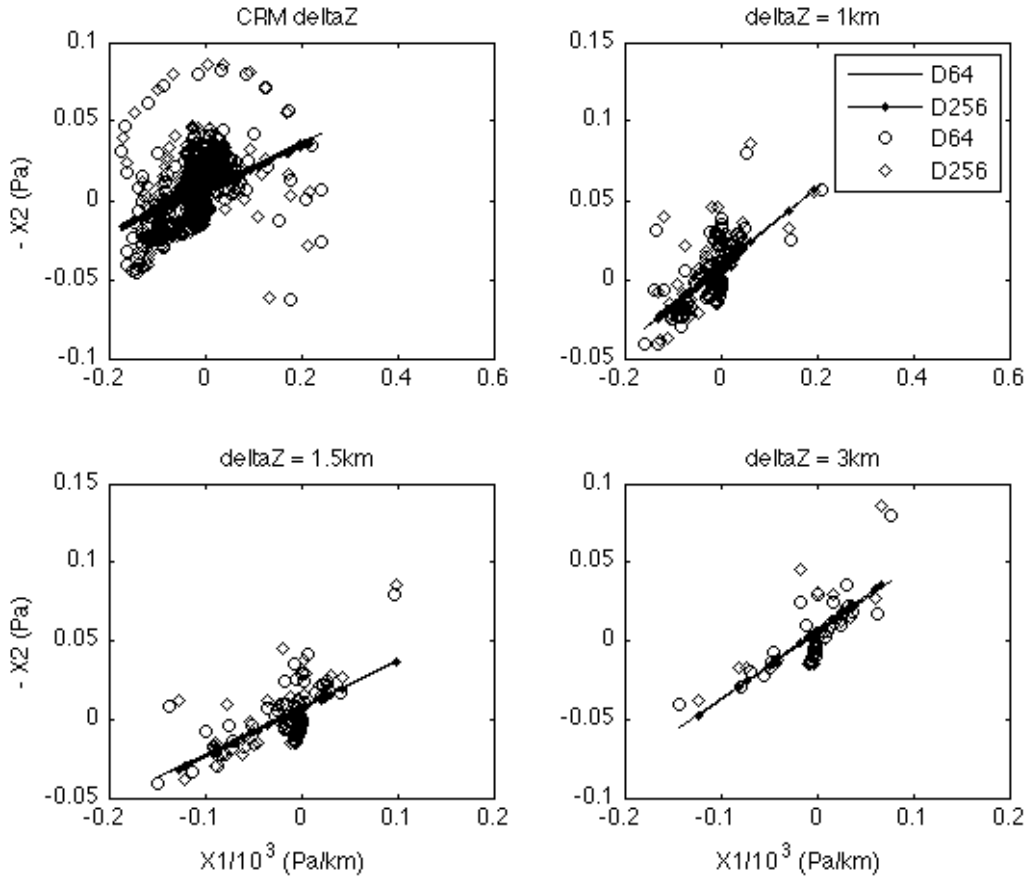

Figure 4.1.5. Scatter plots of *X1* and *-X2*, and the linear regression applied to equation (4.2), for each *∂z,* for small (circles and solid line) and large (diamonds and dotted line) domain sizes, within the upper troposphere.

This analysis was also performed using the complete D64T120-S only, for the whole 120-day period. Similar results were achieved; the best linear fit was observed for *∂z* = 1.5 and 3 km, and the spread of values decreased substantially at these *∂z* values. For mid-troposphere, the linear fit was very weak at all *∂z* considered, indicating a poor relationship between the fields. The upper troposphere still continue to exhibit a good correlation between the fields; a linear relationship was verified for all *∂z*, and the slope values were very close to each other.

4.2. The relative CMT contributions from saturated and unsaturated air

To analyze cumulus convection, it is useful to separate the contributions to vertical transports from saturated air (air within the clouds) and unsaturated air (air outside or between clouds, or free air) because these can have different underlying mechanisms. The core assumption made in all CMT parameterizations is that CMT mainly occurs within vigorous cumulus cloud updrafts and downdrafts, i.e., CMT is dominated by large horizontal velocity anomalies in the cumuli. Unsaturated updrafts and downdrafts are neglected. Furthermore, it is usually assumed that cloud updrafts have a much stronger contribution to CMT than saturated downdrafts. Our 3D-CRM simulations allow us to test these simplifying assumptions.

The first step of this analysis is the definition of saturated and unsaturated updrafts and downdrafts. Following GKI97, a model grid point is defined to be part of a saturated or unsaturated updraft, strong updraft, and downdraft when the conditions for QN and W given in Table 4.2 are simultaneously satisfied. Our analysis will focus on CMT during the strong convection episode on Julian day 358 (December 24th, 1992). This method uses the D64T10 data set, encompassing eight 3-dimensional CRM volumes per Julian day.

	QN (g/kg)	W (m/s)	
Saturated	> 0,001	≥ 1	Updraft
Unsaturated	0		
Saturated	> 0,001	≥ 5	Strong Updraft
Unsaturated	0		
Saturated	> 0,001	≤ -1	Downdraft
Unsaturated	0		

Table 4.2. Definition of a saturated and unsaturated updraft model grid point, a saturated and unsaturated strong updraft model grid point, and a saturated and unsaturated downdraft model grid point, using its non-precipitating condensate (water plus ice) mixing ratio QN (g/kg) and its vertical velocity W (m/s) as defining characteristics.

A simple observation of the CMT vertical profiles generated by the different contributions of saturated and unsaturated air reveals some important results. It is

important to mention that the sum of the saturated and unsaturated portions of the spatial domains equals the whole CRM spatial domain, therefore the 'CRM' CMT averaged over the whole spatial domain is the sum of the CMT generated by the saturated air (in all its forms) and by the unsaturated air (in all its forms). In the left plot of Figure 4.2.1 are the CMT vertical profiles contributed by different types of saturated air, averaged over the eight sampling times. The SAT curve is the CMT contributed by all saturated grid points; the SUP vertical profile defines the CMT contributed by all saturated updrafts grid points; the SSUP refers to the CMT contributed by all strong saturated updrafts; and finally, the SDN profile corresponds to the CMT contributed by the saturated downdraft grid points.

While we might expect the CMT to be dominated by the contribution of saturated updrafts and downdrafts, this is not true in the lower troposphere. There is a CMT peak below 5 km of height which reflects similar magnitude contributions from saturated and unsaturated motions. The saturated contribution comes mainly from updrafts, and about half this contribution comes from strong updrafts. Above 5 km, there is a CMT maximum that again follows the SAT CMT profile, but now the contribution from the saturated updrafts is partly cancelled by the saturated downdrafts. Near 9 km and 13 km respectively, there is a CMT minimum and maximum, each dominated by the saturated contribution. Once more, the saturated downdrafts partly cancel a much larger contribution from saturated updrafts. Above 16 km of height, above the cumulus cloud layer, the CRM CMT is dominated by unsaturated air.

In the right plot of Fig. 4.2.1, the UNSAT profile refers to the CMT generated by all unsaturated grid points, the UNSUP curve corresponds to the CMT carried out by all unsaturated updrafts grid points, the UNSSUP structure defines the CMT obtained by selecting the strong unsaturated updraft grid points, and finally the UNSDN regarding the CMT generated by all unsaturated downdrafts, averaged over these grid points and over the 8 time steps. Throughout the troposphere, the overall CMT (solid line) is of greater magnitude than the unsaturated contribution to CMT. The contribution from the unsaturated strong updrafts is negligible, and the unsaturated updraft CMT is weak and localized within 7 and 15 km of height, presenting a very different vertical structure compared with CRM CMT and having a signature on the CMT carried out by the unsaturated air as a whole (UNSAT curve). The UNSAT CMT owes most of its vertical structure to unsaturated downdrafts which are most significant below 7 km. Above 16 km, there are no clouds so all CMT is unsaturated.

The CMT contributions from saturated and unsaturated air have different vertical profiles, and the unsaturated air significantly shapes the CMT profile within the lower levels and above the tropopause. These preliminary results imply that CMT parameterizations need to consider the contribution from unsaturated air.

To better understand the physical processes underlying the relative CMT contributions from cumulus clouds, in the form of saturated up- and downdrafts, and from unsaturated air, in a combination of convective downdrafts and vertically propagating gravity waves, a vertical-velocity binning approach is applied to the 3D small domain hourly data set for Julian day 358, but first tested on a single 3D CRM volume. The binning method shows in more detail the contributions to CMT from drafts of different strengths. A binning method (as opposed to scatterplots, for example) is very helpful because the spatial correlations of horizontal and vertical velocity perturbations that create CMT are relatively weak, 0.1 or less at many vertical levels, and binning filters out most of the noise, isolating the correlated part of the variability without assuming a particular (*e.g.* linear) structure for this variability, thereby providing clarification of the mechanisms involved in the CMT. The greatest advantage of this method is that one can look at the subsets of the chosen bins, for instance strong w', weak w', or $w' > 0$, and see the patterns that may not show up clearly in the overall relationship between the variables in study.

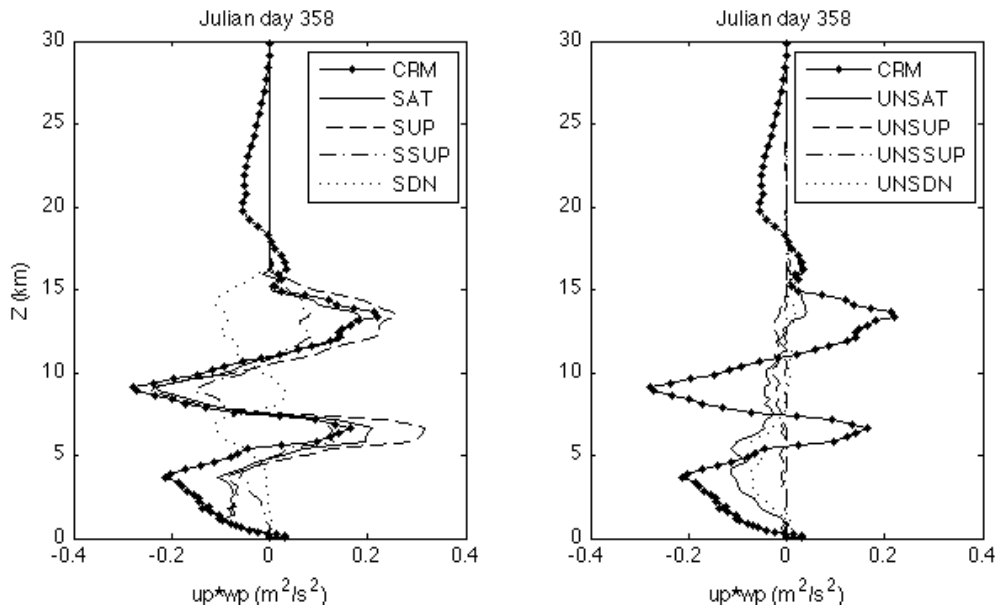

Figure 4.2.1. Vertical profiles of the CMT (the product of the zonal wind perturbation (*Up*) by the vertical wind perturbation (*Wp*)) averaged over the eight 3D volumes from the small-domain simulation of Julian day 358, for the whole CRM spatial domain (solid-dotted line, both left and right plots), for the saturated (solid line, left plot) and unsaturated (solid line, right plot) domains, over the saturated and unsaturated updrafts (dashed line, left and right plots, respectively), over the strong saturated and unsaturated updrafts (dashed-two dots line, left and right plots, respectively) and over the the saturated and unsaturated downdrafts (dotted line, left and right plots, respectively).

After optionally separating saturated and unsaturated air at each level, grid points are binned by vertical velocity w. The bin size (the number of grid points combined in each bin) must be chosen large enough to isolate the desired CMT signal, yet small enough not to average drafts with significantly different vertical velocities. Four bin sizes are tested, composed of 512, 256, 128 and 64 elements. For each w-bin, the bin-mean zonal momentum perturbation u' is computed. By averaging across the bins, the saturated CMT is estimated. If this compares well to the exact saturated CMT simulated by the model, little information relevant for CMT has been lost by binning. The unsaturated air is treated similarly.

Figure 4.2.2 shows that the binned CMT vertical profiles obtained using all four bin sizes match the full CMT almost perfectly. Figures 4.2.3 and 4.2.4 show this is also true for the saturated and unsaturated CMT separately. This indicate that this approach does not loose information about the overall structure of the CMT for any of the chosen bin sizes.

Each vertical level is analyzed individually, and the correlation coefficients between the bin-averaged u' and w' are retrieved as well as the coefficient of determination (R2) which is the correlation coefficient squared, focusing on the vertical levels where the coefficients are stronger (in absolute value) and in the levels in which the CRM CMT and the CRM CMT carried out by saturated and unsaturated air peak or have a significant signature. The P-value statistical test is applied to each level in order to extract information whether is relationship between the fields is statistically significant or not. For this test we consider 95% and 99% confidence levels. The vertical profiles of the unbinned correlation coefficient values between u' and w' correlations range from 0 to 20% (in absolute value) throughout most of the troposphere. Because of the large sample size (the 256x256 grid points at each level), even such small correlations can be statistically significant. However, this behavior suggests that the relationship between u' and w' can be more clearly seen using binning, which averaged across some of the noise in their relationship. Close to the stratosphere, this correlation becomes larger, around 60%.

Binning u' and w', without partitioning into saturated and unsaturated air, exposes different relationships between the bin-averages of these atmospheric fields at different altitudes. Figure 4.2.5 shows the binned analysis at four representative altitudes for all considered bin sizes. Below 5 km (Z23 in Fig. 4.2.5), such that negative zonal wind perturbations are associated with updrafts and positive zonal wind perturbations tend to be downdraft-related to yield a strong linear anticorrelation and a downward CMT. At higher altitudes, a C-shape relationship between binned u' and w' is seen in most plots present in Fig. 4.2.5, in which both strong updrafts and strong downdrafts have similar u', while bins with near-zero w' have u' of the opposite sign and much smaller magnitude. This is true for the vertical levels with maximum positive values of CMT (Z35 at 6.625 km

and Z62 at 13.375 km) and at vertical levels with strong negative values of CMT (Z23 at 3.625 km and Z45 at 9.125 km). A bin size of 256 seems to be enough to remove most of the noise and still resolves this C-shape relationship well, so we use this bin size for our remaining analysis.

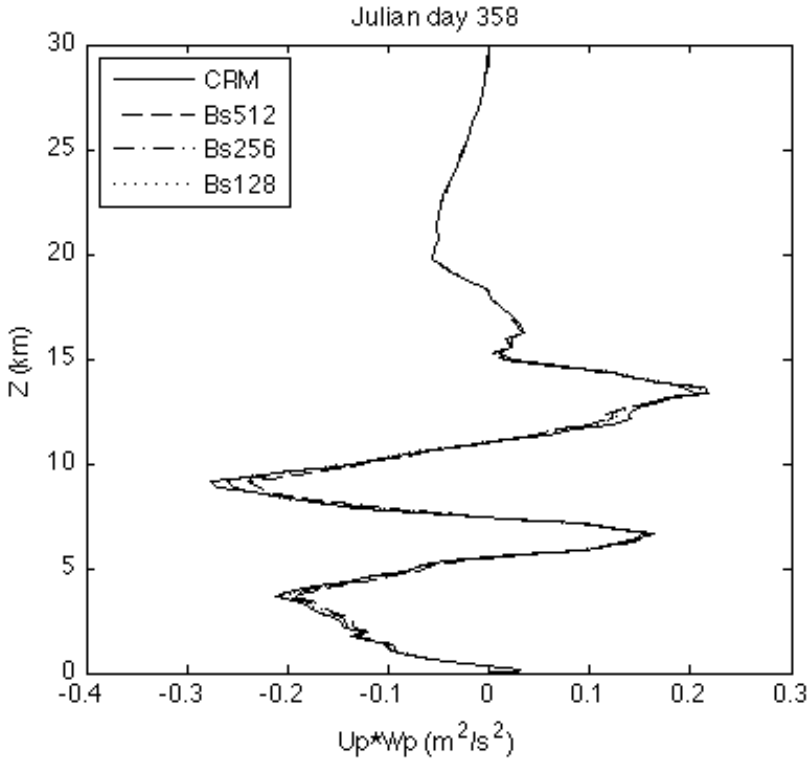

Figure 4.2.2. Vertical profile of unbinned CRM CMT (solid line) overlaid by the binned CMT vertical profiles obtained by the bin sizes of 512 (dashed line), 256 (dashed-dotted line) and 128 (dotted line) elements, for Julian day 358.

We next apply the binning approach separately to the saturated and unsaturated *u'* and *w'*. The vertical distribution of correlation coefficients between binned saturated and unsaturated *u'* and *w'* show some contrasting structures , especially in mid and upper levels. From the surface up to 5 km, the correlation between binned fields is strongly negative for saturated air and less strongly negative for unsaturated air, as can be observed for level Z23 (3.625 km) in Fig. 4.2.6. These levels feature mostly linear relationships between binned saturated and unsaturated *u'* and *w'*. Similar correlation coefficients values are registered between 8 and 10 km of height for unsaturated air. Above 5 km and below 8 km of height (*e.g.* Z30), a C-curve with little linear correlation is observed for saturated air; the unsaturated binned *u'* and *w'* also start to show a C-curve; their linear correlation weakens but continues to be negative. The C-curve structure

persists throughout the mid to upper troposphere in both saturated and unsaturated air. Above convection, the unsaturated binned variables are strongly positively correlated between 15 and 18 km, in the tropopause region, changing to very strong negative correlations within the overlying stratosphere.

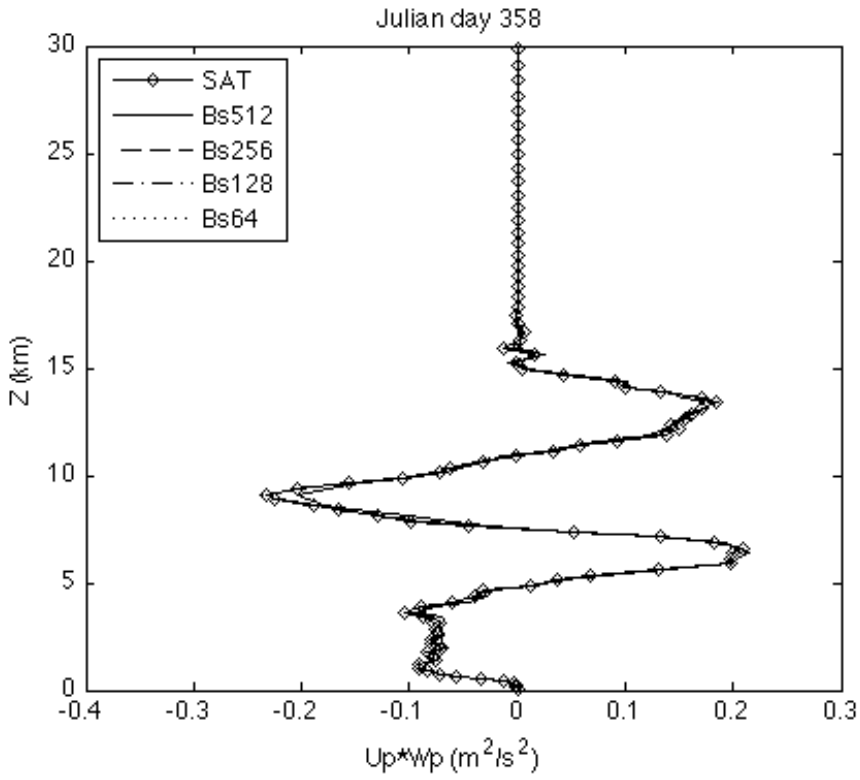

Figure 4.2.3. Vertical profiles of the product of u' by w', averaged over the saturated grid points (SAT), averaged over different number of bins examined for the saturated partition: 64 (Bs512, solid line), 128 (Bs256, dashed line), 256 (Bs128, dash-dot line) and 512 (Bs64, dotted line).

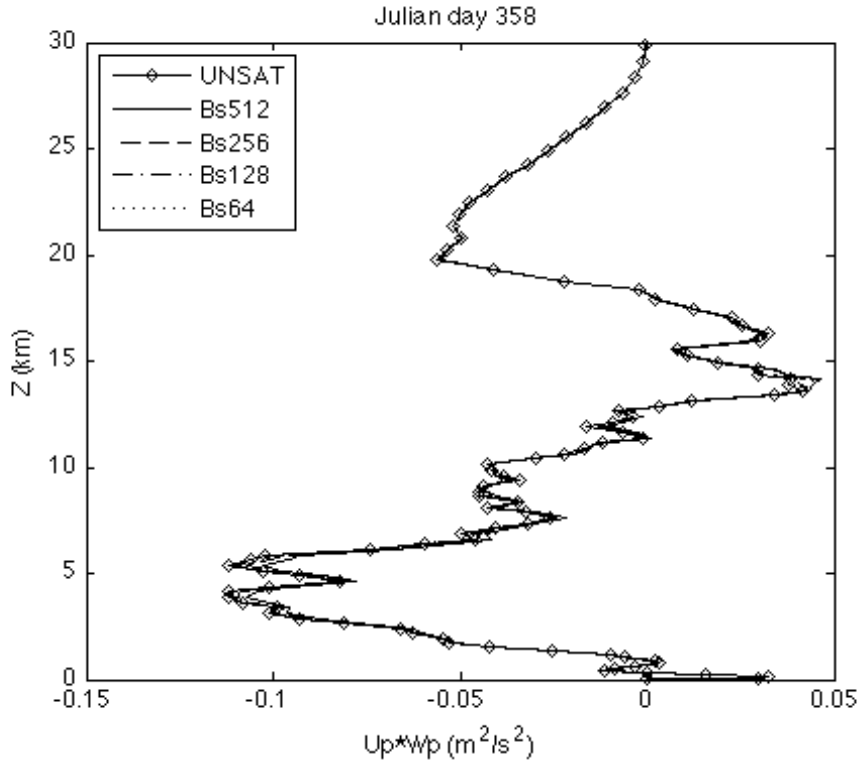

Figure 4.2.4. Vertical profiles of the product of u' by w', averaged over the unsaturated grid points (UNSAT), averaged over different number of bins examined for the unsaturated partition: 64 (Bs512, solid line), 128 (Bs256, dashed line), 256 (Bs128, dash-dot line) and 512 (Bs64, dotted line).

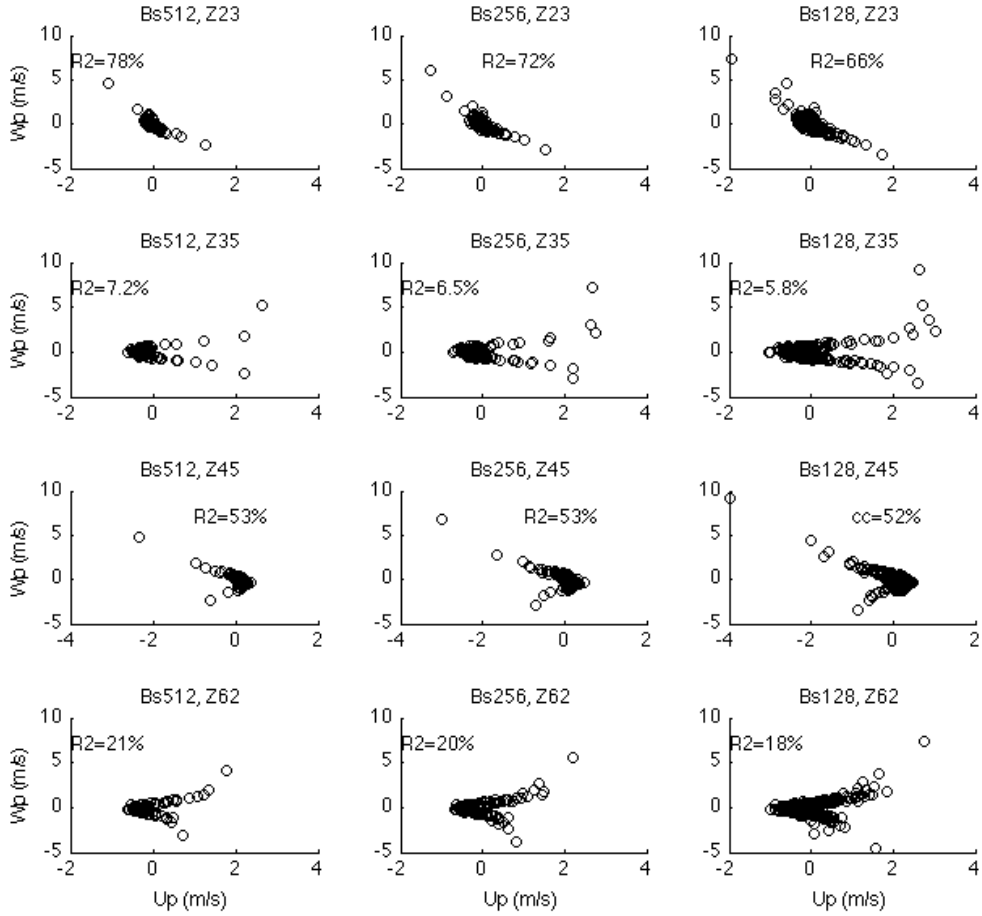

Figure 4.2.5. Scatter plots of binned u' and w', for specific bin sizes of 512 (left column), 256 (mid-column) and 128 (right column) elements, at specific vertical levels of Z23 (3.625 km, top row), Z35 (6.625 km, second row), Z45 (9.125 km, third row) and Z62 (13.375 km, last row), with the correspondent coefficient of determination values (in %), given by D64T10 data set for eight 3D volumes of Julian day 358.

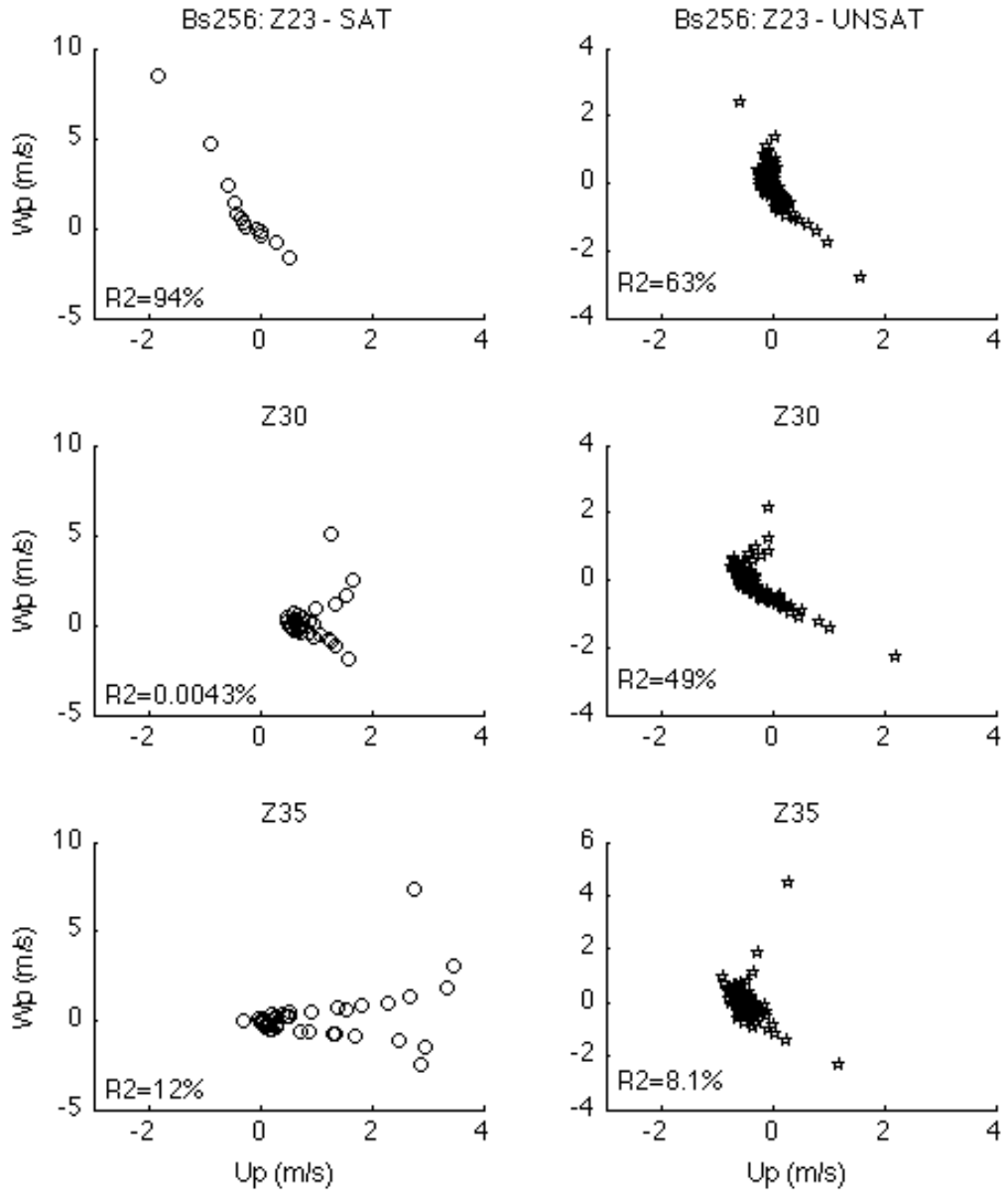

Figure 4.2.6. Scatter plots of binned saturated (left column) and unsaturated (right column) u' and w', for the bin size of 256 elements, at specific vertical levels of Z23 (3.625 km, top row), Z30 (5.375 km, second row) and Z35 (6.625 km, third row), with the correspondent coefficient of determination values (in %), given by D64T10 data set for eight 3D volumes of Julian day 358.

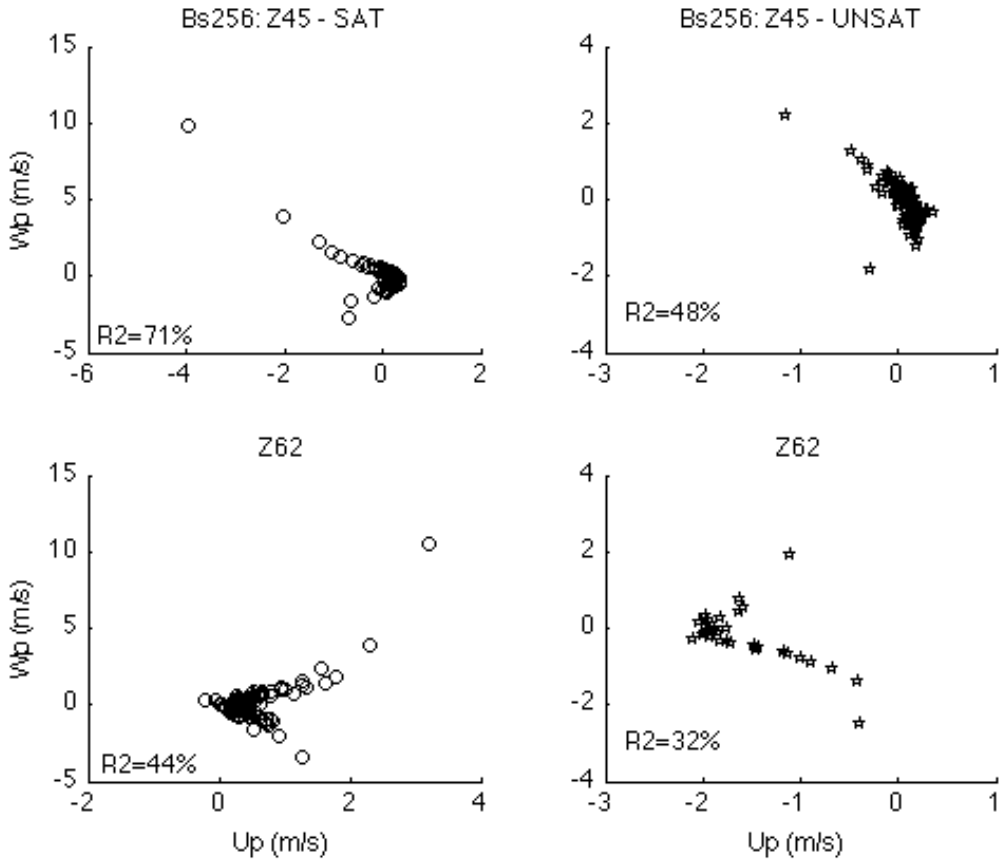

Figure 4.2.7. *(continuation of Fig. 4.2.6)* Scatter plots of binned saturated (left column) and unsaturated (right column) u' and w', for the bin size of 256 elements, at specific vertical levels of Z45 (9.125 km, first row), and Z62 (13.375 km, second row) with the correspondent coefficient of determination values (in %), given by D64T10 data set for eight 3D volumes of Julian day 358.

The C-curve shape is not documented in TOGA-COARE literature, either for saturated and unsaturated drafts, and it deserves some reflection. It remains for further analysis whether this particular characteristic is unique for this particular deep convective event. The C-shape structure dominates most of the mid and upper levels of the troposphere. It indicates that updrafts and downdrafts, both saturated and unsaturated, have momentum perturbations of the same sign, giving canceling contributions to CMT at the same height. This structure could arise if we think of each cumulus cloud and the air right next to it as a mixture of saturated and unsaturated updrafts and downdrafts, which interact through pressure gradient forces avoid colliding by all having the same horizontal velocity at each height in each cloud. More vigorous clouds develop both stronger updrafts and downdrafts and also have a stronger horizontal velocity perturbation across the entire

cloud. This idea still needs to be better tested, but highlights the complex nature of CMT, because updrafts and downdrafts are exchanging momentum with each other within the cloud, not just with the environment. This is different than the assumptions made in CMT parameterizations.

4.3. Is the unsaturated CMT due to upward-propagating gravity waves?

An important question for parameterization is whether CMT driven by unsaturated air is mainly (i) due to activity of internal gravity waves which vertically flux momentum in the stably stratified air between clouds, (ii) due to the interaction between the environmental air and cloudy air around the cloud edges, or (iii) simply due to downdrafts in clear air further from vigorous cumulus clouds.

Internal gravity waves generated in the troposphere through various processes, such as the interaction between convection and vertical wind shear, can play a vital role in the transfer of mean horizontal momentum from one layer to another layer of the atmosphere (Prabhakaran Nayar and Sreeletha, 2003), and especially in carrying momentum fluxes from the troposphere into the stratosphere. In order to test if internal gravity waves are responsible for a significant fraction of the unsaturated CMT in this tropical deep convective event, the buoyancy field is computed and w-binned. Internal gravity waves transport momentum upwards, but not buoyancy; therefore one might expect no correlation between the binned fields of vertical velocity perturbation and buoyancy. However, for buoyancy-driven updrafts and downdrafts in cumulus clouds and in the unsaturated air around their edges, one might expect a strong positive correlation between these two fields.

The buoyancy acceleration (m/s^2) B is given by the formula:

$$B = g\,\frac{T_d - \overline{T_d}}{\overline{T_d}} \tag{4.3}$$

where g is the gravitational acceleration (9.81 m/s^2) and T_d is the density temperature obtained using the expression:

$$T_d = T - \overline{T}\left(0.61 - q_v - q_n - q_p\right) \tag{4.4}$$

T is the absolute temperature in Kelvin, q_v is the water vapor mixing ratio (kg/kg), q_n is the non-precipitating condensate (water plus ice) mixing ratio (kg/kg) and q_p is precipitating water (rain plus snow, in kg/kg). Equation (4.3) may be written as:

$$B = g\,\frac{T_d'}{\overline{T_d}} \tag{4.5}$$

where T_d' is the deviation of the density temperature from its reference-state value.

Figures 4.3.1 and 4.3.2 shows binned buoyancy for the bin size of 256 elements, for saturated and unsaturated drafts at specific levels at which the partitioned CMT peaks, and one particular level in the stratosphere, Z83 at 21 km of height, where only unsaturated air is present. For comparison, the binned zonal velocity perturbation is also displayed in same panels. As expected for buoyancy-driven convection, the saturated drafts (inside clouds) show buoyancy acceleration strongly positive correlated to *w'* throughout most of the troposphere, contrasting with the noisy nonlinear C-shape relationship between *u'* and *w'*. Above 15 km of height, at the very top of the cumulus clouds, the sign of the correlation reverses, as one might expect for cumulus drafts that have overshot their level of neutral buoyancy so they are moving upward due to their inertia but have negative buoyancy.

For the unsaturated air, the situation is more complex and the presence of internal gravity waves isn't easy to identify. Below 15 km, buoyancy and *w'* are much more weakly correlated than *u'* and *w'*, as can be observed from Figures 4.3.1, 4.3.2 and 4.3.3, as one would expect if gravity waves were responsible for much of the CMT. Levels Z30, Z35 and Z45 are good examples of this behavior. Most of the binned *By - w'* correlations, though weak, are still statistically significant. Looking into detail to some of these weak correlations, we see that the buoyancy acceleration is almost zero for all *w'* bins except for strong updrafts.

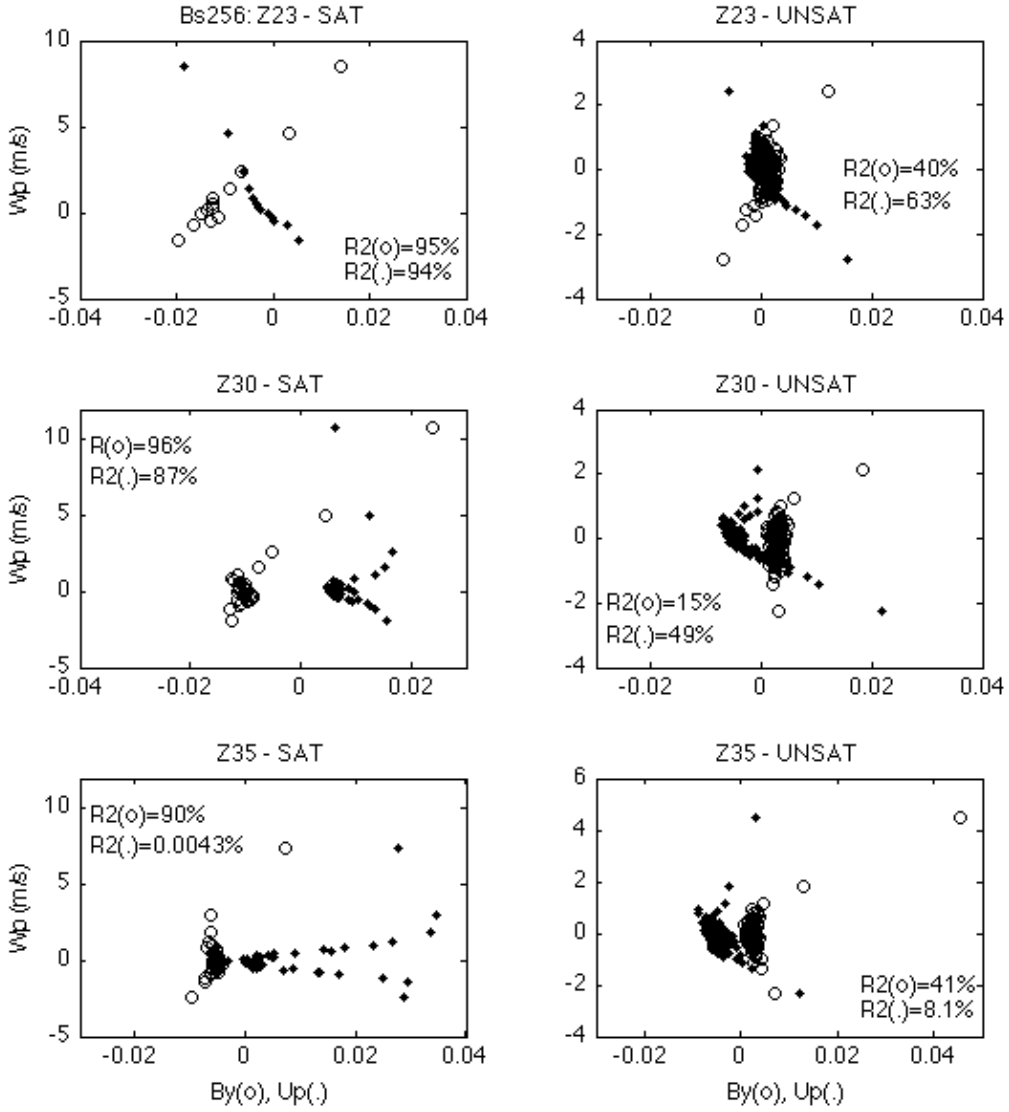

Figure 4.3.1 Scatter plots of binned saturated (left column) and unsaturated (right column) *Buoyancy* (By - circles - in m/s²), *u'* (Up - dots - in m/s/100) and *w'* (Wp in m/s), for the bin size of 256 elements, at specific vertical levels of Z23 (3.625 km, top row), Z30 (5.375 km, second row) and Z35 (6.625 km, third row), with the correspondent coefficient of determination values (in %), given by D64T10 data set for eight 3D volumes of Julian day 358.

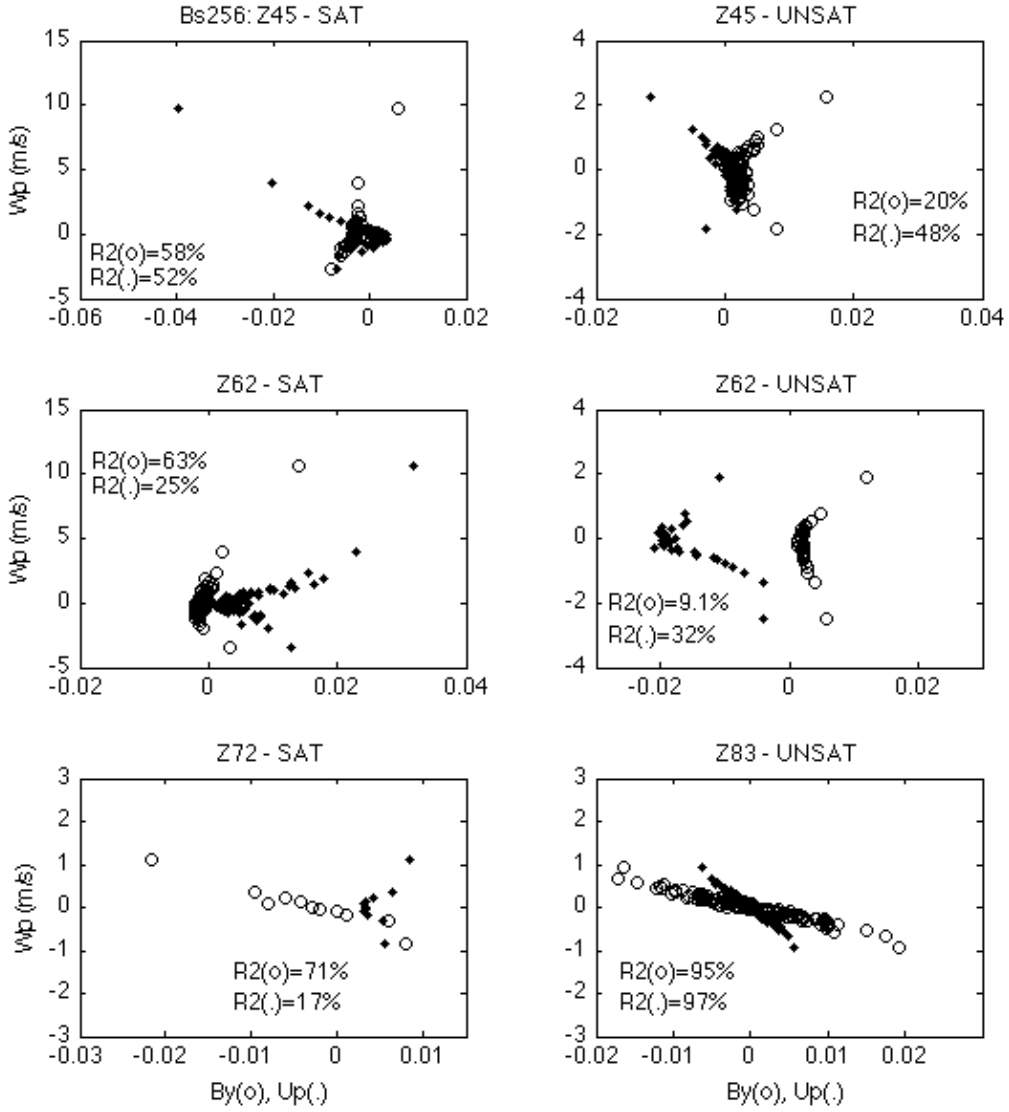

Figure 4.3.2. *(continuation of Fig. 4.3.1)* Scatter plots of binned saturated (left column) and unsaturated (right column) *Buoyancy* (By - circles - in m/s²), *u'* (Up - dots - in m/s/100) and *w'* (Wp in m/s), for the bin size of 256 elements, at specific vertical levels of Z45 (9.125 km, first row), Z62 (13.375 km, second row), Z72 (16.281 km) for saturated bins and Z83 (21 km, stratosphere) for unsaturated bins only, with the correspondent coefficient of determination values (in %), given by D64T10 data set for eight 3D volumes of Julian day 358.

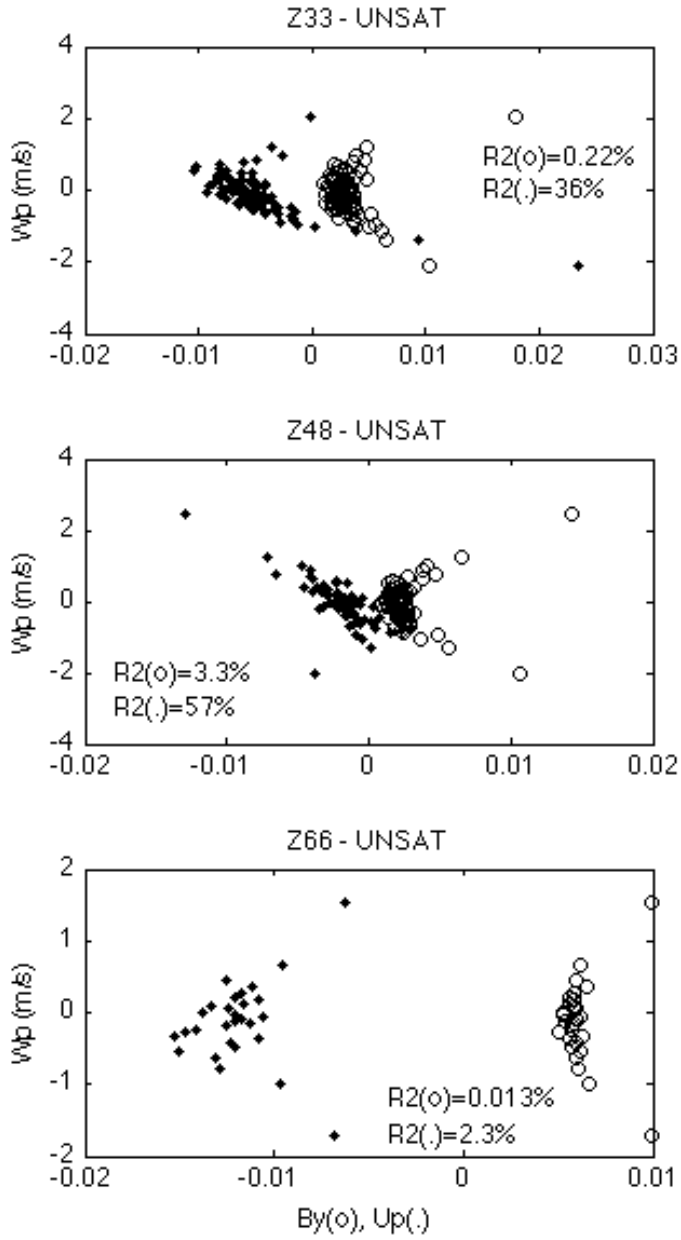

Figure 4.3.3. Scatter plots of binned unsaturated *Buoyancy* (By - circles - in m/s²), *u'* (Up - dots - in m/s/100) and *w'* (Wp in m/s), for the bin size of 256 elements, at specific vertical levels of Z33 (6.125 km, first plot), Z48 (9.875 km, second row), Z66 (14.81 km), with the correspondent coefficient of determination values (in %), given by D64T10 data set for eight 3D volumes of Julian day 358.

The unsaturated strong drafts carry some buoyancy suggesting that the interaction between environmental air and the air inside the cloud is driving these drafts, but internal gravity waves are dominating the remain w' spectrum, since it's clear that buoyancy is not the main mechanism driving the unsaturated air for most levels inside the cloud. Above 20 km of height, in the stratosphere, binned w' is weak, but is clearly anticorrelated with buoyancy as well as u'. Furthermore, the upward momentum flux become gradually less negative with height (Fig. 4.3.2). This is consistent with momentum transport by an upward-propagating gravity wave that is slightly damped, for instance by numerical diffusion in the CRM. Kuang and Bretherton (2004) found such gravity wave damping is due to our use of a vertical grid spacing that is too large (roughly 500 m) in the stratosphere, and would be greatly reduced by using a grid spacing of 100 m in the stratosphere. In summary, the unsaturated CMT is due to a mixture of vertical drafts near cumulus clouds edges and vertically propagating gravity waves.

Chapter 5

Prediction of the Zonal Wind Perturbation in the Updrafts U'_{up}

This chapter uses our CRM data sets to test the prediction of U'_{up} (the difference between the zonal wind within saturated updrafts and environmental wind, both averaged over the spatial domain) using a theoretical formula proposed by GKI97 that includes contributions from the horizontal pressure gradient force and lateral entrainment.

5.1 Evaluating the role of the cloud pressure-gradient force

In the previous chapter, we showed that CMT is mainly caused by motions within clouds, especially saturated updrafts, although momentum fluxes in unsaturated air due to gravity waves also are significant in the lower troposphere and in the stratosphere. CMT parameterizations have focused on the contribution of saturated air, and especially saturated updrafts, to CMT. Among such parameterizations, the one proposed by Kershaw and Gregory (1997) is attractive to compare to the 3D CRM data sets, since it clearly includes the roles of horizontal pressure-gradient force across the updrafts and entrainment processes in the vertical evolution of the horizontal velocity in the updrafts.

The cloud pressure-gradient term is poorly understood theoretically, so early efforts to formulate CMT parameterizations neglected this physical mechanism (for example, Shapiro and Stevens, 1980). Nevertheless, observational studies (Flatau and

Stevens, 1987) and modeling studies (e.g. Gregory and Miller, 1989) have indicated that the cloud pressure-gradient force plays an important part in determining the variation of horizontal velocity within the cloud as a parcel ascends. Kershaw and Gregory (1997) and GKI97, proposed that the vertical structure of the updraft horizontal velocity may be written in the form:

$$\frac{d\overline{U}_{up}}{dZ} = \varepsilon \left(\overline{U}_{env} - \overline{U}_{up} \right) + c^{*} \frac{d\overline{U}_{env}}{dZ} \tag{5.1}$$

where $\bar{U}_{up}$, $\bar{U}_{env}$ are the mean horizontal velocity in the updrafts and in the environment, respectively, ε is a bulk fractional lateral updraft entrainment rate in units of 1/km and c^* is an nondimensional empirical constant (to be determined) that relates the cloud pressure-gradient force to the mean vertical shear. Equation (5.1) can be derived from considering the force balance on a control volume in a representative quasi-steady cumulus updraft. The left-hand side of the equation represents the horizontal momentum added to the updraft air as it rises through the control volume, the first term on the right-hand side is related to the momentum source due to lateral entrainment of air into the updraft and the second term on the right-hand side is a representation of the cloud pressure-gradient force, which will be investigated in this section. Section 5.2 is dedicated to the investigation of the entrainment term in equation (5.1).

Analysis of the perturbation pressure gradient acceleration on updrafts

A relationship between the cloud pressure-gradient force and the mean vertical shear was first theoretically derived by Rotunno and Klemp (1982) who showed from a linear analysis that the pressure perturbation across an isolated updraft is related to the mean shear of the cloud environment and the updraft vertical velocity, the perturbation being parallel to the shear and acting to bring the updraft velocity back toward the mean environmental wind at each level. In 1988, Le Mone *et al.* in their observational study confirmed that this relationship qualitatively holds for updrafts of deep convective clouds. Wu and Yanai (1994) used Rotunno and Klemp's analysis to explain CMT in organized mesoscale convective systems over Midwestern USA, and proposed a parameterization of the cloud pressure-gradient force using updraft cloud-mass flux, mean vertical shear, and the orientation of the convective system to the shear.

GKI97 proposed a simpler formula that neglects the convective organization and which is equivalent to assuming

$$PGF_x = c^* w' \frac{d\overline{U}_{env}}{dZ} \tag{5.2}$$

where $PGF_x = -1/\rho \, \partial p'/\partial x$, ρ is the air density (kg/m^3), p' is the pressure perturbation field (Pa) and w' is the vertical velocity perturbation (m/s). In their study, based on cloud-resolving model simulations of a cold-air outbreak and a tropical deep convection case, they found that the optimal $c^* = 0.7$.

The rest of this section describes a similar analysis of our CRM data set, which is much longer and uses a bigger computational domain than used by GKI97. To accurately compute the cloud pressure-gradient force using model data, we take into account the grid staggering between horizontal velocity and pressure perturbation fields. We compare PGF_x with the right hand side of equation (5.2) at each level, and extract the ideal value for c^*. We then vertically integrate equation (5.1) to retrieve the $\bar{U}_{up}$ for each level of height and to compare it with the one simulated by the CRM and with the GKI97 scheme ($c^* = 0.7$).

The ideal c^* is calculated applying a linear regression to equation (5.2), in the form of $Y = m\,X$, where Y is horizontal component of the cloud pressure-gradient force, the slope m represents the best value for c^* and X is the product of the vertical wind perturbation by the mean vertical shear. This linear regression is constrained to go through the origin, as GKI97 had postulated, and is implemented only over the saturated updraft grid points. The linear regression is then performed over the grid levels for which the fractional area covered by saturated updrafts is greater than 1%. A separate value of c^* is calculated at each time averaged over each of our three tropospheric layers (please refer to section 4.1, Chapter 4, for their definition). The saturated downdrafts are also examined in an attempt to extend the GKI97 scheme to cumulus downdrafts. The pressure perturbation, the vertical velocity perturbation, the environmental wind, and the horizontal velocities within the cumulus updrafts and downdrafts are given by the 3D data set D64T10; the air density is given by the statistics data set D64T120-S. The time average of PGF_{xsup} and PGF_{xsdn} is weighted by the total number of saturated updraft and downdraft grid points, respectively, existing in every time step analyzed. Eight 3D volumes are analyzed for every Julian day considered. The results are shown first for the Julian day 358 that features vigorous deep convection and strong wind shear, and then for the 10-day period from Julian days (Jd) 350 to 359.

Julian Day 358

In Fig. 5.1.1. the vertical profiles averaged over the entire day, as well as time-height cross sections of the zonal wind perturbation U_p, the CMT, and the zonal component of the cloud pressure-gradient force PGF_x within the saturated updrafts (sampled every three hours) are displayed. The time-mean zonal pressure-gradient force is negative below 8 km, increasing in magnitude from surface to 6 km of height. A negative zonal component of the cloud pressure-gradient implies that the pressure tends to be higher to the east than to the west of a typical updraft, which would tend to accelerate the updraft in the negative (westward) direction. Above 5 km, the PGF_x accelerates the saturated updrafts in the positive (eastward) direction. At some heights, the PGF_x is in the same direction as the vertical derivative of the updraft zonal velocity perturbations but at other levels it is not, so PGF_x is not the only mechanism responsible for the U_p and CMT structures within the saturated updrafts. Similarly, the time evolution of PGF_x shows a large peak in the upper troposphere at Jd385.4, but these features are much less visible in U_p and saturated updraft CMT.

The vertical and temporal aspects of saturated downdrafts may be seen in Fig. 5.1.2. The PGF_x is rather weak except close to the tropopause near midday and does not strong resemble the saturated updraft PGF_x. The binning method applied to saturated up and downdrafts described fully in Chapter 4 indicated that the cumulus drafts may be controlled by different fluid dynamics; evaluating the cloud pressure-gradient force separately points in the same direction.

The vertical profiles of the fields involved in equation (5.2) are displayed in Fig. 5.1.3, for both cumulus up- and downdrafts. Below 8 km, the vertical wind shear profile is followed closely by the PGF_x vertical profile, while the vertical velocity perturbation is in the range 1.5 - 3 m s^{-1}. In the 10 - 14 km layer, the mean vertical wind shear is rather weak and negative and W_p is 1 - 2 m s^{-1}, whereas the PGF_x is positive, counter to the GKI97 formula. For the saturated downdrafts, the scenario is considerably different. The lower levels, where saturated downdrafts are present and there is some vertical wind shear, do show some PGF_x variation, especially below 6 km. The mid and upper levels display weaker magnitudes of PGF_x than in the saturated updrafts with significant variability in the profile that is hard to relate to features in W_p or in VWS vertical profiles, suggesting again a poor relationship between the two members of equation (5.2) in this region.

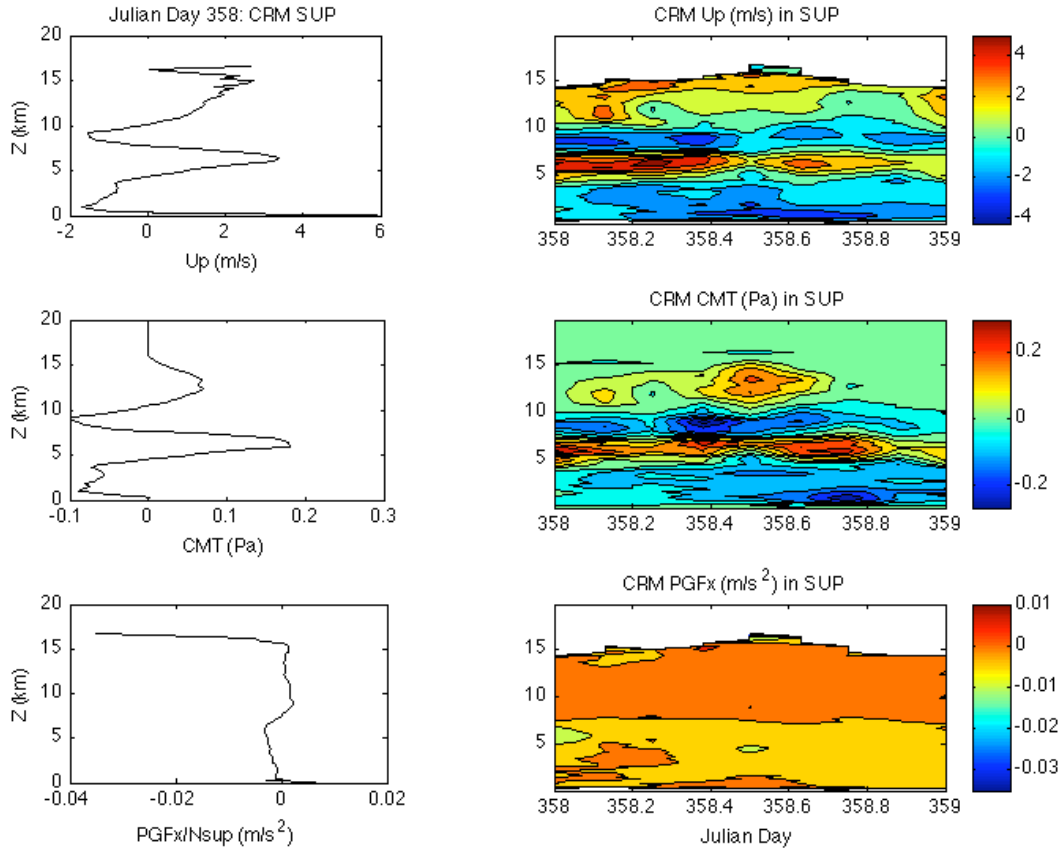

Figure 5.1.1. *Upper Left:* vertical profile of the zonal wind perturbation *Up* (m/s) averaged over the saturated updraft grid points and over the Julian day 358; *Upper Right:* time-height cross section of *Up* during the Jd 358, averaged over the saturated updraft grid points; *Middle Left:* vertical profile of the *CMT* (Pa) averaged over the saturated updraft grid points and over the Julian day 358; *Middle Right:* time-height cross section of *CMT* during the Jd 358; *Lower Left:* zonal pressure-gradient force PGF_x (m/s²) vertical profile average over the saturated updraft grid points and over the Jd 358, and *Lower Right:* time-height cross section of the PGF_x during the Jd 358, averaged over the saturated updraft grid points. All quantities are provided by 3D D64T10 simulation.

ZW03 do not show any vertical profiles related with the variables involved in (5.2) but they mention that " large positive values of PGF_x correspond to strong negative wind shear, such as that in the lower and middle troposphere on 24 December (…). Similarly, negative pressure-gradient appears where there is a strong positive wind shear ". This would correspond to a negative value of c^*, opposite to the findings of GKI97. In our simulations, these features are only verified in the upper troposphere for saturated updrafts and within the 5 - 8 km and 14 - 16 km layers for saturated downdrafts. Hence, the results obtained by ZW03 are not entirely confirmed by our 3D data sets.

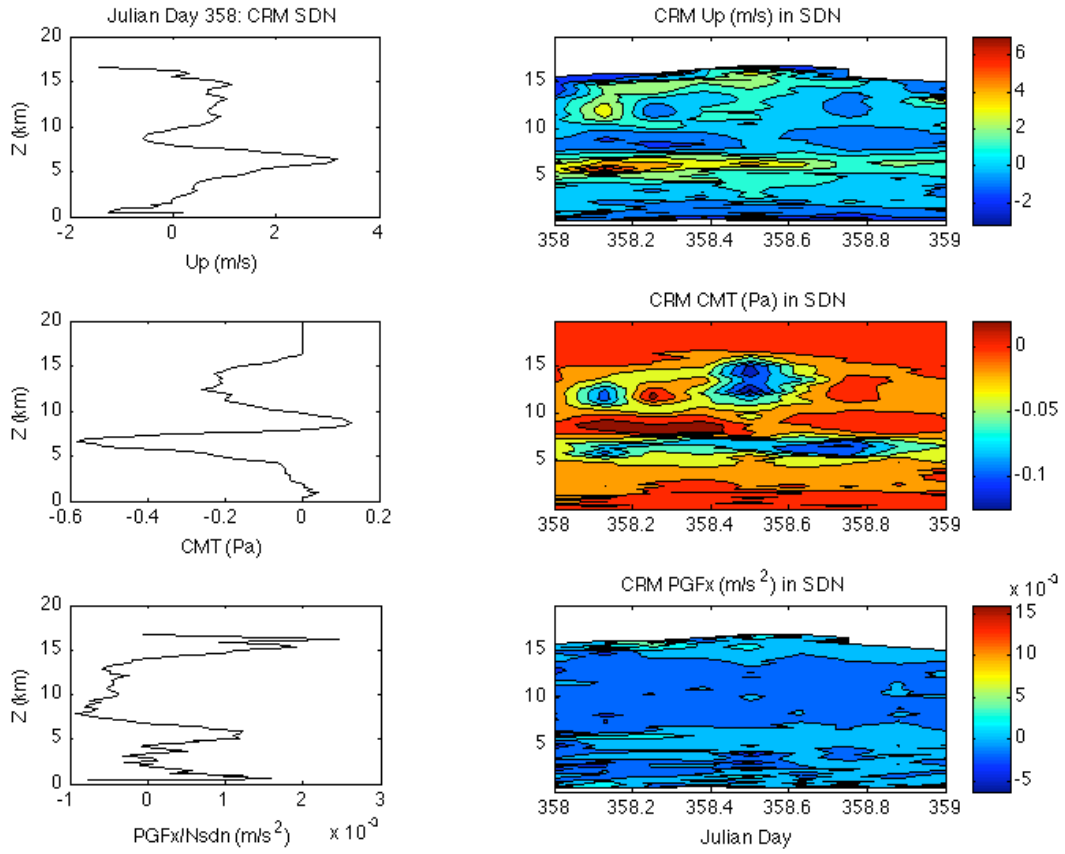

Figure 5.1.2. *Upper Left:* vertical profile of the zonal wind perturbation *Up* (m/s) averaged over the saturated downdraft grid points and over the Julian day 358; *Upper Right:* time-height cross section of *Up* during the Jd 358, averaged over the saturated downdraft grid points; *Middle Left:* vertical profile of the *CMT* (Pa) averaged over the saturated downdraft grid points and over the Julian day 358; *Middle Right:* time-height cross section of *CMT* during the Jd 358; *Lower Left:* zonal pressure-gradient force PGF_x (m/s²) vertical profile average over the saturated downdraft grid points and over the Jd 358, and *Lower Right:* time-height cross section of the PGF_x during the Jd 358, averaged over the saturated downdraft grid points.

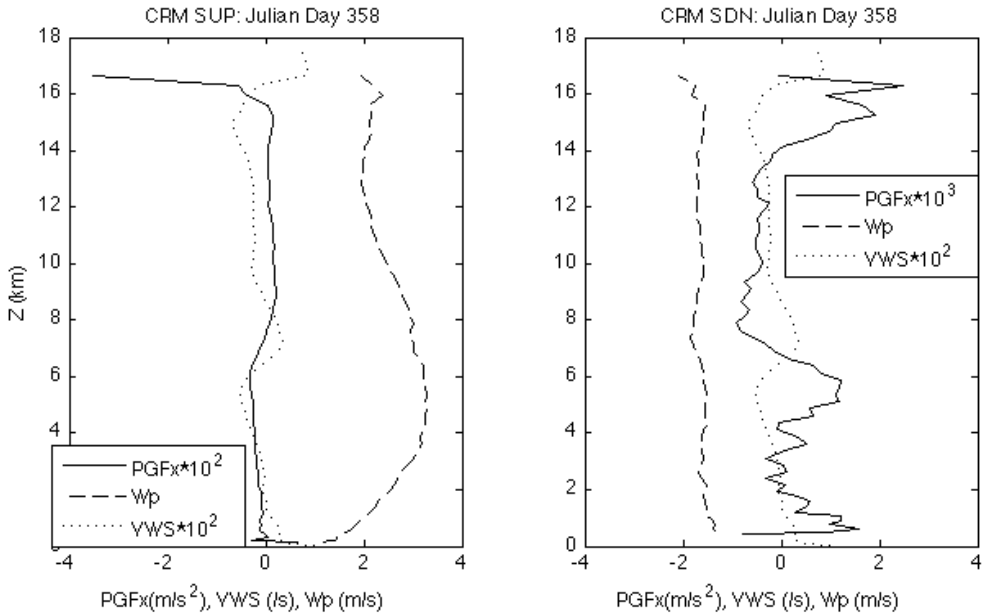

Figure 5.1.3. *Left:* vertical profiles of the mean vertical shear *VWS* (dotted line), of the vertical velocity perturbation *Wp* (dashed line) and of the zonal cloud pressure-gradient force PGF_x (solid line), averaged over the saturated updraft grid points and over the Julian day 358; *Right:* vertical profiles of the same fields, averaged over the saturated downdraft grid points and over the Jd 358. All quantities are provided by 3D D64T10 data set.

GKI97 suggested based on their results that 0.7 is an optimal value for c^*, for both their cold-air outbreak or tropical cases, and for both saturated updrafts and downdrafts. As can be seen in Figure 5.1.4, the zonal pressure-gradient force parameterization using this c^* for the whole troposphere does not always match the PGF_x simulated by the 3D cloud-resolving model. Below 8 km, within the lower and mid-troposphere, the parameterization performs somewhat reasonably in both cumulus up-and-downdrafts. However, within most of the upper troposphere, the parameterized PGF_x diverges significantly and even has the opposite sign from the CRM simulation, especially within cumulus updrafts.

In Figure 5.1.5, we see that the agreement is no better for other reasonable choices of c^*, except for smaller c^* values within saturated downdrafts. These results are consistent with ZW03's conclusion that c^* should not be the same for all heights.

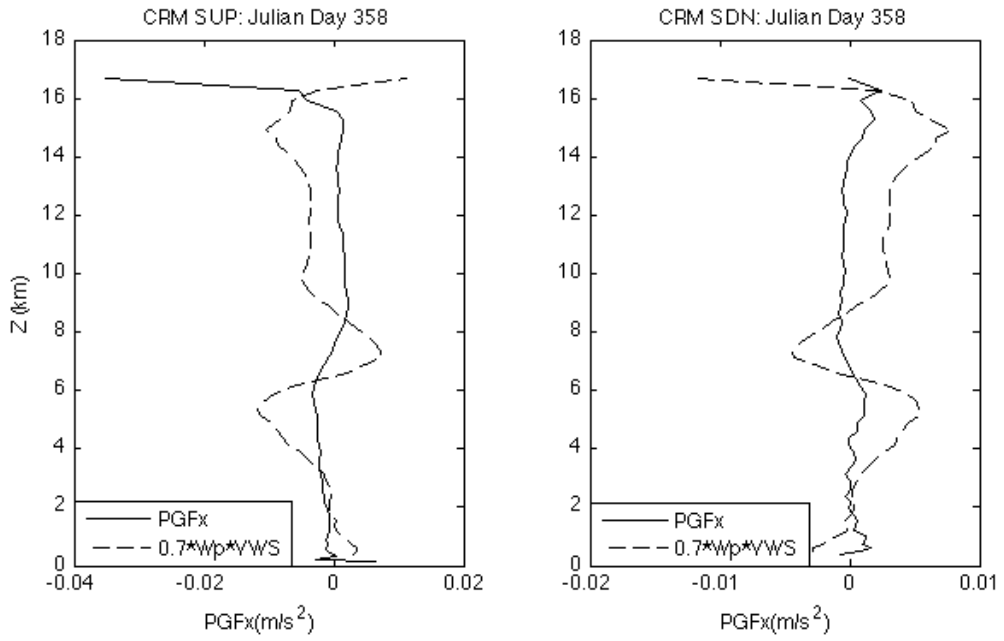

Figure 5.1.4. Vertical profiles of the two members of equation (5.2) proposed by GKI97: the PGF_x (m/s², solid line) and the product of c^* (0.7) by vertical velocity perturbation (m/s) by the mean vertical shear (/s) (dash line), averaged over the saturated updraft grid points (*Left* plot) and over the saturated downdraft grid points (*Right* plot), for Julian day 358. All the quantities are given by the 3D D64T10 simulation.

In the present work, the optimal c^* is achieved by applying a simple linear regression to equation (5.2) in respect to time, for each tropospheric layer, constrained to pass through the origin, treating the 8 times steps at which we have 3D volumes as independent samples. As in Section 4.1, the linear regression is applied to three tropospheric layers, and for each layer the slope of this line corresponds to the best c^* for that layer. Only vertical levels within that layer where the fraction of saturated updrafts or downdrafts is greater than 1% are considered, and both sides of (5.2) are area-weighted by the total number of saturated updraft (downdraft) N_{sup} (N_{sdn}) grid points.

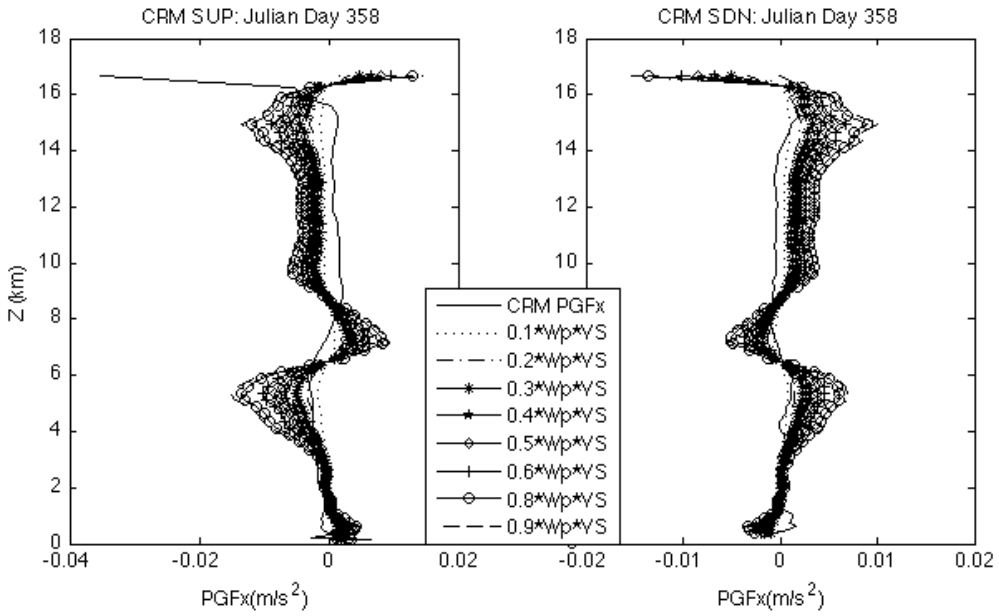

Figure 5.1.5. Vertical profiles of the two members of equation (5.2) proposed by GKI97: the PGF_x (m/s², solid line) and the product of c^* by vertical velocity perturbation (m/s) by the mean vertical shear (/s), considering several discrete choices for c^*, averaged over the saturated updraft (*Left plot*) and over the saturated downdraft (*Right plot*) grid points, for Julian day 358. All the variables studied are given by the 3D D64T10 simulation.

Figure 5.1.6 presents the best-fit slope (c^*) for saturated updrafts (first row) and saturated downdrafts (second row) obtained from applying the linear regression to parameterization (5.2) within the three layers of the troposphere. For the cumulus updrafts, both sides of the parameterization are strongly correlated in time (maximizing during the strong convective event near 12 UTC) in the upper troposphere only. In the middle troposphere the estimated slope is around 0.55, while for the lower and upper troposphere, the respective slopes of -0.41 and -0.29 are negative. These are all smaller than the value suggested by GKI97, and in two of the three cases of unexpected sign. However, these results are in good agreement with those found by ZW03 in their 2D CRM TOGA-COARE study, except in the upper-levels, where ZW03 obtained larger slope values. There are too few cumulus downdrafts in the lower tropospheric region to allow a real conclusion about c^*. In mid and upper level saturated downdrafts, there is more mass flux but the estimated slope values are very small in the upper troposphere and -0.4 in the mid levels and there is no correlation between the quantities analyzed, again contradicting GKI97's results.

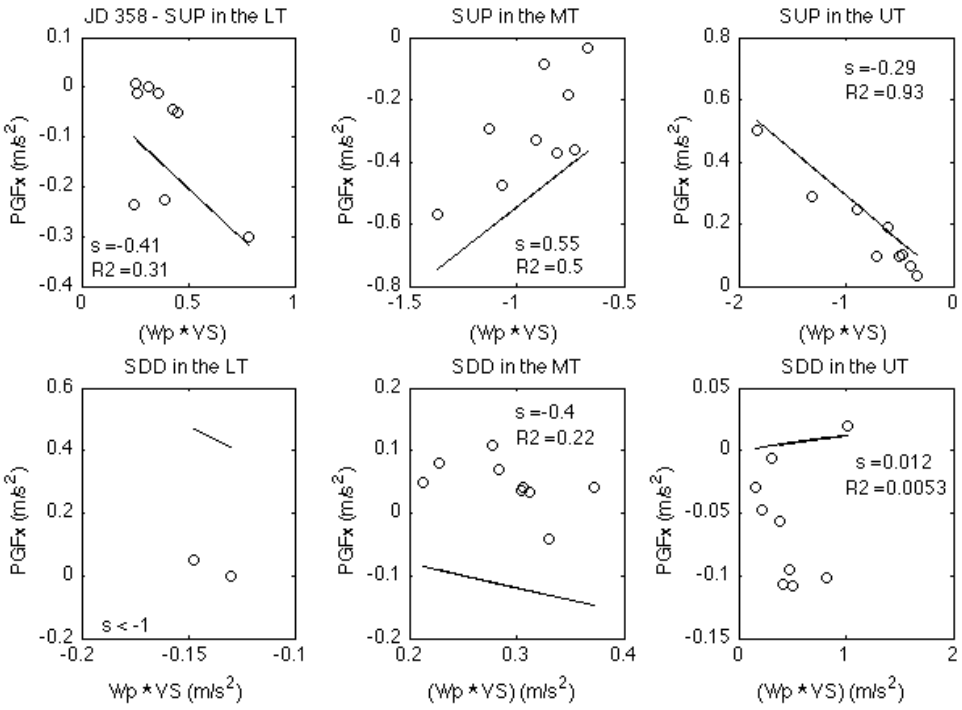

Figure 5.1.6. Linear regression applied to the equation (5.2) proposed by GKI97: the PGF_x as the predictand and the product of vertical velocity perturbation *Wp* (m/s) by the mean vertical shear *VS* (/s) as the predictor, averaged over the lower (*left column, LT*), the middle (*mid-column, MT*) and the upper (*right column, UT*) troposphere, within the saturated updraft grid points (*first row*) and over the saturated downdraft grid points (*second row*), for Julian day 358. All the quantities are given by the 3D D64T10 data set.

In summary, the 3D data sets used in this thesis do not support the GKI97 parameterization of the pressure-gradient force on saturated updrafts and downdrafts, at least for this specific case during this particular time window of one day.

Julian Days 350:359

Figures 5.1.7 and 5.1.8 display the vertical distributions and time-height cross sections of zonal wind perturbation, zonal momentum flux and zonal component of cloud pressure-gradient force, for saturated updrafts and downdrafts, respectively, for the 10-day simulation.

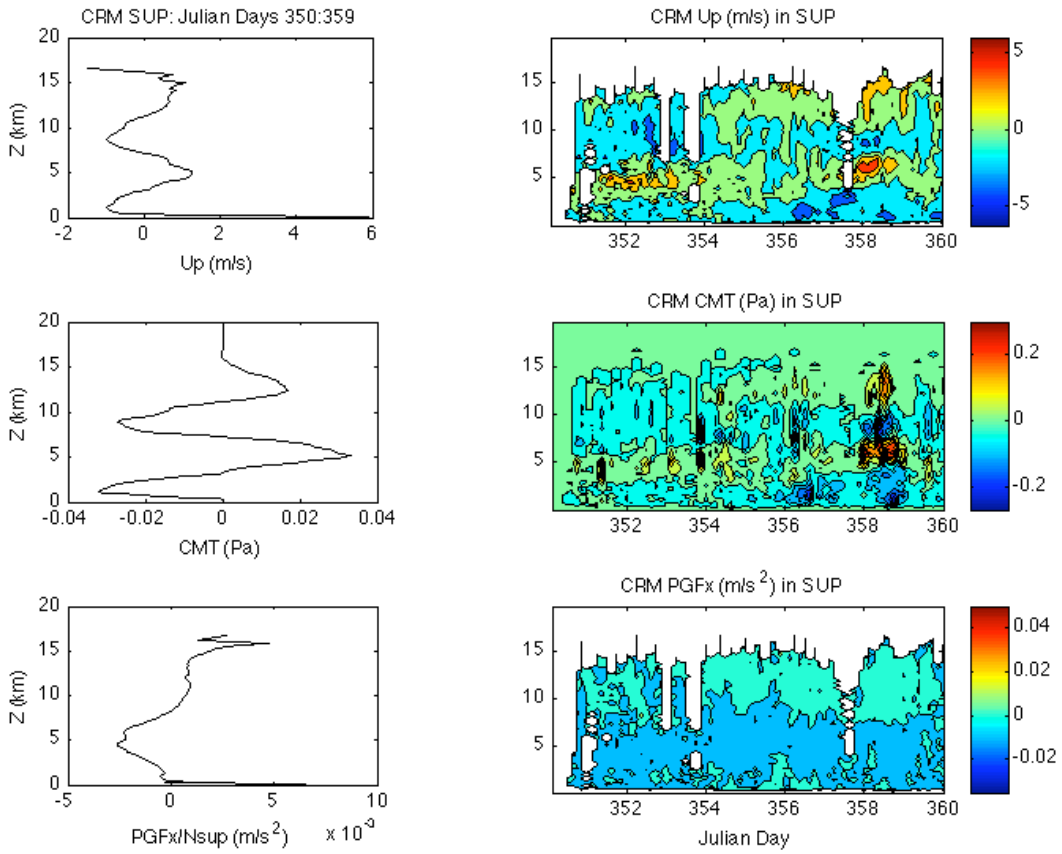

Figure 5.1.7. *Upper Left:* vertical profile of the zonal wind perturbation *Up* (m/s) averaged over the saturated updraft grid points and over the Julian days 350:359; *Upper Right:* time-height cross section of *Up* during the 10-day simulation, averaged over the saturated updraft grid points; *Middle Left:* vertical profile of the *CMT* (Pa) averaged over the saturated updraft grid points and over the Julian days 350:359; *Middle Right:* time-height cross section of *CMT* during the 10-days; *Lower Left:* zonal pressure-gradient force PGF_x (m/s²) vertical profile average over the saturated updraft grid points and over the 10-day period, and *Lower Right:* time-height cross section of the PGF_x during the 10-days time period, averaged over the saturated updraft grid points. All quantities are provided by 3D D64T10 simulation.

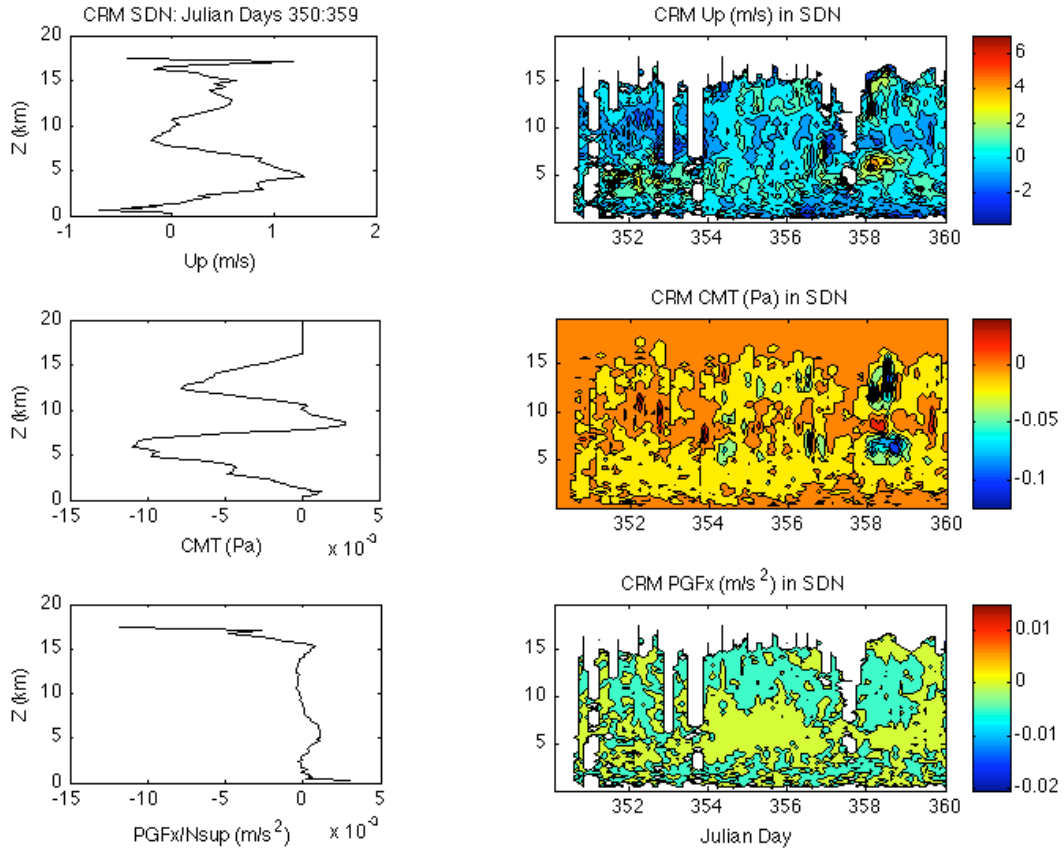

Figure 5.1.8. *Upper Left:* vertical profile of the zonal wind perturbation *Up* (m/s) averaged over the saturated downdraft grid points and over the Julian days 350:359; *Upper Right:* time-height cross section of *Up* during the 10-days simulation, averaged over the saturated downdraft grid points; *Middle Left:* vertical profile of the *CMT* (Pa) averaged over the saturated downdraft grid points and over the Julian days 350:359; *Middle Right:* time-height cross section of *CMT* during the 10-days; *Lower Left:* zonal pressure-gradient force PGF_x (m/s²) vertical profile average over the saturated downdraft grid points and over the 10-days period, and *Lower Right:* time-height cross section of the PGF_x during the 10-day time period, averaged over the saturated downdraft grid points. All quantities are provided by 3D D64T10 simulation.

Inside of cumulus updrafts, the 10-day mean PGF_x is negative from 2 km to 8 km of height and is positive beyond that altitude, showing a qualitatively similar time-mean vertical structure (averaged over spatial and time domains) compared with the one for Jd 358 shown in the lower left of Fig. 5.1.1, but weighted toward the levels of maximum fractional area covered by saturated updrafts. Therefore, the 10-day mean PGF_x and the zonal wind perturbation profiles show a clear correlation with the corresponding Jd358 vertical profiles. The zonal wind perturbation (Fig. 5.1.7 top) strongly shapes the CMT profile (Fig. 5.1.7 middle), both in the 10-day mean (left panels) and the time-height

evolution (right panels). For saturated downdrafts (Fig. 5.1.8), the conclusions from JD358 are also valid for the 10-day period, because the strong convective event dominates the time-mean vertical profiles of CMT and PGF_x.

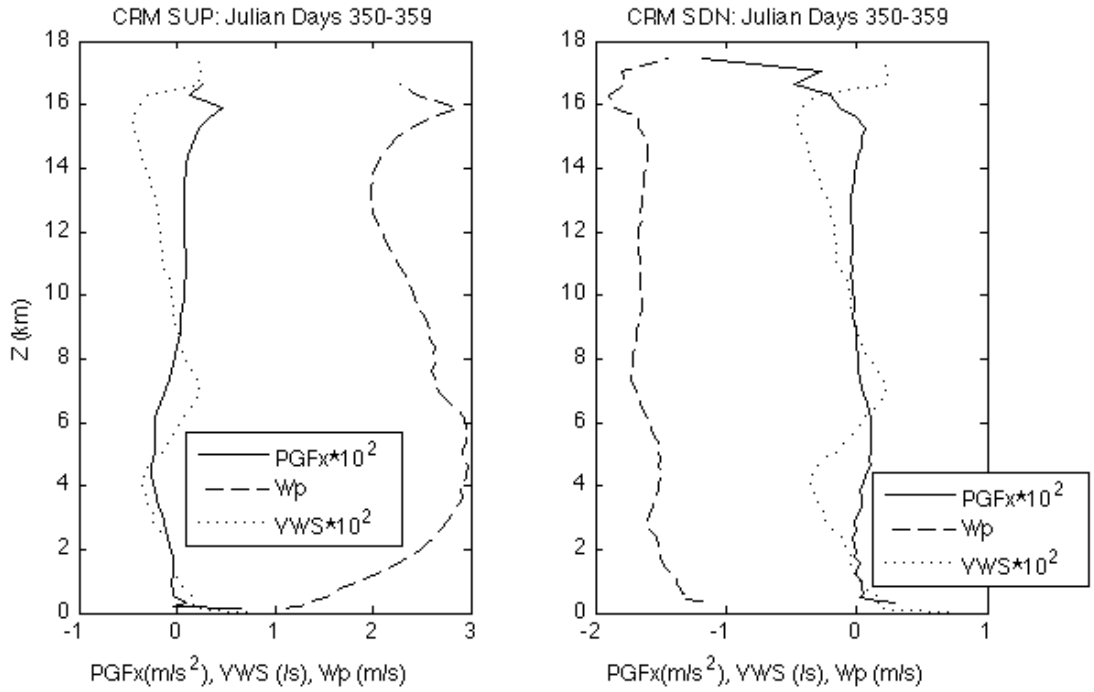

Figure 5.1.9. 10-day mean *v*ertical profiles of the mean vertical shear *VWS* (dotted line, magnitude of 10^{-2}), of the vertical velocity perturbation *Wp* (dashed line), of the zonal cloud pressure-gradient force PGF_x (solid line, magnitude of 10^{-2}) of saturated updrafts (*left*) and saturated downdrafts (*right*). All quantities are derived from 3D D64T10 simulation.

Figure 5.1.9 shows the 10-day mean vertical profiles of the quantities involved in GKI97's parameterization (5.2) for PGF_x. The results resemble those of the 1-day period shown in Fig. 5.1.3, since the strong deep convective event has a remarkable signature on the time-mean vertical profiles for this larger period of time, except in the upper troposphere for PGF_x in both cumulus drafts.

Figure 5.1.10 displays the corresponding vertical distributions of the two members of equation (5.2) for GKI97's recommended value c^*= 0.7 for both cumulus up-and downdrafts. As for Jd358, GKI97's approach simulates the 10-day area-weighted PGF_x quite poorly.

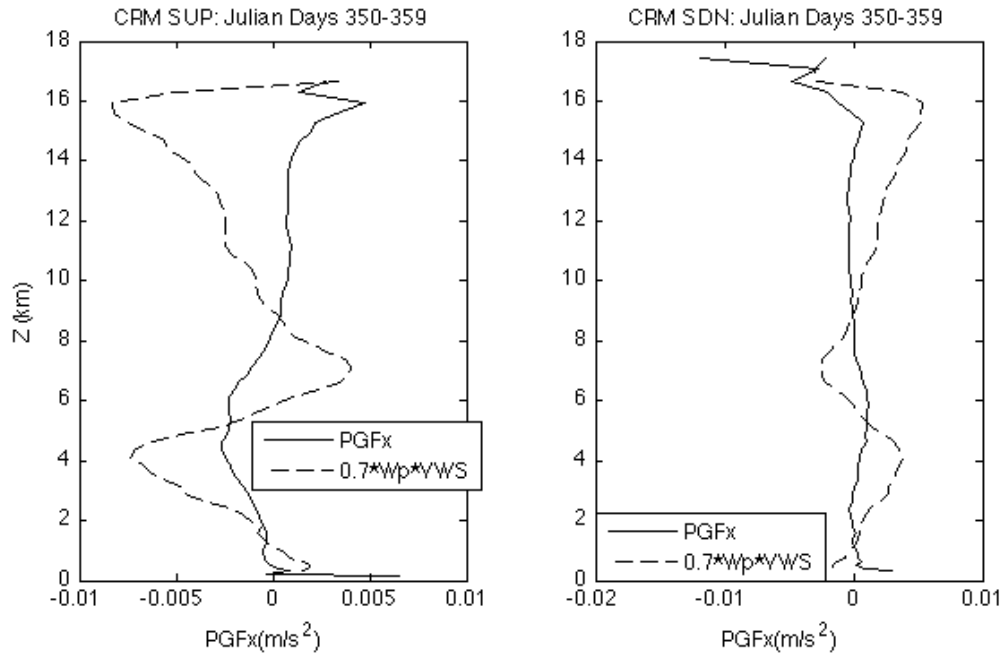

Figure 5.1.10. Vertical profiles of the two members of equation (5.2) proposed by GKI97: the PGF_x (m/s², solid line) and the product of c^* (0.7) by vertical velocity perturbation (m/s) by the mean vertical shear (/s) (dash line), averaged over the saturated updraft grid points (*Left* plot) and over the saturated downdraft grid points (*Right* plot), for the time period Jd 350:359. All the variables studied are given by the 3D D64T10 data set.

Following exactly the same procedure as for Julian day 358, linear regression over the 3hr-mean samples, for the 10-day period, averaged across the three tropospheric layers is performed on equation (5.2), estimating the best c^* value for each layer as the slope of the regression line (Figure 5.1.11). Compared to the Jd358 cumulus updraft results, the c^* is smaller in magnitude within the lower and middle troposphere but in the same range in the upper troposphere, and like for Jd358, the estimated c^* is positive only in the mid-troposphere. For the cumulus downdrafts, there is too little mass flux in the lower and mid-troposphere to meaningfully estimate c^*, but in the middle troposphere the estimated c^* is less than half of the one predicted for Jd358. Thus the Jd358 results, which contradict GKI97, also apply to the full 10-day simulation. The correlation among the variables involved in eqn (5.2) is still identifiable but smaller for saturated updrafts, in all tropospheric layers considered, compared with those for Jd358. The saturated downdrafts don't show any correlation at all. These results suggest that, for longer periods of time that include deep convective events, especially within cumulus updrafts, we still have both members of equation (5.2) somehow correlated with each other, and the optimal c^* still is in an acceptable range of values.

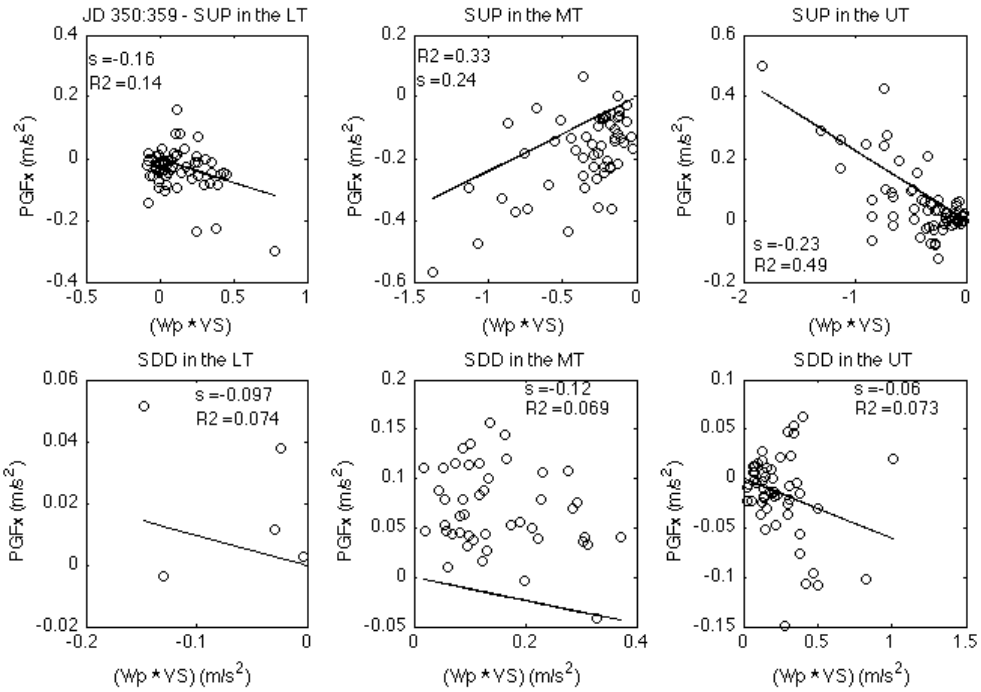

Figure 5.1.11. Linear regression applied to the formula (5.2) proposed by GKI97: the PGF_x as the predictand and the product of vertical velocity perturbation *Wp* (m/s) by the mean vertical shear *VS* (/s) as the predictor, averaged over the lower (*left column, LT*), the middle (*mid-column, MT*) and the upper (*right column, UT*) troposphere, within the saturated updraft grid points (*first row*) and within the saturated downdraft grid points (*second row*), for the time period Julian days 350:359. All the quantities are given by the 3D D64T10 simulation.

5.2. The prediction of cumulus updraft zonal velocity perturbation

To compute the saturated updraft CMT using the mass flux approximation, we need $\bar{U}_{env}$ - $\bar{U}_{up}$, which we calculate by vertically integrating equation (5.1) for the updraft zonal momentum. Section 5.1 explored the second term on the right-hand side (hereafter RHS) of (5.1), which parameterizes the pressure-gradient force on the updraft; we now briefly discuss the first 'entrainment' term on the RHS of (5.1) and then compare

predictions from (5.1) with our CRM results.

The entrainment process is associated with a transfer of mass flux into the cloud, which we quantify as a relative entrainment rate ε, per unit of height. That is, as an updraft with mass flux M rises a small height increment dZ, a mass flux $\varepsilon M dZ$ of environmental air (assumed to also have the environmental value of zonal velocity) is mixed into the updraft. The first term of the RHS of (5.1) represents this 'entrainment dilution' of the updraft momentum.

The entrainment rate is empirically specified to be $\varepsilon = 0.6/Z$, where Z is the altitude. This rate was derived from the profile of moist static energy in saturated updrafts, which below the freezing level is solely affected by entrainment. Introducing this fractional entrainment rate into equation (5.1) and considering a range of values for c^* (which scales the pressure gradient term), the updraft zonal momentum equation is then integrated upward from cloud base to the tropopause after discretization using the forward Euler scheme, starting with the CRM-simulated zonal wind at the cloud base level averaged over the saturated updraft grid points.

Julian Day 358

To show the role of entrainment alone in modifying the updraft zonal wind profile, we integrate the formula (5.1) with $c^* = 0$, shutting down the pressure-gradient force term. Figure 5.2.1 compares this profile and the updraft zonal wind perturbation from the environment with those simulated by the CRM averaged over Julian Day 358. The entrainment contribution by itself captures well the horizontal velocity inside the cumulus updrafts in the lower-levels of the cloud. Above 4 km of height, the parameterized zonal velocity within the cumulus updrafts diverges significantly from the CRM profile, with differences exceeding 10 m/s in the upper troposphere, although the vertical evolution of both profiles presents the same qualitative features. The CRM-derived PGF_x is positive in the upper troposphere (Fig. 5.1.1) and would increase U_{sup} rather than decreasing it as needed, making the discrepancy between (5.1) and the CRM U_{sup} even worse there.

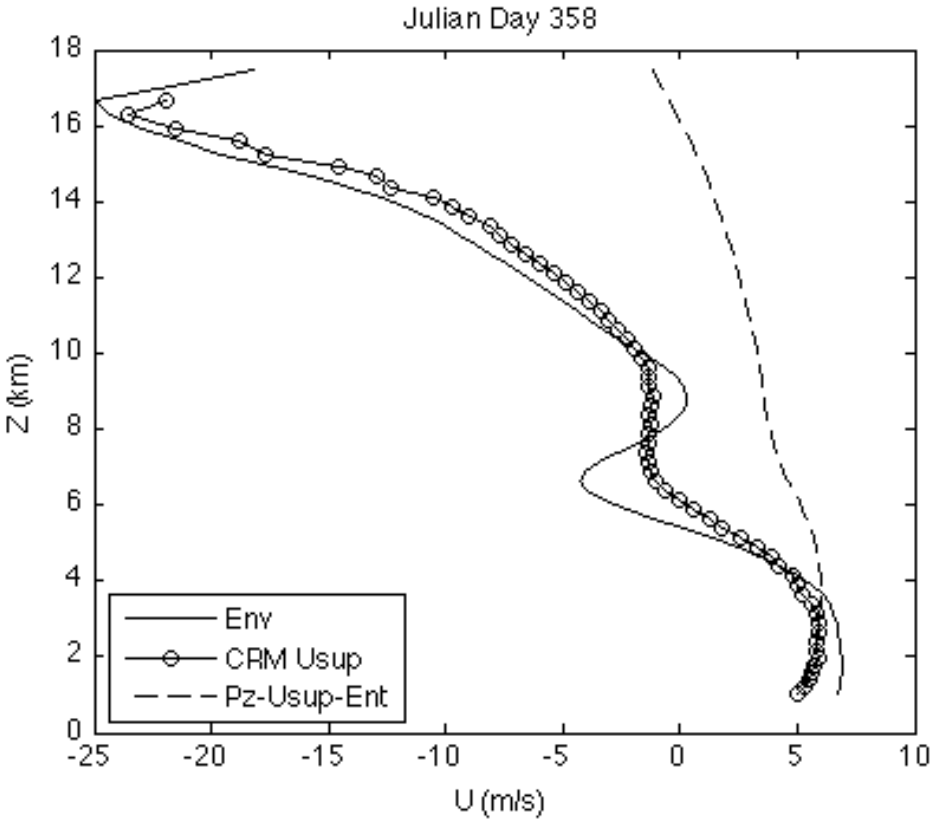

Figure 5.2.1. Vertical profiles of the CRM mean environmental wind *Env* (m/s, solid line), the cumulus updraft zonal velocity *CRM Usup* (m/s, circled line) simulated by the CRM and the parameterized cumulus updraft zonal velocity given by equation (5.1) assuming the action of entrainment only, discarding the contribution from the pressure-gradient force (m/s, dashed line). All the profiles are given by the 3D D64T10 data sets.

The values based on the linear regression analysis for PGF_x do not improve the entrainment-only fit, which is discouraging. If we ignore this analysis and just assume different c^* choices constant over height, we obtain the colored curves for U_{sup} in the left panel of Fig. 5.2.2. Reasonable agreement, especially above 10 km, is obtained using the two highest c^* (0.8 - 0.9). One could also get reasonable U_{sup} profiles using the linear regression analysis for PGF_x to specify c^* in each tropospheric layer and strongly increasing the lateral entrainment rate ε in the middle and especially in the upper troposphere beyond that diagnosed from the CRM. Either way, our analysis reveals a lack of fundamental understanding of the factors determining the updraft zonal velocity in vigorous, strongly sheared deep convection.

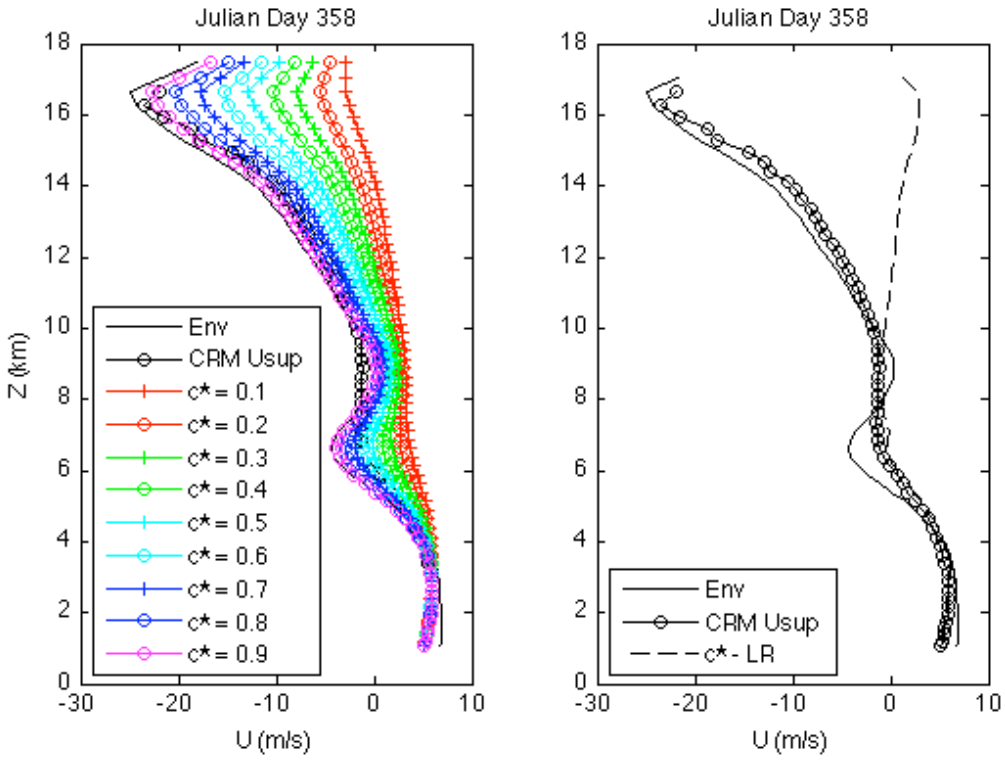

Figure 5.2.2. *Left plot*: vertical profiles of the CRM mean environmental wind Env (m/s, solid line), the cumulus updraft horizontal velocity CRM Usup (m/s, circled line) simulated by the CRM and the parameterized cumulus updraft horizontal velocity given by equation (5.1), under different c^* choices constant over height (m/s, colored lines). *Right plot*: the same vertical profiles for environmental (solid line) and simulated CRM zonal wind averaged over the cumulus updrafts (circled line), and the cumulus updraft zonal wind predicted by parameterization (5.1) using c^* given by the linear regression slope. All data is given by the 3D D64T10 simulation.

Julian Days 350:359

For the 10-day period, the results gotten by testing the GKI97 parameterization are are close to those obtained for Jd 358. Figure 5.2.3 shows the vertical variation of cumulus updraft zonal wind (*Usup*) given by (5.1) including only the contribution by the entrainment process, that is the cloud pressure-gradient force is turned off. As on Jd 358, the entrainment contribution alone does not reproduce the vertical variation of the simulated zonal wind inside the cumulus updrafts throughout the troposphere, except in a narrow layer near the cloud base, although it produces qualitatively the right profile shape, suggesting that a greater ε could bring these two profiles together.

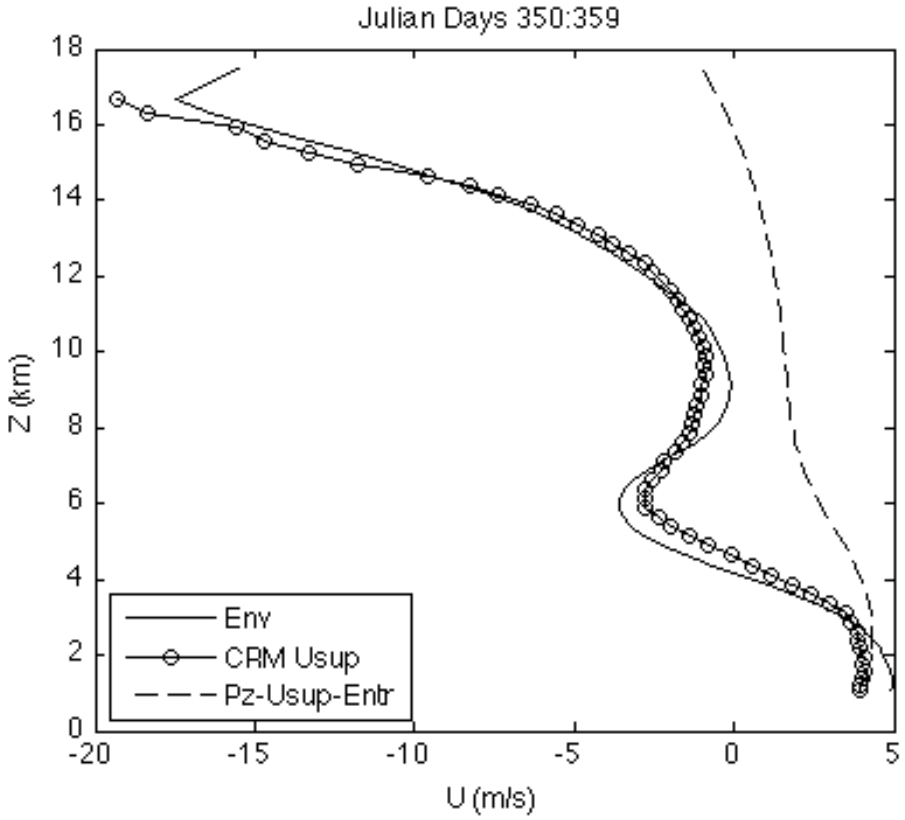

Figure 5.2.3. *V*ertical profiles of the CRM mean environmental wind *Env* (m/s, solid line), the cumulus updrafts horizontal velocity *CRM Usup* (m/s, circled line) simulated by the CRM and the parameterized cumulus updraft horizontal velocity given by equation (5.1) assuming the action of entrainment only, discarding the contribution from the pressure-gradient force (m/s, dashed line). All the profiles are given by the 3D D64T10 data sets and are averaged over the 10-day period.

Figure 5.2.4 shows the cumulus updraft zonal wind vertical profiles predicted by GKI97's scheme considering both terms of the RHS of (5.1). In the left plot, in which several discrete c^* values are considered, $c^* = 0.9$ retrieves the closest parameterized zonal velocity vertical distribution to the corresponding CRM zonal wind profile, throughout most of the troposphere. Using the linear regression slope for c^* (right plot) in (5.2), the predicted vertical distribution of the zonal wind inside cumulus updrafts is far from the CRM *Usup* profile in the middle and most part of upper troposphere. As a result, the zonal wind perturbation predicted by (5.1) is overestimated in these tropospheric regions. In summary, these results are similar to those obtained from the analysis of Jd358.

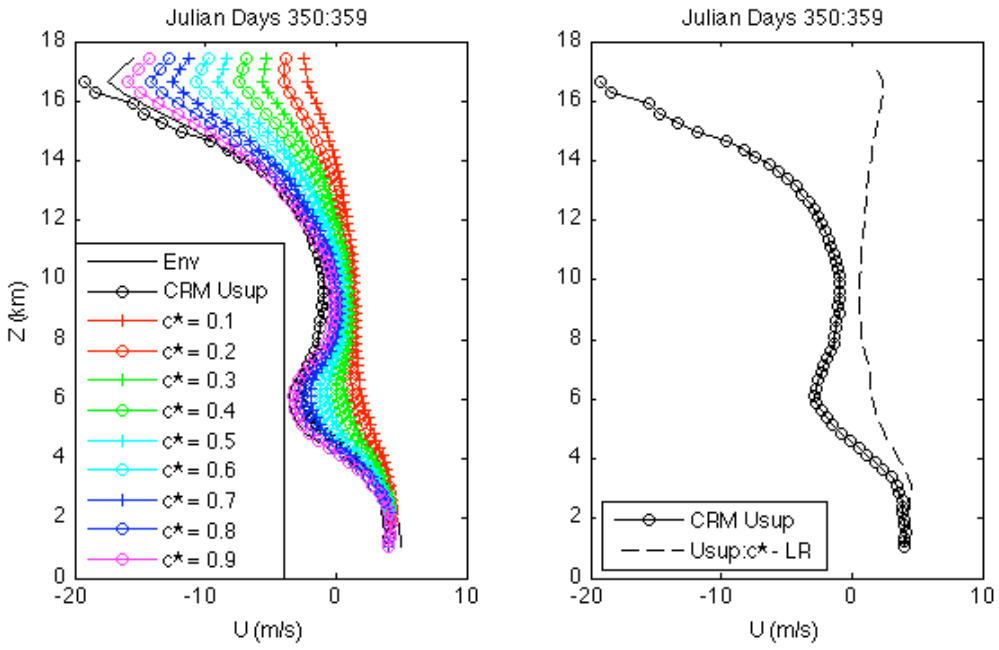

Figure 5.2.4. *Left plot*: vertical profiles of the CRM mean environmental wind 'Env' (m/s, solid line), the cumulus updraft horizontal velocity 'CRM Usup' (m/s, circled line) simulated by the CRM and the parameterized cumulus updraft horizontal velocity given by equation (5.1), under different c* choices constant over height (m/s, colored lines). *Right plot*: vertical profiles of the simulated cumulus updraft zonal wind 'CRM Usup' (circled line) and the parameterized cumulus updraft zonal wind with c* given by the linear regression slope. All data is given by the 3D D64T10 simulation and averaged over the 10-day time period.

5.3. Testing the mass-flux approach to convective momentum transport parameterization

The mass-flux approximation for cumulus updrafts only was introduced in eqn. (4.1). Kershaw and Gregory (1997) suggested cumulus updrafts and downdrafts both contribute to CMT, leading to the more general mass-flux approximation that we will analyze in this section,

$$CMT = M_{up}\left(\overline{U}_{up} - \overline{U}_{env}\right) + M_{dn}\left(\overline{U}_{dn} - \overline{U}_{env}\right) \tag{5.3}$$

where M_{up} is the updraft cloud mass flux, M_{dn} is the downdraft cloud mass flux, $\bar{U}_{env}$ is the

mean flow, and $\bar{U}_{up}$ and $\bar{U}_{dn}$ are the domain-averaged zonal velocities conditionally sampled inside the cumulus updrafts and downdrafts, respectively. The left-hand side of (5.3) represents the total CMT, the first term of the right-hand side of (5.3) represents the CMT within the cumulus updrafts and the second term of the right-hand side regards the CMT within cumulus downdrafts. This formulation examines the effects of updrafts and downdrafts separately, and consequently implies that the fundamental issue of predicting the total CMT (left-hand side of (5.3)) is to parameterize the cumulus updraft and downdraft mass fluxes and the mean horizontal velocities inside of them.

In this section, we evaluate the mass-flux approximation against CMT simulated by the 3D cloud-resolving model using 3-dimensional CRM data to evaluate the variables on the right hand side of (5.3), for instance the cloud mass fluxes. We will derive the updraft and downdraft zonal velocity perturbation from the CRM, rather than trying to predict them with a vertical velocity equation as investigated in the previous two sections. Thus, we are testing the fundamental suitability of a 'perfect' mass-flux parameterization for representing the CMT simulated by the CRM.

The data sets D64T10 and D64T120-S provide the data to test this parameterization. The first data set is the 3-hourly 3-dimensional output from which the horizontal velocities and horizontal velocity and vertical velocity perturbation are extracted. The statistics simulation provides the hourly cloud mass flux profiles averaged over the spatial domain (64 x 64 km^2). The formula (5.3) is applied to two different time periods: Julian day 358, the deep convective event day, and the 10-day period from Julian days 350 to 359, which includes this episode.

Julian Day 358

Figure 5.3.1. presents the vertical variations of the cloud updraft and downdraft mass fluxes and CMT contributions derived from the CRM and averaged over Jd 358. Total cloud mass flux and especially total CMT are primarily shaped by the contribution from cumulus updrafts. The cumulus updraft mass flux is large throughout the troposphere, as discussed in Chapter 3.

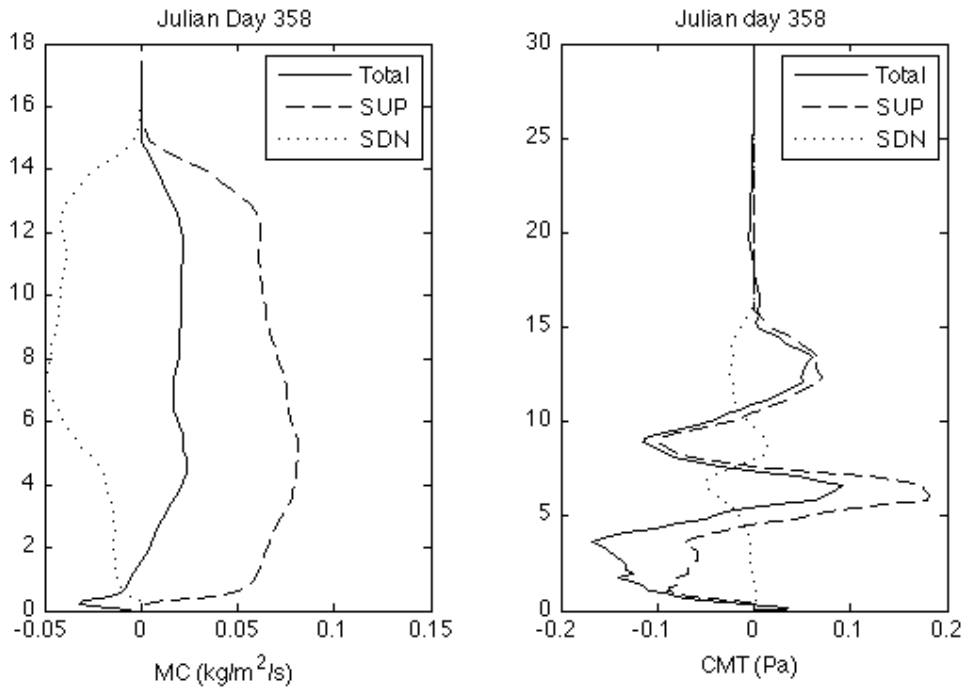

Figure 5.3.1. *Left plot*: vertical profiles of total cloud mass flux (kg/m²/s, solid line), updraft cloud mass flux (kg/m²/s, dashed line) and downdraft cloud mass flux (kg/m²/s, dotted line) given by the D64T120-S data set; *Right plot*: vertical profiles of total CMT (Pa, solid line), CMT within cumulus updrafts (Pa, dashed line) and CMT within cumulus downdrafts (Pa, dotted line) given by the 3D data set D64T10.

Figure 5.3.2 compares the two sides of equation (5.3) each computed using the CRM, for the eight times saved during Jd 358. Overall, the mass-flux approximation works fairly well, assuming perfect knowledge of the mass fluxes and the saturated updraft/ downdraft zonal velocity perturbations. The most important centers of negative and positive CMT are fairly well captured by the parameterization. The magnitudes of the mass-flux estimated CMT are slightly smaller than the CRM-estimated CMT (top plots). The negative values below 5 km and around 10 km are slightly underestimated by the mass-flux approximation, especially toward the end of the day. The mass-flux approximation also applies quite well to the CMT in cumulus (saturated) updrafts (middle plots). The parameterization does acceptably, but less well, within the cumulus downdrafts, for which it underestimates the magnitude of CMT variations (bottom plots).

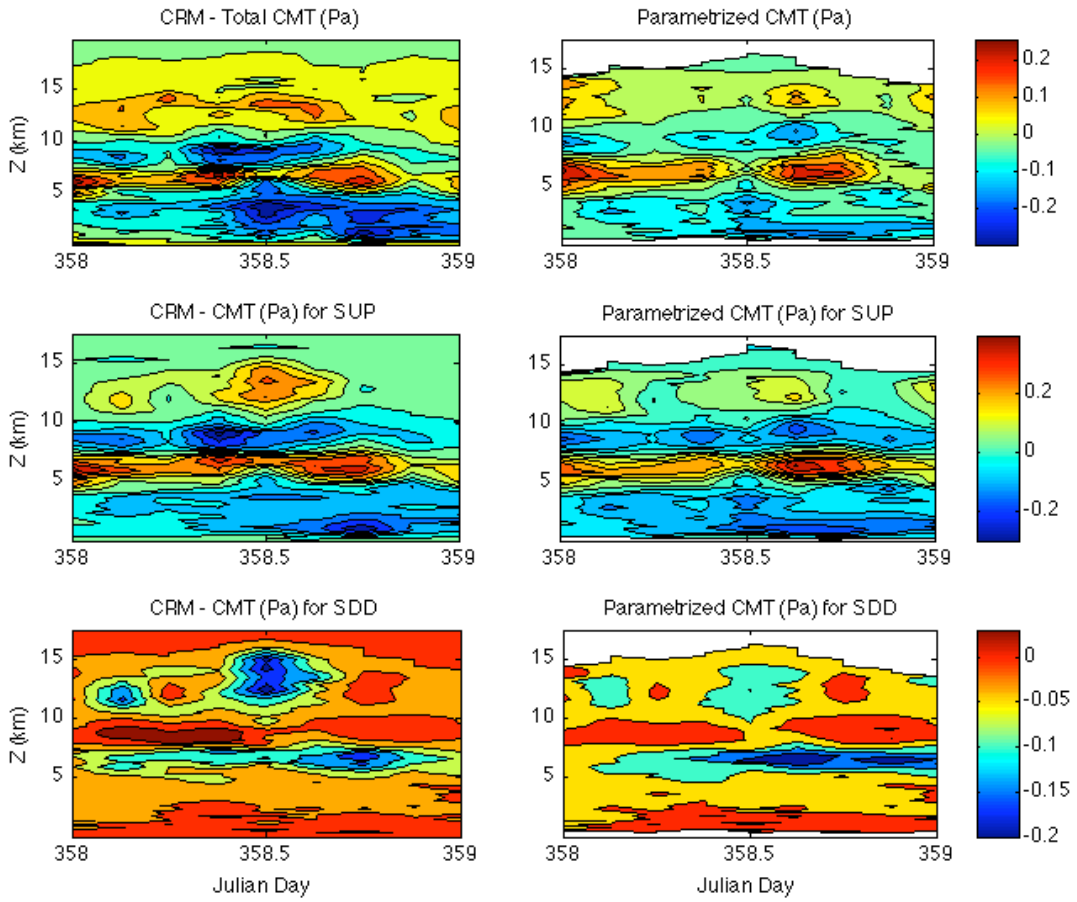

Figure 5.3.2. Comparison between the CMT simulated by the cloud-resolving model and the CMT given by equation (5.3). *Left column:* time-height cross sections of total CMT (top plot), cumulus updrafts CMT (middle plot) and cumulus downdrafts CMT (bottom plot) simulated by the 3D CRM. *Right column:* time-height cross-section of total CMT (top plot), CMT within cumulus updrafts (middle plot) and CMT within cumulus downdrafts (bottom plot) all obtained by the parameterization (5.3). White regions represent regions with no data.

Figure 5.3.3 displays the vertical profiles of the total, updraft and downdraft CMT, given by the CRM and by the mass-flux approximation (5.3), averaging over the 8 time steps that compose Julian day 358. The time-averaging smoothes out the differences between the simulated and parameterized CMT. The total CMT is still underestimated in its negative values and overestimated in its positive magnitudes, but is qualitatively well captured by the mass-flux approximation. The greatest difference is located between the cloud base and 5 km, and both profiles match well above 10 km. The CMT profiles within cumulus updrafts and downdrafts are extremely well reproduced by the mass-flux approximation, except for a slight overestimation of the peak value at 6 km of height. The

slight difference is due to small 'eddy' contributions to the saturated updraft and downdraft CMT due to positive correlations between zonal and vertical velocity perturbations within each of these categories. We infer that the difference seen in total CMT is mostly due to the contribution of unsaturated air, especially in form of downdrafts, to total CMT, which is strongest below 5 km (please refer to Fig. 4.2.1). The mass-flux approximation does not consider the role of unsaturated air upon CMT, but the cloud-resolving model does.

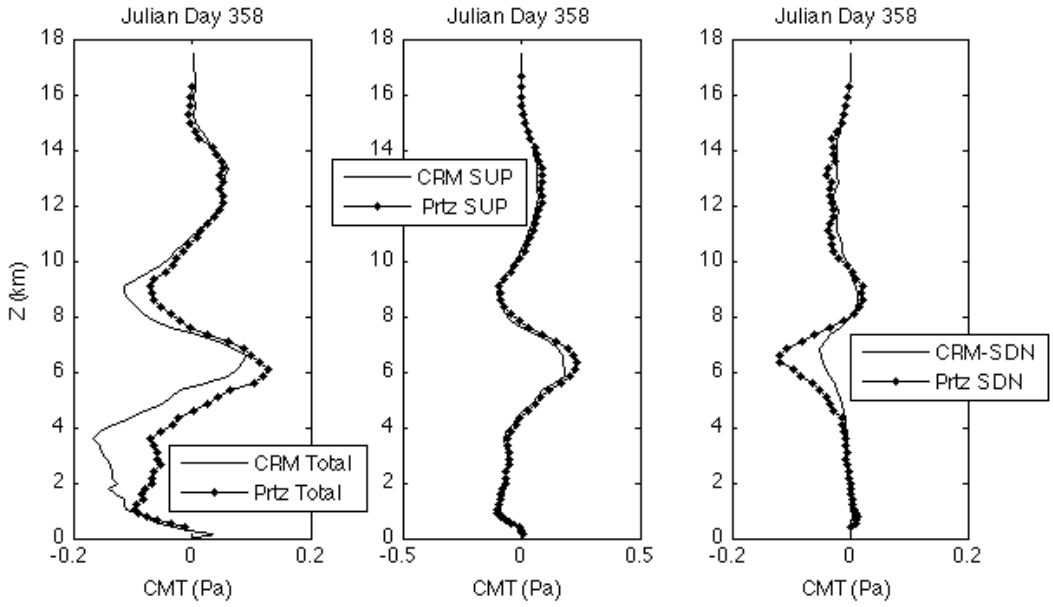

Figure 5.3.3. Vertical profiles of CRM (solid line) and parameterized (dotted lined) CMT (Pa): total (left plot), within cumulus updrafts (mid-plot) and within cumulus downdrafts (right plot), for Julian day 358.

The temporal correlation coefficients between the mass-flux approximation to CMT and the exact simulated CMT vary with height, but are generally high. Close to the cloud base level and above 4 km, the correlation between these fields is above 70% in most levels, confirming the effectiveness of this approximation.

The differences between the mass-flux approximation and the simulated total CMT may be investigated by calculating the residual of equation (5.3), shown in Figure 5.3.4 for the CRM. This residual is the sum of the unsaturated air contribution and smaller 'eddy' contributions to the CMT due to positive correlations between zonal and vertical velocity perturbations within each of these categories. As one might also infer from the left panel of Fig. 5.3.3, the simulated residual CMT is not negligible, especially in the lower and mid-

troposphere. However, compared to the profound problems we have found in predicting UP_{sup}, the overall inaccuracy in the mass-flux approximation seems like a less important source of error in predicting CMT.

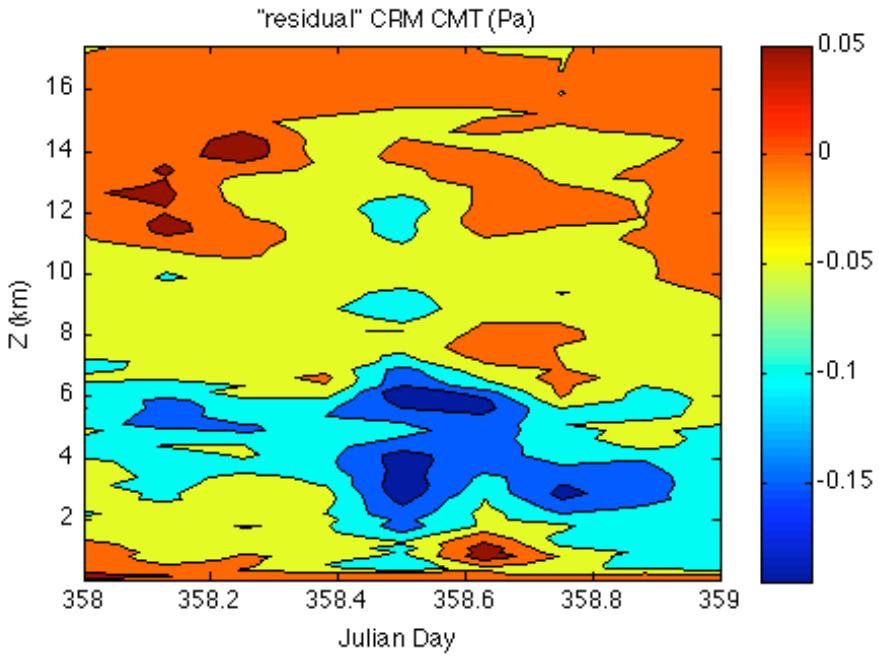

Figure 5.3.4. Time-height cross-section of the 'residual' CMT, simulated by the CRM, obtained as the difference between total CMT and CMT contributed by cumulus drafts, for Julian day 358.

Julian Days 350:359

For the 10-day period, the results obtained from the same approach are, as expected, considerably similar. The vertical structure of the cloud mass fluxes and CMT inside cumulus updrafts and downdrafts are displayed in figure 5.3.5. The ten-day average cloud mass flux profiles have similar shape but slightly smaller magnitude than those simulated for Jd 358, which was a period of particularly intense convection, but are otherwise similar to that day. However, the CMT vertical structures are somewhat different from those in Jd 358. The total ten-day mean CMT is about half than that for Jd 358, and is negative throughout most of the troposphere. The 10-day mean vertical structure of total CMT somewhat follows the cumulus updrafts CMT vertical profile but the fraction of the CMT explained by the saturated updrafts and downdrafts is smaller

than for Jd358, especially in the lower troposphere. That is, unsaturated vertical motions are doing most of the CMT at the lower levels, and the CMT due to these motions is consistently negative throughout the troposphere, but particularly from cloud base up to 8 km. Figures 5.3.7 and 5.3.6 compare the mass-flux approximation (5.3) and the corresponding fields simulated by the CRM for saturated updrafts, saturated downdrafts and the entire CMT.

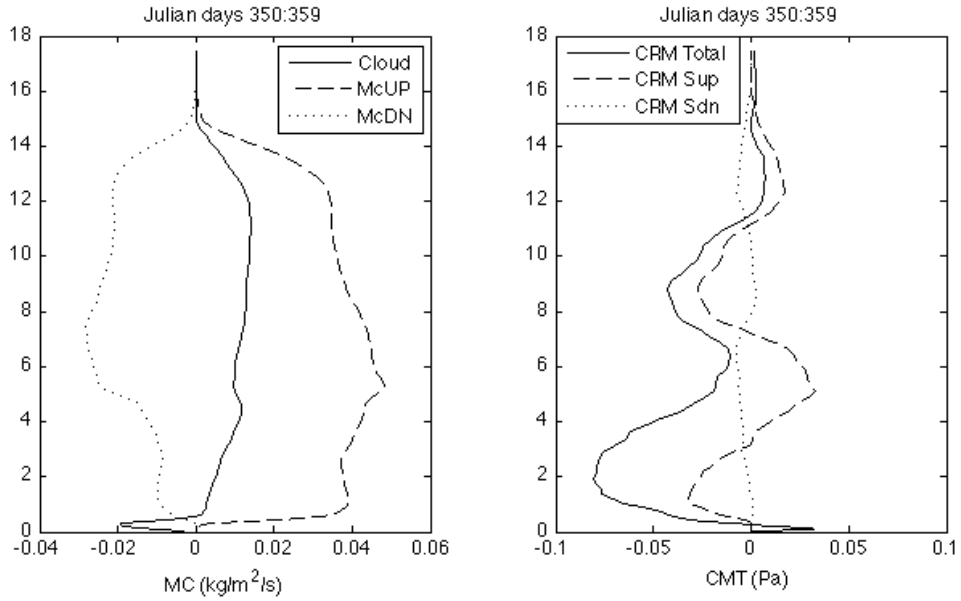

Figure 5.3.5. *Left plot*: vertical profiles of total cloud mass flux (solid line), updraft cloud mass flux (dashed line) and downdraft cloud mass flux (dotted line) given by the D64T120-S data set; *Right plot*: vertical profiles of total CMT (solid line), CMT within cumulus updrafts (dashed line) and CMT within cumulus downdrafts (dotted line) given by the 3D data set; all profiles are averaged over the 10-day period.

The mass-flux approximation accurately captures most of the day-to-day variability in the cumulus updrafts (middle panels) and downdrafts (lower panels), but does not include the large contribution from unsaturated CMT. The vertical profiles of the the 10-day mean CMT and the mass-flux approximation are exhibited in Figure 5.3.8. These panels also show that the mass-flux approximation is noisy but generally tracks the CMT for both saturated updrafts and downdrafts, with larger errors in the total CMT. As in Jd358 analysis, the implication is that biggest error in the mass flux representation of CMT is its neglect of unsaturated CMT. This error can be clearly seen in Figure 5.3.9, which displays the 'residual' for CRM CMT, computed as the difference between the total CMT and the mass-flux representation, and which is dominated by the unsaturated CMT.

As for Jd358, this contribution is of the same magnitude as the total CRM CMT in the lower troposphere, where it is a dominant source of negative cumulus momentum fluxes throughout the period, and especially on the days leading up the deep convective event (Jd356-358).

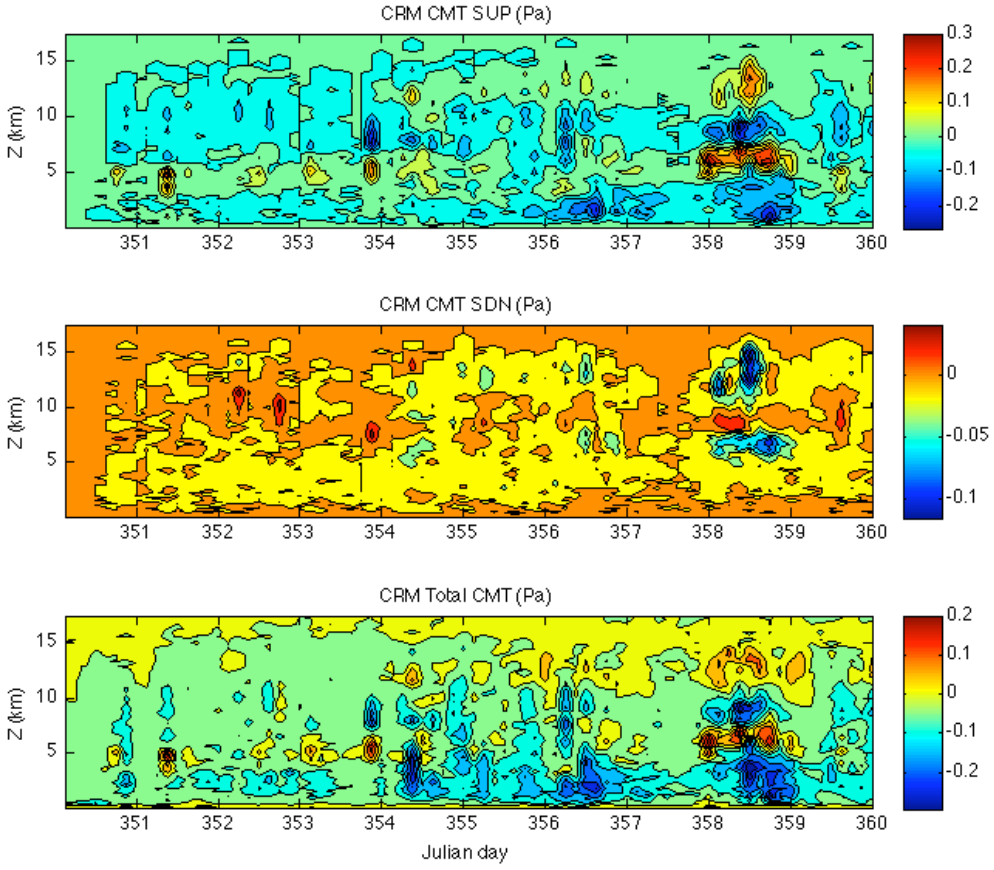

Figure 5.3.6. CMT simulated by the 3D cloud-resolving model: time-height cross sections of the CMT contributed by cumulus updrafts (*top plot*), cumulus downdrafts (*middle plot*) and total CMT (*bottom plot*). Data provided by the data sets D64T120-S and 3D D64T10, for the 10-day period of simulation.

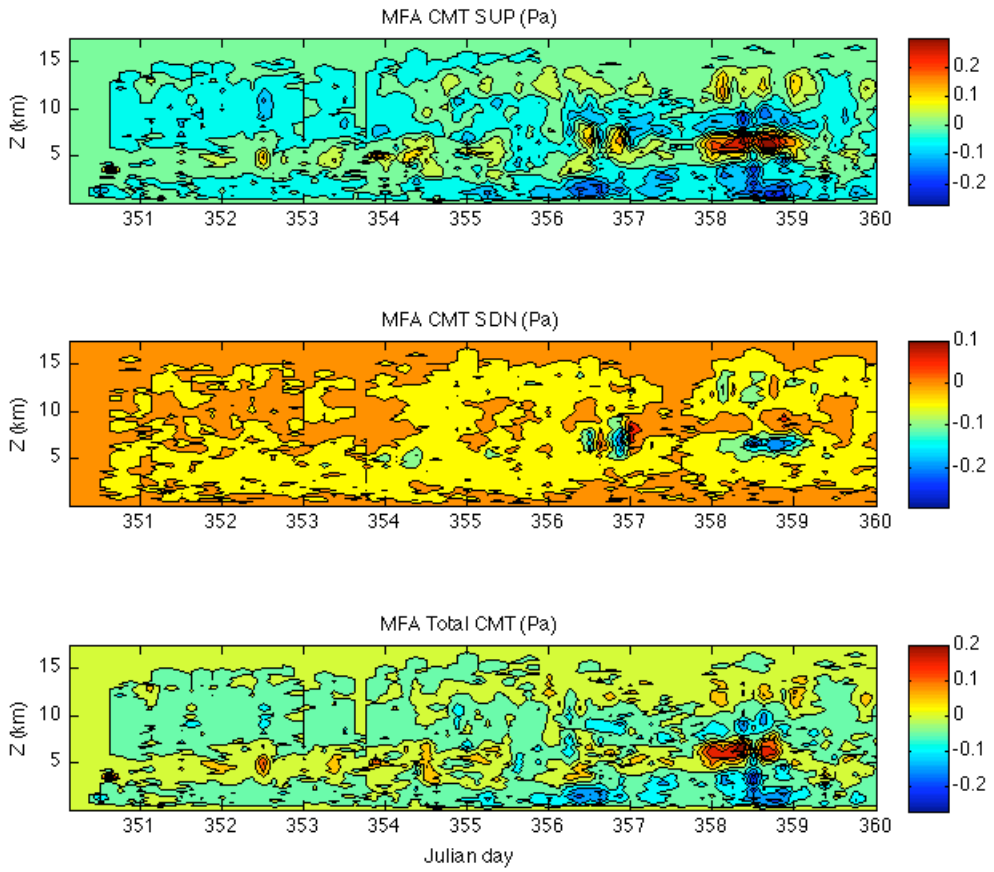

Figure 5.3.7. CMT given by the mass-flux approximation (5.3): time-height cross sections of the CMT within cumulus updrafts (*top plot*), cumulus downdrafts CMT (*middle plot*) and total CMT (*bottom plot*). Data provided by the data sets D64T120-S and 3D D64T10, for the 10-day period of simulation.

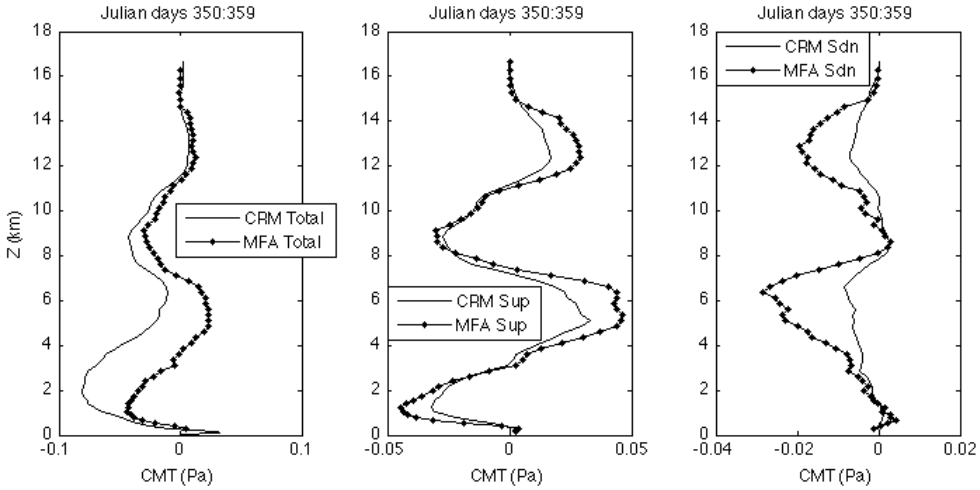

Figure 5.3.8. Vertical profiles of CRM (solid line) and parameterized (dotted lined) CMT (Pa): total (*left plot*), within cumulus updrafts (*mid-plot*) and within cumulus downdrafts (*right plot*), averaged over the 10-day window.

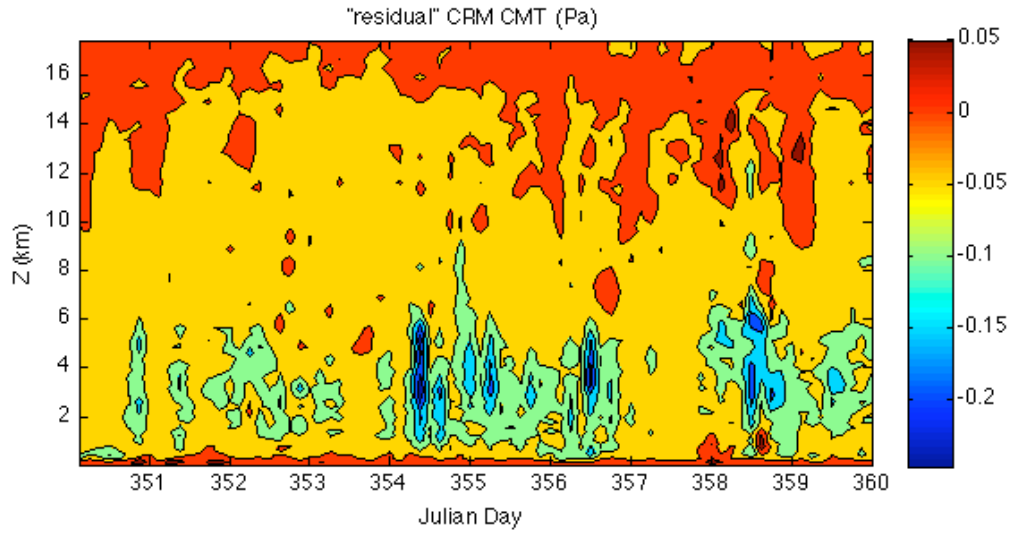

Figure 5.3.9. Time-height cross-section of the 'residual' CMT, simulated by the CRM, obtained as the difference between total CMT and CMT contributed by cumulus drafts, for the 10-day time interval.

Chapter 6

Discussion and Directions for Future Work

Cumulus convection embedded in a tropical atmosphere is a complex subject and a broad field of research, yet it is of vital importance to understand in order to build up skillful parameterizations to be used in global climate models and numerical weather prediction models, improving their simulations of the general circulation of the atmosphere. Most of this complexity originates from the intricate internal structure of cumulus clouds, composed by a number of short-lived individual rising buoyant towers which are nonhydrostatic, unsteady and highly turbulent, and internally driven by latent heating, giving them a unique character and making it difficult to completely access them through observations and model studies. Cumulus clouds are strongly affected by the thermodynamic and moisture structures of their environment, as well as the horizontal and vertical velocity fields on much larger scales.

On the other hand, to understand tropical motion systems, one must comprehend and evaluate the strong interactions among cumulus convection, mesoscale and large-scale circulations. Quantifying the effect of deep precipitating cumulus clouds on the dynamics and energetics of large-scale atmospheric systems is of primary importance, due to the great magnitudes of the energy transformations associated with the changes of water phases in deep precipitating cumulus clouds and their updrafts and downdrafts which often occupy most of the troposphere, as well as the vertical convective transports of heat, moisture and momentum.

Convective momentum transport has proved to be a difficult field of research, mostly due to the nature of its interactions with the large-scale environment: observations of the horizontal wind perturbations and cloud-mass fluxes, for instance, are very hard to

obtain, and inferring the CMT over large regions from budget studies continues to have large uncertainties. In addition, the effect of CMT on tropical circulations, while important, is much more subtle than that of latent heating in cumulus clouds. For this reason, progressing in parameterizing convective momentum transport has been slow in comparison with the convective transports of heat and moisture, which have attracted more attention by the scientific community.

One good way to seek understanding of the mechanisms underlying convective momentum transport is to use cloud-resolving models which, for the last decade, are the most advanced tool for simulating cumulus cloud systems. Cloud-resolving models are able to explicitly resolve convective motions and simulate the properties of the cloud and their environment, however they still need parameterizations microphysical processes, like cloud microphysics and precipitation loading, and unresolved subgrid turbulence.

This thesis has analyzed CMT in 3-dimensional cloud-resolving model simulations of a very important four month observational campaign over the warm pool of western Pacific – TOGA COARE, characterized by episodes of strong convection in varying horizontal wind profiles that can produce diverse patterns of CMT. The fundamental goal of this thesis was to investigate the convective momentum fluxes by tropical deep convective clouds over the ocean and compare them with assumptions used in parameterizations of CMT, aiming to contribute for improvements of future cumulus parameterizations. Our analysis was inspired by previously proposed theoretical formulations and other modeling case-studies. Our cloud resolving model simulations improve on previous modeling studies by using a combination of a larger and/or a longer period of simulation.

Some conclusions from our analysis are as follows. First, no prior study has investigated the sensitivity of CMT to the model horizontal domain size. This is a important model feature, because even if the cloud-resolving model can't resolve larger-scale motions, the increase of the spatial domain size corresponds to an expansion of the influence of the initial large-scale forcing, as well as initial and boundary conditions, and allows development of mesoscale convective organization that has been hypothesized to be important for CMT. By comparing simulations with domains 64 km and 256 km on a side, we found that convective momentum transport is not sensitive to this change of the model horizontal domain size.

A second important new conclusion was the important role of unsaturated motions in CMT in the lower troposphere. Unsaturated downdrafts around cumulus clouds are not considered in any current CMT parameterizations, but make up a substantial fraction of the overall CMT at altitudes below 5 km, according to our simulations. Except for this contribution, a mass-flux approximation in which CMT is attributed to updraft and

downdrafts contributions each given as the product of a mass flux and a horizontal velocity perturbation, works satisfactorily.

A third conclusion was that a downgradient mixing-length parameterization to CMT works well in the upper troposphere, where there are extensive regions of turbulent cumulus anvil detrained from the strongest updrafts, and that the appropriate mixing length is around 1 km. This mixing length is much smaller than what we would expect from typical entrainment rates used for thermodynamic variables in cumulus parameterizations, suggesting that those entrainment rates are far too small to describe momentum mixing. On the other hand, in the mid-troposphere, downgradient momentum mixing has little skill in predicting CMT.

Lastly, we compared our CRM results to the modern GKI97 mass-flux parameterization of CMT including entrainment and pressure-gradient effects on updrafts and downdrafts. We found that the pressure-gradient contribution to horizontally accelerating updraft air is only a third as large in the CRM than assumed in the CMT parameterization. We also found that the entrainment of momentum was too weak to keep the updraft horizontal velocity as close to the environmental zonal velocity as found in the CRM. Together, these suggest that one should use a smaller PGF_x contribution but a much larger upper-tropospheric entrainment rate in this parameterization than is currently done.

This investigation has enriched our knowledge about the vertical transport of horizontal momentum in cumulus convection through a more concrete understanding about its properties uncovered by 3-dimensional CRM simulations. It has also suggested some directions for future work. The role of unsaturated drafts upon CMT, a more reliable deep convective entrainment rate for momentum and the role of updraft pressure-gradient forces should all be studied for a wider variety of types of cumulus convection, to test the robustness of our results. It may be necessary to separately parameterize the unsaturated downdrafts around cumulus clouds. As a start, it would be good to extend our analysis to the whole four-month campaign period of TOGA COARE, which was not completely performed due to time constraints.

Bibliography

Arakawa, A., 2004: The Cumulus Parameterization Problem: Past, Present, and Future. *J. of Climate.*, **17**, 2493-2525.

Austin, P. M., and R. A. Houze, Jr., 1973: A technique for computing vertical transports by precipitating cumuli. *J. Atmos. Sci.*, **30**, 1100-1111.

Blossey, P. N., C. S. Bretherton, J. Cetrone, and M. Khairoutdinov, 2007: Cloud-resolving model simulations of KWAJEX: Model sensitivities and comparisons with satellite and radar observations. *J. Atmos. Sci.*, **64**, 1488-1508.

Bretherton, C. S. And P. K. Smolarkiewicz, 1989: Gravity waves, compensating subsidence and detrainment around cumulus clouds. *J. Atmos. Sci.*, **46**, 740-759.

Bretherton, F. P., 1969: Momentum transport by Gravity Waves. *Quart. J. Roy. Meteor. Soc.*, **95**, 213-243.

Brown, A. R., 1999: Large-eddy simulation and parameterization of the effects of shear on shallow cumulus convection. *Bound.-Layer Meteor.*, **91**, 65-80.

Carr, Matthew T., and C. S. Bretherton, 2001: Convective momentum transport over the tropical Pacific: Budget estimates. *J. Atmos. Sci.*, **58**, 1673-1693.

Charney, J. G., and A. Eliassen, 1964: On the growth of hurricane depression. *J. Atmos. Sci.*, **21**, 68-75.

Ciesielski, P. E., R. H. Johnson, P. T. Haertel and J. Wang, 2003: Corrected TOGA COARE sounding humidity data: Impact on diagnosed properties of convection and climate over the warm pool. *J. Clim.*, **16**, 2370-2384.

Cotton, William R., and R. A. Anthes, 1989: Storm and Cloud Dynamics. Academic Press,Inc, 883 pp.

Deb, S. K., H. C. Upadhyaya, J. Y. Grandpeix, and O. P. Sharma, 2006: On convective entrainment in a mass flux cumulus parameterization. *Meteorol. Atmos. Phys.*, **94**, 145-152.

Flatau, M., and D. E. Stevens, 1987: The effect of horizontal pressure gradients on the momentum transport in tropical convective lines. Part II: Lagrangian calculations. *J. Atmos. Sci.*, **44**, 2088-2096.

Gallus, W. A., Jr., and R. H. Johnson, 1992: The momentum budget of an intense midlatitude squall line. *J. Atmos. Sci.*, **49**, 422-450.

Gao, K., D.-L. Zhang, M. W. Moncrieff, and H.-R. Cho, 1990: Mesoscale momentum budget of a midlatitude squall line: A numerical case study. *Mon. Wea. Rev.*, **118**, 1011-1028.

Godfrey, J. S., R. A. Houze Jr., R. H. Johnson, R. Lukas, J.-L. Redelsperger, A. Sumi and R. Weller, 1998: Coupled Ocean-Atmosphere Response Experiment (COARE): An interim report. *J. Geophys. Res.,* **103**, 14395-14450.

Grabowsky, W., X. Wu and M. Moncrieff, 1996: Cloud Resolving Modeling of Tropical Cloud Systems during Phase III of GATE. Part I: Two Dimensional Experiment. *J. Atmos. Sci.*, **53**, 3684-3709.

Gregory , D., R. Kershaw and P. M. Inness, 1997: Parametrization of Momentum Transport by Convection. Part II: Tests in Single Column and General Circulation Models. *Quart. J. Roy. Meteor. Soc.*, **123**, 1153-1183.

Holland, J. Z., and E. M. Rasmussen, 1973: Measurements of the atmospheric mass, moisture and momentum budgets over a 500-kilometer square of tropical ocean. *Mon. Wea. Rev.*, **101**, 44-55.

Hourinochi, T., S. Pawson, K. Shibata, U. Langematz, E. Manzini, M.A. Giorgetta, F. Sassi, R.J. Wilson, K. Hamilton, J. DE Grandpre, and A. A. Scaife, 2003: Tropical Cumulus Convection and Upward-Porpagating Waves in Middle-Atmospheric GCMs. *J. Atmos. Sci.*, **60**, 2765-2782.

Houze, R. A., Jr., 1973: A climatological study of vertical transports by cumulus-scale convection. *J. Atmos. Sci.*, **30**, 1112-1123.

Houze, R. A., Jr., 1994: Cloud Dynamics. Academic Press, Inc., 573 pp.

Inness, P. M., and D. Gregory, 1997: Aspects of the intraseasonal oscillation simulated by the Hadley Centre Atmospheric Model. *Climate Dynamics*, **13**, 441-458.

Kershaw, R. and D. Gregory, 1997: Parameterization of momentum transport by convection. I: Theory and cloud modelling results. *Quart. J. Roy. Meteor. Soc.*, **123**, 1133-1151.

Kim, D., J. Kug, I. Kang, F. Jin and A. T. Wittenberg, 2008: Tropical Pacific Impacts of Convective Momentum Transport in the SNU coupled GCM. *Clim. Dyn.*, DOI 10.1007/ s00382-007-0384-4.

Kuang, Z., P. N. Blossey and C. S. Bretherton, 2005: A New Approach for 3D Cloud Resolving Simulations of Large-Scale Atmospheric Circulation. *Geo. Res. Letters*, **32**, 1-4.

Kuang, Z. and C. S. Bretherton, 2006: A Mass-Flux SchemeView of a High-Resolution Simulation of a Transition from Shallow to Deep Cumulus Convection. *J. Atmos. Sci.*, **63**, 1895-1909.

LaFore, J.-P., J.-L. Redelsperger, and G. Jaubert, 1988: Comparison between a three-dimensional simulation and Doppler radar data of a tropical squall line: Transports of mass, momentum and moisture. *J. Atmos. Sci.*, **45**, 3483-3500.

LeMone, M. A., 1983: Momentum transport by a line of cumulonimbus. *J. Atmos. Sci.*, **40**, 1815-1834.

LeMone, M. A., G. M. Barnes, and E. J. Zipser, 1984: Momentum flux by lines of cumulonimbus over the tropical oceans. *J. Atmos. Sci.*, **41**, 1914-1932.

LeMone, M. A., and D. P. Jorgenson, 1991: Precipitation and kinematic structure of an oceanic mesoscale convective system. Part II: Momentum transport and generation. *Mon. Wea. Rev.*, **119**, 2638-2653.

LeMone, M. A., and M. W. Moncrieff, 1994: Momentum transport by convective bands: Comparisons of highly idealized dynamical models to observations. *J. Atmos.Sci.*, **51**, 281-305.

Lin, J.-L., M. Zhang and B. Mapes, 2005: Zonal momentum budget of the Madden–Julian Oscillation: The source and strength of equivalent linear damping. *J. Atmos. Sci.*, **62**, 2172-2188.

Lin, J.-L., B. Mapes, and W. Han, 2008: What are the sources of mechanical damping in Matsuno-Gill type models? *J. Clim.*, **21**, 165-179 .

Mapes, B. E., and X. Wu, 2001: Convective momentum transport in long cloud-resolving model simulations. *J. Atmos. Sci.*, **58**, 517-526.

Mechem, D. B., S. S. Chen and R. A. Houze, 2006: Momentum transport processes in the stratiform regions of mesoscale convective systems over the western Pacific warm pool. *Quart. J. Roy. Meteor. Soc.*, **132**, 709-736.

Moncrieff, M. W., 1992: Organized convective systems: Archetypical dynamical models, mass and momentum flux theory, and parametrization. *Quart. J. Roy. Meteor. Soc.*, **118**, 819-850.

Moncrieff, M. W., and E. Klinker, 1997: Organized convective systems in the tropical western Pacific as a process in general circulation models: A TOGA-COARE case-study. *Quart. J. Roy. Meteor. Soc.*, **123**, 805-827.

Newton, C. W., 1950: Structure and mechanisms of the pre-frontal squall line. *J. Meteor.*, **7**, 210-222.

Ooyama, K., 1971: A theory on parametrization of cumulus convection. *J. Meteor. Soc. Japan*, **49**, 744-756.

Palmen, E., and C. W. Newton, 1969: Atmospheric Circulations Systems. *Academic*, New York, 421 pp.

Peixoto, J. P., and A. H. Oort, 1992: Physics of Climate. *American Institute of Physics*, Springer-Verlag, 520 pp.

Prabhakaran Nayar, S. R., and S. Sreeletha, 2003: Momentum flux associated with gravity waves in the low-latitude troposheres. *Annales Geophysicae*, **21**, 1183-1195.

Richter, J. H., and P. J. Rasch, 2008: Effects of convective momentum transport on the atmospheric circulation in the Community Atmosphere Model, version 3 (CAM3). *J. Clim.*, **21**, 1487-1499.

Schneider, E. K., and R. S. Lindzen, 1976: A discussion of the parameterization of momentum exchange by cumulus convection. *J. Geophys. Res.*, **81**, 3158-3180.

Shapiro, L. J. And D. E. Stevens, 1980: Parameterization of Convective effects on the momentum and vorticity budgets of synoptic-scale Atlantic Tropical waves. *Mon. Wea. Rev.*, **108**, 1816-1826.

Smith, Roger K., 1997: The physics and parametrization of moist atmospheric convection. Kluwer Academic Publishers, 498 pp.

Stevens, D., 1979: Vorticity, momentum, and divergence budgets of synoptic-scale wave disturbances in the tropical eastern Atlantic. *Mon. Wea. Rev.*, **107**, 535-550.

Soong, S.-T., and W.-K. Tao, 1984: A numerical study of the vertical transport of momentum in a tropical rainband. *J. Atmos. Sci.*, **41**, 1049-1061.

Sui, C.-H., and M. Yanai, 1985: Cumulus ensemble effects on the large-scale vorticity and momentum fields of GATE. Part I: Observational evidence. *J. Atmos. Sci.*, **43**, 1618-1642.

The Second GEWEX Cloud System Study Science and Implementation Plan, 2000: *IGPO Publication Series*, Nº **34**, 45 pages.

Tiedtke, M., 1989: A Comprehensive Mass Flux Scheme for Cumulus Parametrization in Large-Scales Models. *Mon. Wea. Rev.*, **117**, 1779-1800.

Trier, S. B., M. A. LeMone, and W. C. Scamarock, 1998: Effect of three-dimensional structure on the stormwide horizontal accelerations and momentum budget of a simulated squall line. *Mon. Wea. Rev.*, **126**, 2580-2598.

Tung, W. and M. Yanai, 2002: Convective Momentum Transport Observed during the TOGA COARE IOP. Part I: General Features. *J. Atmos. Sci.*, **59**, 1857- 1871.

Tung, W. and M. Yanai, 2002: Convective Momentum Transport Observed during the TOGA COARE IOP. Part II: Case Studies. *J. Atmos. Sci.*, **59**, 2535- 2549.

Warner, J., 1970: The Microstructure of Cumulus Cloud: The nature of the updraft. *J. Atmos. Sci.*, **27**, 682 - 688.

Webster, P. J. and R. Lukas, 1992: TOGA COARE: The Coupled Ocean-Atmosphere Response Experiment. *Bul. American Meteor.Soc,* **73**, 1377-1416.

Wu, X., and M. Yanai, 1994: Effects of vertical shear on the cumulus transport of momentum: Observations and parameterization. *J. Atmos. Sci.*, **51**, 1640-1660.

Zhang, G. J., and H.-R. Cho, 1991: Parameterization of the vertical transport of momentum by cumulus clouds. Part I: Theory. *J. Atmos. Sci.*, **48**, 1483-1492.

Zhang, G. J., and H.-R. Cho, 1991: Parameterization of the vertical transport of momentum by cumulus clouds. Part II: Application. *J. Atmos. Sci.*, **48**, 2448-2457.

Zhang, G. J., and N. A. McFarlane, 1995: Role of convective-scale momentum transport in climate simulation. *J. Geophys. Res.*, **100**, 1417-1426.

Zhang, G. J. and X. Wu, 2003: Convective Momentum Transport and Perturbation Field from a Cloud-Resolving Simulation. *J. Atmos. Sci.*, **60**, 1120-1139.